

**Fate and Transport of Nanoparticles in Porous Media:
A Numerical Study**

A dissertation submitted by

Amir Taghavy

In partial fulfillment of the requirements for the degree of

Doctor of Philosophy

in

Civil and Environmental Engineering

Tufts University

May 2013

Adviser: Prof. Linda M. Abriola

ABSTRACT

Understanding the transport characteristics of NPs in natural soil systems is essential to revealing their potential impact on the food chain and groundwater. In addition, many nanotechnology-based remedial measures require effective transport of NPs through soil, which necessitates accurate understanding of their transport and retention behavior. Based upon the conceptual knowledge of environmental behavior of NPs, mathematical models can be developed to represent the coupling of processes that govern the fate of NPs in subsurface, serving as effective tools for risk assessment and/or design of remedial strategies.

This work presents an innovative hybrid Eulerian-Lagrangian modeling technique for simulating the simultaneous reactive transport of nanoparticles (NPs) and dissolved constituents in porous media. Governing mechanisms considered in the conceptual model include particle-soil grain, particle-particle, particle-dissolved constituents, and particle- oil/water interface interactions. The main advantage of this technique, compared to conventional Eulerian models, lies in its ability to address non-uniformity in physicochemical particle characteristics. The developed numerical simulator was applied to investigate the fate and transport of NPs in a number of practical problems relevant to the subsurface environment. These problems included: (1) reductive dechlorination of chlorinated solvents by zero-valent iron nanoparticles (nZVI) in dense non-aqueous phase liquid (DNAPL) source zones; (2) reactive transport of dissolving silver nanoparticles (nAg) and the dissolved silver ions; (3) particle-particle interactions and their effects on the particle-soil grain interactions; and (4) influence of particle-oil/water interface interactions on NP transport in porous media.

ACKNOWLEDGMENTS

Research contained herein was funded in part by Strategic Environmental Research and Development Program (SERDP), National Science Foundation (NSF), and Advanced Energy Consortium (AEC). This work has not been subject to review by the sponsoring agencies, and therefore, any opinions, findings, conclusions, and recommendations expressed herein are those of the author, do not necessarily reflect the views of SERDP, NSF and/or AEC, and no official endorsement should be inferred. Portions of this dissertation were adapted from the following manuscripts:

- Taghavy, A.; Costanza, J.; Pennell, K.D.; Abriola, L.M., 2010. Effectiveness of nanoscale zero-valent iron for treatment of a PCE–DNAPL source zone, *Journal of Contaminant Hydrology* 118(3–4) 128-142. (Chapter 2)
- Taghavy, A.; Mittelman, A.; Wang, Y.; Pennell, K.D.; Abriola, L.M. Mathematical modeling of the transport and dissolution of silver nanoparticles in porous media, submitted to *Environmental Science & Technology*, Feb. 2013. (Chapter 3)
- Mittelman, A.; Taghavy, A.; Wang, Y.; Abriola, L.M.; Pennell, K.D. Influence of Dissolved Oxygen on Silver Nanoparticle Mobility and Dissolution in Water-Saturated Quartz Sand, submitted to *Journal of Nanoparticle Research*, Feb. 2013. (Chapter 3)
- Taghavy, A.; Pennell, K.D.; Abriola, L.M., 2013. A Lagrangian approach for modeling the influence of Aggregation on the transport and retention of nanoparticles in porous media, in preparation. (Chapter 4)

The co-authors of these manuscripts are gratefully acknowledged.

Through my adventure in the “new world” which started along with my PhD at Tufts University, I have met many individuals in academic and non-academic capacities who in direct or indirect ways have added to my life and helped me improve as a scholar and as a person. I would like to thank Tufts community for providing me with this opportunity.

I would like to express my gratitude to my adviser, Prof. Linda Abriola, a distinct outlier on the distribution curve of human intelligence, for her passion and enthusiasm that have constantly motivated and inspired me. A great product requires great leadership and effective execution of great ideas. As the major product of a great proportion of my life in academia, my PhD work, in great part, owes to you the leadership and great fundamental ideas. I would also like to thank you for granting me a chance when I desperately needed one, and I am very proud for having earned your trust.

I would also like to recognize the significant contribution of my co-adviser, Prof. Kurt Pennell, for his countless number of constructive ideas, comments, and recommendations throughout my PhD. In addition, this work, in its present form, would not have been possible without the experimental data provided by his research group. My many thanks go to the members of Prof. Pennell’s Laboratory, Dr. Yonggang Wang, Ms. Anjuliee Mittelman, and Dr. Jed Costanza, the team of experimentalists behind this work. I must recognize the so many hours of thoughtful and hard work put by these colleagues of mine for attaining each experimental dataset and, in some occasions, even each data point! I would also like to dearly thank my friend and peer, Matthew Becker, for his direct contribution and aid with the inverse problems and beyond that for non-stop exchange and sharing of thoughts and ideas on a daily basis in the past three years.

My warm thanks go to my friends and comrades, Ali Boroumand and Sandeep Sathyamoorthy, who have made my learning experience at Tufts a truly enjoyable one. I would also like to thank the members of the Integrated Multi-Phase Environmental Systems (IMPES) Laboratory. My thank you goes to my friends from Amirkabir University of Technology and Sharif University of Technology, and in particular, Ali Fotowat, Rahman Edalat-manesh, Farrokh Fazileh, and Mohammadali Sharbatmaleki.

I would like to acknowledge Prof. Steven Chapra (a.k.a. Dr. C), Prof. Grant Garven, and Prof. Richard Vogel, three of my greatest teachers, who have been a great source of support and inspiration to me during my years at Tufts. In addition, I must recognize a great mentor, teacher, and a true friend of mine, Prof. Lee Minardi, who has added significantly to my professional skills and personal life. I would like to thank Prof. C. Andrew Ramsburg under whose supervision and support I gained valuable insight into the experimental aspect of the very problems which I, as a happy modeler, have been simulating. I would like to thank Prof. Nicole Berge (University of South Carolina) for tremendous amount of time and energy she spent on training me, and teaching me how to conduct batch and column experiments and operate analytical instruments.

There have been many other influential individuals who have taught me great lessons in life and supported me in the pursuit and achievement of my goals and dreams; my special thanks go to my Master's adviser Prof. Behzad Ataie-Ashtiani (Sharif University of Tech.) and my first and true mentor Prof. Mansour Peydayesh (Amirkabir University of Tech.). I would also like to express my deep gratitude to Prof. Menachem Elimelech (Yale University) for his accepting to serve on my PhD committee and his helpful comments and remarks.

Last but not the least, I would like to express my gratitude and love to my family: My wife, Fateme, without whose support, emotional and logistical, and sometimes direct scientific and communicational advice this work would not have been possible. I feel so lucky for having met you six years ago and so blessed for having had you in my life since then. My one and only brother, Ali, who is a part of my identity and a warmth in my heart, I do not find the right words to describe the irreplaceable bond between us. My parents who went through a lot of hardships to give us chances in life that they had not been given. Thank you, mom, for all the love and affection you gave me, and beyond that for the sincere respect I have received from you for so long as I remember, as a grown-up man, an arrogant juvenile, and a demanding little child! Thank you, dad, for having always had believed in me and for your relentless support throughout my life. If I ever become a father, being the father that you have been to me to your grandchildren would be a hard challenge and yet my ultimate goal!

TABLE OF CONTENTS

Abstract.....	ii
Acknowledgments.....	iii
Table of Contents.....	vii
List of Tables	x
List of Figures	x
Chapter 1 Background	1
1.1. Nanoparticles in the Subsurface Environment	1
1.2. Modeling the transport of NPs in Porous Media	3
1.2.1. Modeling the Particle-Soil Grain Collector Interactions (i.e. Deposition and Detachment)	4
1.2.2. Modeling Particle-Particle Interactions (i.e. Aggregation)	9
1.2.3. Modeling Particle-Dissolved Phase Interactions (i.e. Chemical Reactions)	13
1.2.4. Modeling Particle-Water/NAPL Interface Interactions.....	15
1.2.5. Modeling Particle Non-Uniformity.....	18
1.3. Eulerian Method vs. Lagrangian Method for Solving the Transport Equation	19
1.3.1. Deterministic Eulerian transport (e.g., Method of Finite Differences).....	20
1.3.2. Stochastic Lagrangian transport (e.g., Random-Walks Particle-Tracking Method)	21
1.4. Summary and Significance	24
1.5. Research Objectives.....	25
Chapter 2 Effectiveness of Nano-scale Zero-valent Iron for Treatment of PCE-DNAPL Source-Zones	27
2.1. Introduction	27
2.2. Materials and Methods.....	30
2.2.2. Analytical Methods	31
2.3. Mathematical Model	32
2.4. Results and Discussion	37

2.4.1. Experimental Results	37
2.4.2 Mathematical Modeling Results	39
2.4.3. Sensitivity Analysis	44
2.4.4. <i>Damköhler</i> Number Analysis.....	56
2.5. Summary and Conclusions	59
Chapter 3 Modeling of the Transport and Dissolution of Silver Nanoparticles in Porous Media	61
3.1. Introduction	61
3.2. Materials and Methods.....	63
3.2.1. Batch Dissolution Experiments	64
3.2.2. Column Experiments.....	65
3.3. Mathematical Model	66
3.3.1. The Transport of nAg and Dissolved Constituents.....	66
3.3.2. nAg Dissolution	68
3.3.3. Numerical Implementation.....	70
3.4. Results and Discussion.....	74
3.4.1. nAg Dissolution Kinetics.....	74
3.4.2. Simulation of Coupled nAg Transport and Dissolution.....	77
3.4.3. Model Sensitivity Analysis.....	84
3.5. Conclusions	87
Chapter 4 Modeling Particle-Particle Interactions and their Influence on the Transport and retention of NPs in Porous Media.....	89
4.1. Introduction	89
4.2. Mathematical model.....	92
4.3. Numerical Implementation.....	95
4.3.1. Numerical Implementation of Particle-Collector Interactions	95
4.3.2. Numerical Implementation of Particle-Particle Interactions.....	95
4.4. Results and Discussion.....	97
4.4.1. Verification of the Coupled Aggregation-Transport Model.....	97
4.4.2. Sensitivity Analysis	106
4.5. Conclusions	115
Chapter 5 Modeling NP-Oil/Water Interface Interactions.....	118

5.1. Introduction	118
5.2. Mathematical Model	121
5.2.1. Phase Mass Balance Equations	122
5.2.2. Component Mass Balance Equations.....	123
5.3. Numerical Implementation.....	127
5.3.1. Model Verification	128
5.4. Results and Discussion	129
5.4.1. The Hypothetical Scenario	129
5.4.2. Sensitivity Analysis	141
5.5. Conclusions	146
Chapter 6 Conclusions and Recommendations	148
6.1. Conclusions	148
6.2. Recommendations and Future Directions	153
Appendices.....	155
Appendix I	156
I.1. Some Notes on the Solution Algorithm of HELP-1D Simulator.....	156
Appendix II	158
II.1.Verification of Transport Modules of HELP-1D.....	158
Appendix III	162
III.1. Sensitivity of Modeling Results to Numerical Parameters.....	162
Appendix IV	166
IV.1. Nomenclature	166
Bibliography	169

LIST OF TABLES

Table 2-1. Summary of experimental properties and model input parameters [91].	40
Table 3-1. Summary of experimental properties and model input parameters [114].	77
Table 4-1. Summary of experimental properties and model input parameters reported by Raychoudhury et al. [123].	98
Table 4-2. Summary of scenarios considered in the sensitivity study.	107
Table 5-1. List of model input parameters used in the simulation of the generic case scenario.	130
Table 5-2. Interpretation of the physical meaning of the sigmoidal model parameters.	131

LIST OF FIGURES

Figure 1-1. Conceptual model of nZVI transport showing filtration, straining, and DNAPL targeting [13].	15
Figure 2-1. Placement of the RNIP particles in the PCE-DNAPL containing sand column [91].	39
Figure 2-2. Experimental and model breakthrough curves of dissolved-phase PCE and ethane [91].	41
Figure 2-3. Spatial distribution profiles of (a) DNAPL saturation, (b) Fe ⁰ content of soil, and (c) dissolved PCE and ethene concentrations at different simulation times [91].	43
Figure 2-4. Influence of initial emplaced nZVI concentration on (a) DNAPL mass remaining in the source zone and PCE transformation efficiency, and effluent concentrations of (b) PCE, and (c) ethane [91].	46
Figure 2-5. Influence of flow rate on (a) DNAPL mass remaining in the source zone and PCE transformation efficiency index, and effluent concentrations of (b) PCE, and (c) ethene. Here lower Fe content=28.3 g/kg [91].	49
Figure 2-6. Influence of DNAPL source zone size on (a) DNAPL mass remaining in the source zone and PCE transformation efficiency index, and effluent concentrations of (b) PCE, and (c) ethene. Here lower Fe content=28.3 g/kg [91].	52
Figure 2-7. Influence of downstream nZVI zone on (a) DNAPL mass remaining in the source zone and PCE transformation efficiency index, and effluent concentrations of (b) PCE, and (c) ethene. Here lower Fe content=28.3 g/kg [91].	55
Figure 2-8. Logarithmic diagrams of (a) Da ₁ -PCE TEI, (b) modified Da ₁ -PCE TEI relations, and (c) range of linearity of Log modified Da ₁ -PCE TEI relationship [91].	58
Figure 3-1. Dissolved silver ion concentrations measured in batch reactors as a function of pH and mixing time. First-order model (Eq. 3.6) fit obtained for pH 4 data set based on a LSSR procedure [114].	75
Figure 3-2. Time release of Ag ⁺ from nAg solutions over 48 hours at (a) pH 7 and (b) pH 4 for DO concentrations of 9 mg/L (◆), 2 mg/L (▲) and < 0.2 mg/L (●). Early time data	

(time 0 to 2.33 hours) for pH 7 and 4 are shown in detail in plots (c) and (d), respectively. Solid lines show modified first order model predictions for all data except early time pH 7 [115]...... 76

Figure 3-3. Measured and simulated effluent concentrations of nAg particles and Ag⁺ ions at pH 7 performed in water-saturated columns packed with 40-50 mesh Ottawa sand [114]...... 80

Figure 3-4. Measured and simulated effluent concentrations of (a) nAg particles and (b) Ag⁺ ions in water-saturated column experiments (1, 2, 3) conducted at pH 4 [114]. 80

Figure 3-5. HELP-1D fits to nAg and Ag⁺ effluent concentrations, and Liu and Hurt (2010) correlation based prediction of nAg dissolution. 82

Figure 3-6. (a) Effect of dissolved oxygen concentration in pH 4 column experiments on (a) Nanoparticle breakthrough and (b) Ag⁺ breakthrough. HELP-ID fits (DO=9 mg/L) and predictions (DO=2 and <.2 mg/L) for nAg and Ag⁺ breakthrough data are shown. Inset shows nAg breakthrough during first 6 pore volumes in greater detail [115]. 84

Figure 3-7. Influence of (a) applied flow rate (0.1 to 1.0 mL/min) and (b) nanoparticle diameter (12 to 120 nm) on (1) total Ag recovery and on effluent concentrations of (2) nAg and (3) Ag⁺ in water-saturated 40-50 mesh Ottawa sand at pH 4 [114]. 86

Figure 4-1. (a) Experimental (▲) and modeled (HELP-1D – solid and R-model – dashed lines) effluent CMC-nZVI concentrations, (b) influent (dashed lines) and effluent (solid lines) cumulative volumetric PSD curves predicted by HELP-1D, and (c) changes in collision efficiency with particle diameter (50-400 nm) at flow velocity of 6.4 m/day. 100

Figure 4-2. Comparison of simulated CMC-nZVI BTCs based on binary (shown in black) and polyadic (shown in red) (a) with aggregation at the inlet boundary and inside the column, and (b) with aggregation only inside the column for $C_{0,NP} = 725$ mg/L, and (c) the predicted cumulative volumetric particle size distribution for each simulation after 80 PV. 104

Figure 4-3. Effect of changes in the influx of model particles on (a) predicted effluent NP concentrations and (b) computational time. 106

Figure 4-4. Influence of pore water velocity on (a) effluent NP concentration for aggregating (in red and blue) and non-aggregating (in black) particles, (b) predicted cumulative volumetric PSD curves for effluent NPs, and (c) collision efficiency – particle diameter relationship. 108

Figure 4-5. Influence of pore water velocity on (a) effluent NP concentration for aggregating (in red and blue) and non-aggregating (in black) particles, (b) predicted cumulative volumetric PSD curves for effluent NPs. Here, aggregation occurs only inside the column (i.e. $\alpha_{PP} = 0$ at the column inlet boundary and $\alpha_{PP} = 3.08 \times 10^{-4}$ inside the column). 110

Figure 4-6. Influence of (a) influent NP concentration and (b) aggregation efficiency on predicted (1) effluent NP concentrations, (2) spatial distribution of retained NPs, and (3) cumulative volumetric PSD curves of effluent NPs. 113

Figure 4-7. Influence of primary particle size on (a) effluent NP concentration for aggregating (in red) and non-aggregating (in black) particles, (b) predicted cumulative

volumetric PSD curves for effluent NPs, and (c) collision efficiency – particle diameter relationship.....	115
Figure 5-1. Three types of variation of γ with c for aqueous solutions: (1) simple organic solutions, (2) simple electrolytes, and (3) amphipathic solutes (Fig. 7-14) [131].	121
Figure 5-2. A schematic of the NP and surfactant transport and interactions with the solid phase and o/w IF and interphase mass transfer (i.e. solubilization of the organic liquid phase in the aqueous phase).	122
Figure 5-3. Comparative NP and surfactant (a) BTCs and (b) solid phase retention profiles simulated by HELP-1D and MCB models [126] for simultaneous injection of a 3 pore volume pulse of 10 mg/L of quantum-dot particles and 3 mg/L of PAA.	129
Figure 5-4. Experimental $\gamma - \ln c$ data measured at Isopar oil/water interface for (a) Calfax 16L-32 surfactant (with a sigmoidal fit) and (b) magnetite NPs (with a 2 nd -order polynomial fit).	131
Figure 5-5. Surface excess – bulk phase concentration ($\Gamma - c$) curves in (a) logarithmic and (b) linear concentration scales derived from IFT data measured at Isopar oil/water interface for Calfax 16L-35 surfactant and nMag.	132
Figure 5-6. Interfacial tension measured over a 600 s time interval at Isopar/water interface for Calfax 16L-35 surfactant at variable bulk aqueous concentrations of (a) 10, (b) 30, (c) 100, and (d) 200 mg/L.	133
Figure 5-7. (a) Simulated effluent concentrations of nMag particles, and (b) effluent concentrations of nMag magnified for better visual illustration of the difference between NP breakthrough predicted for C_0 of 1 and 10 mg/L. Here, nMag interactions with solid phase are neglected.	134
Figure 5-8. Simulated retention profiles of nMag particles captured by o/w IF at different simulation times corresponding to 0.5, 1.0 and 5.0 aqueous PVs for C_0 values of (a) 1 mg/L and (b) 10 mg/L. Here, nMag interactions with solid phase are neglected.	135
Figure 5-9. Simulated effluent concentrations of (a) Calfax 16L-35 and (b) dissolved Isopar. Here, surfactant and dissolved oil adsorption to the solid phase is neglected. ..	136
Figure 5-10. Simulated retention profiles of Calfax 16L-35 adsorbed to the o/w IF at different simulation times corresponding to 0.5, 1.0 and 5.0 aqueous PVs for C_0 values (a) 10 mg/L and (b) 100 mg/L. Here, surfactant adsorption to the solid phase is neglected.	136
Figure 5-11. Simulated (1) effluent concentrations and (2) retention profiles of nMag ($C_0 = 1$ mg/L) and Calfax 16L-35 ($C_0 = 10$ mg/L), based on (a) competitive one-site and (b) non-competitive site-blocking models.	137
Figure 5-12. Simulated (a) effluent concentrations and (b) retention profiles of nMag inside the column (in the absence of surfactant) using the experimental Gibbs surface excess (Γ_{exp}) and a hypothetical surface excess curve one order-of-magnitude greater than Γ_{exp} . Here, nMag interactions with solid phase are disregarded.	139
Figure 5-13. Simulated nMag and Calfax 16L-35 surfactant (a) effluent and (b) retained concentrations, and (c) aqueous phase concentration profiles of Calfax 16L-35 surfactant and dissolved oil. Here, the interactions of nMag and Calfax 16L-35 with the solid phase are disregarded.	140

Figure 5-14. Influence of (a) the nMag surface excess, (b) the rate coefficient of surfactant adsorption to the o/w IF ($1 \times 10^{-4} - 0.01$ 1/s), (c) the attachment efficiency of nMag to the o/w IF (0.013-1.0), and (d) influent Calfax 16L-35 concentration on the simultaneous transport of Calfax 16L-35 and nMag particles in a sand column containing 20% saturation of oil at constant pore velocity of ca. 7.6 m/day.	144
Figure 0-1 Solution algorithm flowchart of the hybrid simulator.....	157
Figure 0-2. A 2PV pulse of non-attaching particles (1), and a 3PV continuous injection of attaching CFT particles (2).	159
Figure 0-3. Breakthrough (1) and retained (at 6 PV) (2) concentrations of irreversibly attaching particles according to MFT.	159
Figure 0-4. Breakthrough (1) and retained (at 20 PV) (2) concentrations of reversibly attaching particles according to MFT.	160
Figure 0-5. Breakthrough concentrations of a 2PV pulse of a tracer solute (1) and of reacting dissolved TCE (2).	161
Figure 0-6. Influence of changes in (a) time-step size, Δt , and (b) grid-block spacing, Δx , on simulated NP and surfactant retention profiles after (1) 0.4, (2) 0.8 and (3) 4.0 pore volumes for $\alpha_{if} = 0.013$	163
Figure 0-7. Influence of changes in (a) time-step size, Δt , and (b) grid-block spacing, Δx , on simulated NP and surfactant retention profiles after (1) 0.4, (2) 0.8 and (3) 4.0 pore volumes for $\alpha_{if} = 0.13$	164
Figure 0-8. Influence of changes in (a) time-step size, Δt , and (b) grid-block spacing, Δx , on simulated NP and surfactant retention profiles after (1) 0.4, (2) 0.8 and (3) 4.0 pore volumes for $\alpha_{if} = 1.0$	165

Chapter 1 BACKGROUND

1.1. Nanoparticles in the Subsurface Environment

In this chapter, the main processes governing the fate and transport of nanoparticle (NPs) in the subsurface are outlined, and the existing body of literature with a primary focus on the previous attempts for mathematical representation of these processes is reviewed.

As the basic building block of nanotechnology, engineered nanoparticles (NPs) are finding their use in electronic, biomedical, personal care, and automotive products [1]. The potential market value for nanotechnology-related materials is estimated to approach nearly US\$1 trillion per annum [2]. Due to high-volume production and widespread use, anthropogenic NPs will inevitably intrude into the natural environment, and in particular, terrestrial ecosystems, during manufacture, transportation, use, and/or disposal [1]. The risk posed by such materials to human health and the environment is currently unclear, but preliminary evidence suggests certain NPs such as nanosilver (nAg) may harm people, organisms, or the environment [3, 4].

NPs are defined as substances that are less than 100 nm in more than one dimension [5]. Transport and deposition of NPs, similar to micron-sized colloidal particles, is controlled by their physiochemical properties as well as environmental

conditions such as flow velocity, soil grain size, and solution chemistry [6]. Their tiny dimension, however, allows NPs to fit into the smallest pore spaces within soil particles, creating the potential for migrating longer distances in terrestrial systems than larger particles before becoming trapped in the soil matrix [7]. Along with their small sizes, the prevalence of negatively charged substrates in aquatic environments [8] is expected to inhibit the deposition of negatively charged NPs by electrostatic repulsion [6]. Stability of NPs in aqueous environments is another key factor controlling their transport and ultimate fate in aqueous environments [1]. Changes in particle shape and size resulting from aggregation may significantly alter transport potential as well as the reactivity and toxicity of NPs [9]. In addition, NPs may experience chemical transformation in natural aquatic systems, including oxidation/reduction (e.g., oxidation of zero-valent-iron nanoparticles (nZVI) via reductive dehalogenation reaction with chloroethenes), dissolution (e.g., dissolution of nAg or ZnO nanoparticles), hydrolysis, and biological degradation.

A comprehensive understanding of fate and transport of NPs in the subsurface is required to assess their potential negative impact on the environment[10]. In addition, many nanotechnology-based remedial measures require effective transport of NPs (e.g. nZVI) through soil [11], which necessitates accurate understanding of their transport behavior [1]. Mathematical models based upon the conceptual knowledge of environmental behavior of NPs can be developed to represent the coupling of processes that govern the fate of NPs in subsurface, serving as effective tools for risk assessment and/or design of remedial strategies. A main objective of this research was to develop a numerical simulator that is capable of simulating the simultaneous reactive transport of NPs and solute constituents in the subsurface, taking into account mechanisms that govern the fate and transport of NPs. Such mechanisms include particle-soil grain,

particle-particle, particle-dissolved phase constituents, and particle-oil/water interface (o/w IF) interactions.

1.2. Modeling the transport of NPs in Porous Media

According to a 2011 review article on the environmental fate of nanomaterials (NMs) [12] most of the studies on fate and transport of NPs in terrestrial porous media have led to the conclusion that increased entry into the soil of engineered and anthropogenic NPs raises concern about their fate, transport, and potential adverse effects on animal and human health. Until recently, however, no direct or relevant data pertaining to the fate and transport of NMs in “terrestrial systems” existed. To date, there are only a few published reports addressing the behavior of NPs in real soil systems (e.g., [13-17]). Even fewer studies have involved simulation of the fate and transport of NPs in the subsurface. To the best of the author’s knowledge, those few that attempted to simulate the fate and transport of NPs had based their study on the assumption of **identical** particles and failed to address the evolution of physiochemical characteristics of NPs in the subsurface as they interact with each other and with other coexisting reactive compounds.

When released into aquatic environments, NP behavior depends on particle-specific properties (e.g., size, shape, chemical composition, surface charge, and coating), particle state (free or matrix incorporated), the surrounding solution chemistry (e.g., pH, ionic strength, ionic composition, natural organic matter content), and hydrodynamic conditions [18]. An integrated assessment of NP behavior in porous media requires taking into account how NPs interact with (1) the soil matrix, (2) co-existing dissolved components, and (3) other NPs. In addition, should a secondary fluid phase exist in the porous medium (e.g., DNAPL or oil residuals), the fate of NPs could be affected by its

presence. In the following Subsections (1.2.1 – 1.2.5) a summary of related modeling work in the literature is presented.

1.2.1. Modeling the Particle-Soil Grain Collector Interactions (i.e. Deposition and Detachment)

Particle attachment, the removal of particle mass from solution via collision with and fixation to the porous media, is typically assumed to be a primary process controlling the transport of colloids - particles with effective diameters less than $10\mu\text{m}$ [19]. The movement of colloids – and therefore also of NPs – in porous media may be impeded by two processes: (1) straining or physical filtration where the particle is larger than the pore throat and is trapped and (2) true filtration where a particle is removed from suspension by interception, diffusion, and sedimentation [20]. A brief overview of previous work on modeling these two processes of particle capture in porous media is provided in Subsections 1.2.1.1 and 1.2.1.2.

1.2.1.1. Particle Filtration

The filtration of particles by the collector surfaces is determined largely by the collisions between particles and soil grain surfaces, which, in turn, is regulated by solution chemistry and chemical characteristics of particles and surfaces. Physical parameters, such as particle size, fluid velocity, grain size, and water temperature can also play roles in filtration of nanoparticles [1]. These interactions have traditionally been described by the *Derjaguin-Landau-Verwey-Overbeek* (a.k.a. DLVO) Theory of colloidal stability. According to the DLVO theory, the stability of NPs suspended in an aqueous environment can be evaluated as the sum of *van der Waals* and electrostatic double-layer interactions. The resultant interaction energy will determine the particle stability as two surfaces approach one another. However non-DLVO forces such as steric,

magnetic, and hydration forces can also play an important role in particle-soil grain and particle-particle interactions [18].

Most of the few published modeling studies that describe the transport and deposition of NPs in saturated porous media have implemented a form of the Advection-Dispersion-Reaction (ADR) equation with a first-order filtration term based on either (1) the Classical Filtration Theory (CFT) [21, 22] or (2) a Modified version of the Filtration Theory (MFT) [10, 15, 17, 23]. General forms of transport mass balance equations for (1) NPs suspended in the aqueous phase and (2) those associated with the solid phase are expressed as:

$$\left(\frac{\partial C}{\partial t} + \frac{\rho_b}{\phi S_w} \frac{\partial \omega}{\partial t}\right) - \nabla \cdot (\overline{D}_h \cdot \nabla C) + \overline{v}_w \cdot \nabla C = 0 \quad (1.1)$$

$$\frac{\rho_b}{\phi} \frac{\partial \omega}{\partial t} = k_{dep} \psi_{dep} C - \rho_b k_{det} \omega \quad (1.2)$$

where C [mM] is the molar concentration of NPs in the aqueous phase, ω [mol/kg soil] is the concentration of NPs attached to the solid phase, t [s] is time, ρ_b [kg/m³] is the bulk density of soil, ϕ [-] is the soil porosity, and S_w [-] is the aqueous phase saturation. \overline{D}_h [m²/s] is the hydrodynamic dispersion tensor, and \overline{v}_w [m/s] is the pore water velocity vector. ψ_{dep} [-] is a site blocking function, and k_{dep} [s⁻¹] and k_{det} [s⁻¹] are the NP deposition and detachment rate coefficients, respectively.

Three basic mechanisms for particle capture by solid soil collectors are considered in the Classical Filtration Theory (CFT): Brownian diffusion, interception, and gravitational sedimentation. Transport of the larger particles is regulated by interception and sedimentation mechanisms, whereas Brownian diffusion is the dominant factor controlling the transport of nano-scale particles to the collector surfaces [24]. The deposition rate coefficient can be expressed as [25]:

$$k_{dep} = \frac{3(1-\phi S_w)v_w}{2d_c} \alpha \eta_0 \quad (1.3)$$

where d_c [m] is a representative collector diameter, the collision efficiency factor, α [-], represents the fraction of collisions that result in attachment of particles to the collector sand grains, and the single collector efficiency, η_0 [-], represents the frequency of particle collisions with the porous medium collector surfaces. η_0 can be calculated from an empirical correlation proposed by *Tufenkji and Elimelech* [24] where the overall single collector contact efficiency is written as the sum of contributions for each transport mechanism (i.e. *Brownian* diffusion, η_D , interception, η_I , and gravitational sedimentation, η_G).

$$\eta_0 = \eta_D + \eta_I + \eta_G \quad (1.4)$$

The value of ψ_{dep} in Equation 2.2 equals 1 for clean-bed CFT-based conditions. CFT assumes an infinite capture capacity for collector surfaces. Experimental observations of colloidal transport are not always in agreement with the CFT [19]. Some of these discrepancies have been attributed to soil surface roughness [26], charge heterogeneity [27], variability of colloid characteristics [28], and/or existence of repulsive forces between the particles and the soil grains [8].

Other functional forms for ψ_{dep} have been proposed in the literature to account for particle blocking, ripening, and non-exponential spatial distribution. For example *Johnson and Elimelech* [27] proposed the following site-blocking function for time-dependent deposition behavior in a manner similar to *Langmuirian* blocking:

$$\psi_{dep} = \left(1 - \frac{\omega}{\omega_{max}}\right) \quad (1.5)$$

where ω_{max} [mol/kg soil] is the particle retention capacity of the soil. Site blocking has been cited as an important mechanism in the transport of certain types of NPs (e.g., C₆₀ nanoparticles [15], and multi-walled carbon nanotubes [23]). In these studies, it was observed that NP transport could not be predicted using the traditional CFT approach due to delayed NP breakthrough in column experiments. Experimental observations from these studies suggested that the sand collector surface had a finite retention capacity. Initially, the retention rate of NPs was large, but with time the retention capacity of the collector surfaces was achieved and NPs were no longer removed from the suspended-phase. This demonstrates the fundamental idea behind the MFT approach.

There are other types of NPs, however, whose retention in porous media has been adequately described by CFT. For example, *Fang et al.* [22] successfully implemented a CFT-based model to simulate the transport of TiO₂ nanoparticles (nTiO₂) in their column experiments. *Fang et al.* [22] observation of nTiO₂ deposition, however, is contradictory to the *Guzman et al.* [29] report of a slow increase with time in the passage of anatase, the most dominant form of mineral TiO₂, NPs through a two-dimensional model of porous structure. *Guzman et al.* [29] suggested that the mobility of NPs increased with time as deposition sites became saturated, which is conceptually in concert with a MFT model. These differences in the transport behavior for NPs of the same material clearly demonstrate the controlling effect of the porous medium and solution chemistry as well as the inherent properties of NPs.

1.2.1.2. Physical Filtration (i.e. Straining)

Some of the discrepancies between particle transport data and CFT predictions have been explained by the CFT's failure to consider particle straining [19, 30, 31]. Straining is the trapping of particles in the downgradient pore throats that are too small to

allow particle passage. Nanoparticles may aggregate to become large enough to exceed pore throat sizes where they may be removed from the flowing phase through physical screening or straining.

The magnitude of particle retention by straining depends on both the particle and porous medium properties. *Bradford et al.*[32] proposed the following simple form for a particle mass transfer term between the aqueous and solid phases due to straining:

$$E_{sw}^{str} = \frac{\partial(\rho_b \omega)}{\partial t} = \phi S_w k_{str} \psi_{str} C \quad (1.6)$$

where E_{sw}^{str} [mol L⁻¹ s⁻¹] is the mass transfer due to straining, k_{str} [s⁻¹] is the straining coefficient, ψ_{str} [-] is a dimensionless particle straining function. *Bradford et al.*[32] proposed the following phenomenological power-law function to represent ψ_{str} :

$$\psi_{str} = \left(\frac{d_{50} + z}{d_{50}} \right)^{-\beta} \quad (1.7)$$

where d_{50} [m] is the median sand grain size, β [-] is a parameter that controls the shape of the spatial distribution of strained particles, and z [m] is the distance from the column inlet. *Bradford and Bettahar* [33] assumed that oocyst retention by straining occurred primarily at the column inlet because oocysts were retained in dead-end pores that were smaller than “some critical size”. They hypothesized that the number of dead-end pores decreases with increasing travel distance because of size exclusion and/or limited advection and transverse dispersivity that tend to keep mobile oocysts within the larger networks, thus bypassing smaller pores. *Bradford et al.* [32] suggested a value of $\beta = 0.432$ for retained carboxyl latex colloids ($d_p/d_{50} < 0.02$).

Xu et al. [31] found that clean bed straining rates are generally zero below a threshold $d_p/d_{50} = 0.008$ and increase linearly as d_p/d_{50} increases from 0.008 to

0.052. However, *Bradford et al.* [32] report a threshold value of 0.002 after which straining rates scale exponentially with d_p/d_{50} according to the following power function:

$$k_{str} = 269.7 \left(\frac{d_p}{d_{50}} \right)^{1.42} \quad (1.8)$$

1.2.2. Modeling Particle-Particle Interactions (i.e. Aggregation)

Stability of nano-particles in aqueous systems is a key factor controlling their transport and ultimate fate in aqueous environments [1]. Particle-particle interactions (i.e. aggregation) have reportedly influenced the particle-soil grain interactions (i.e. deposition), thus affecting their transport in porous media in a number of studies [9, 22, 34]. Therefore, an understanding of particle-particle interactions is imperative when considering the transport of NPs in natural environments [18]. The environmental fate of NPs is considered to be “predominantly affected by coagulation-breakup mechanisms”, as opposed to “removal by settling” [5]. Unlike colloidal suspensions that have a higher propensity for precipitating out of the aqueous phase, well-dispersed nano-particles may travel long distances in aquatic environments and thus have more opportunities to interact with and cause potential harm to their receptors. Hydrodynamic particle sizes have been observed to be substantially larger than the individual particle size in the dry phase for many nano-materials.

Experimental evidence confirms that nanoparticles interact with one another to form larger aggregates (e.g., *Elzey and Grassian* [35] and *Li et al.* [36] report nAg aggregation in batch and column transport experiments, respectively). *Lin et al.* [1] present this phenomenon as an indication that aggregation is a common process for NPs in water. The aggregation process is controlled by the properties of the NPs (e.g. size,

chemical composition, surface charge, surface roughness and heterogeneity), and chemistry of the aqueous phase (e.g. ionic strength, pH, and NOM) [37]. Where the main difference of NPs from their bulk counterparts is related to their surface/volume ratio [12], aggregation may reduce the overall specific surface area of nano-particles, limiting their reactivity.

Theoretically, the kinetics of particle aggregation depends on the height of their energy barrier [38]. Particles that overcome the energy barrier will aggregate with another particle in a deep primary energy minimum. The height of the energy barrier for deposition or aggregation depends directly on the size of the interacting particles, with smaller particles exhibiting much lower energy barriers [18, 20]. Therefore, it is expected that nanoparticles aggregate more in the primary minimum than micrometer-sized particles. It has been suggested that nanoparticles that aggregate in primary energy minima are less likely to break apart following changes in solution chemistry, such as reduction of ionic strength or changes in solution pH [39].

Three transport mechanisms govern the collision of particles during aggregation: (1) *Brownian* diffusion (perikinetic aggregation), (2) fluid motion (orthokinetic aggregation), and (3) differential settling. For nanoparticles, *Brownian* diffusion is the predominant mechanism of aggregation with negligible contribution from fluid shear and sedimentation [18]. Based on *Smoluchowski's* formulation [40] the following 2nd-order expression for the time rate of change of number concentration of aggregates of rank k due to perikinetic aggregation is written as [38]:

$$\frac{dn_k}{dt} = 1/2 \sum_{i=1}^{k-1} h_{i,k-i} n_i n_{k-i} - n_k \sum_{i=1}^{m-k} h_{i,k} n_i \quad (1.9)$$

where $n_i[\text{m}^{-3}]$ denotes the concentration of i -size clusters, m is the maximum size of an aggregate that can form in the system, and $h_{i,j}[\text{m}^3/\text{s}]$ is the second order attachment constant of clusters of rank j to clusters of rank i . $h_{i,j}$ can be estimated from the following expression derived based on *Stokes-Einstein* equation under favorable conditions for aggregation [38]:

$$h_{i,j} = \frac{2}{3} \frac{k_B T}{\mu} \frac{(d_{p_i} + d_{p_j})^2}{d_{p_i} d_{p_j}} \quad (1.10)$$

where $k_B [=1.381 \times 10^{-23} \text{J/K}]$ is the *Boltzmann* constant, T [K] is the absolute temperature, μ [$\text{g m}^{-1} \text{s}^{-1}$] is the fluid density, and d_{p_i} [m] is the diameter of i -rank aggregates. Under unfavorable conditions for aggregation, which is the case for most of NPs subject to natural solution chemistry (e.g., pH and ionic strengths), once the favorable aggregation rate is established, the attachment efficiency for aggregation $\alpha_{PP}[-]$ needs to be determined. α_{PP} at a given solution chemistry can be computed by normalizing the obtained aggregation rate constant with the favorable aggregation rate constant. Using Dynamic Light Scattering (DLS), α_{PP} can be obtained from the slopes of the initial change of the hydrodynamic radius with time [18]:

$$\alpha_{PP} = \frac{\frac{1}{N_0} \left(\frac{da_h(t)}{dt} \right)_{t \rightarrow 0}}{\frac{1}{N_{0, fav}} \left(\frac{da_h(t)}{dt} \right)_{t \rightarrow 0, fav}} \quad (1.11)$$

where the subscript *fav* denotes favorable aggregation, N_0 [m^{-3}] is the initial particle number concentration, and a_h [m] is the hydrodynamic radius of aggregates. An alternative approach to the DLS method would be to estimate α_a from the following DLVO-based expression [38]:

$$\alpha_a = \kappa d_{p_i} \exp\left(-\frac{V_{max}}{k_B T}\right) \quad (1.12)$$

where κ [m^{-1}] is the inverse Debye length, d_{P_i} [m] is the diameter of particle i , and V_{max} [J] represents the energy barrier height.

When particles attach, the hydrodynamic size of the resulting cluster will be greater than that of the attaching particles (or aggregates). The increase in cluster diameter can be accounted for by taking two alternative approaches [38]. The first approach involves the assumption of spherical colliding particles, implying that ‘*coalescence*’ of particles occur after collision. The alternative approach is to recognize aggregates as ‘*fractal objects*’. According to this approach the relationship between an aggregate mass, M , and size d_p , is:

$$M \propto d_p^{D_f} \quad (1.13)$$

where D_f [-] is a mass fractal dimension varying from 3 for regular 3-dimensional objects (e.g., spheres) to considerably less than 3 for irregular aggregates. *Lin et al.* [41] suggested a fractal dimension of 1.8 for diffusion-limited aggregation as opposed to a higher fractal dimension of 2.1 for the case of reaction-limited aggregation (i.e. more compact aggregate structures in the presence of repulsive forces).

Chatterjee and Gupta [21] developed a mathematical model for the transport of aggregating particles by coupling the ADR equation with *Elimelech et al.*’s aggregation model. However, they developed their numerical model under the assumption of “no aggregation” to occur within the porous medium. That is, the coupled transport/aggregation mathematical model reduced to a transport-only model after numerical implementation.

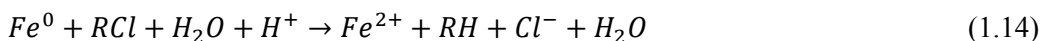
1.2.3. Modeling Particle-Dissolved Phase Interactions (i.e. Chemical Reactions)

It is of critical importance to know not only the behavior of NPs but also that of dissolved species that coexist and evolve along with NPs once particles are discharged into aquatic environments [36]. Based on their composition, NPs can chemically interact with dissolved solutes (e.g., reductive dechlorination reaction of chloroethenes by nano-scale zero-valent iron particles (nZVI)). NPs may also become sources for (e.g., dissolution of nano-scale silver particles (nAg) and of zinc oxide nanoparticles (nZnO)) or sinks of (e.g., sorption of heavy metal ions to nZVI) dissolved constituents in aqueous systems.

While the strong reductive properties of some NPs (e.g., nZVI) render them effective remedial agents for removing a wide range of environmental pollutants (e.g., chlorinated solvents and heavy metals), dissolved-phase interactions of other NPs, such as nAg and quantum-dots, may increase their environmental impact through the enhancement of environmental exposure caused by downstream plumes originating from these NPs. Because of their relevance to this study, existing modeling approaches for describing the dissolved-phase interactions of (1) nZVI and (2) nAg are discussed in more detail in Subsections 1.2.3.1 and 1.2.3.2.

1.2.3.1. nZVI-driven Reductive Dechlorination

nZVI has been shown to reduce many chlorinated methenes, ethenes, and other halogenated organic compounds at ambient temperature [42], via the general reaction:

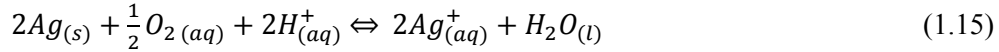


In most studies, the dechlorination reaction of chloroethenes by Fe^0 is modeled by pseudo-first-order kinetics with respect to contaminant concentration [43-45]. The one exception to this was a batch study conducted under iron-limited conditions, (a molar Fe^0

: TCE ratio of ~2.9), where the product formation showed a clear lag phase (~10h of slow reaction), followed by 2-3 days of steady rapid reaction, and a final period where the reaction slowed and eventually stopped [46].

1.2.3.2. Oxidative Dissolution of nAg

An understanding of nAg environmental effects is complicated by the coexistence of the particle and ionic forms, which likely exhibit different fate and transport characteristics, and may have independent or synergistic toxicity pathways [47]. Ion release from nAg has been shown to be a cooperative oxidation process requiring both dissolved oxygen and protons. It produces unstable peroxide intermediates, and proceeds to complete reactive dissolution. The following global reaction stoichiometry is suggested for the oxygen-mediated ion release from nAg in the absence of other oxidants [47, 48]:



Liu and Hurt [47] presented an empirical kinetic law for nAg dissolution for the low nAg concentrations used in their experiments which they claim as “most relevant to the environment”. The total silver concentration range in their experiments was 0.05 - 2.0 mg/L diluted from 40 mg/L stock nAg suspension. Their empirical relationship is expressed as:

$$\frac{\partial C_{nAg}^{aq}}{\partial t} = -\hat{A} \cdot SSA \cdot e^{-E/RT} \left(\frac{[H^+]}{10^{-7}M} \right)^{0.18} e^{-a[NOM]} C_{nAg}^{aq} \quad (1.16)$$

where C_{nAg}^{aq} [mmol/L] is the suspended concentration of nAg in the aqueous phase, $E = 77$ kJ/mol, $a = 0.083$ L/mg, and $\hat{A} = 7.6 \times 10^{16}$ $\mu\text{g}_{\text{release}}/\text{day} \cdot \text{m}_{\text{particle surface}}^2$ is a dissolution rate constant normalized on a particle surface area basis. SSA [$\text{m}^2/\mu\text{g}$] is the

specific surface area of nAg particles and [NOM] [mg/L] is the concentration of the natural organic matter. These authors concluded, however, that more investigation is required to develop a full kinetic model of nAg oxidation.

More recently, *Zhang et al.* [48] developed a kinetic model to describe Ag^+ ion release from nAg using the *Arrhenius* equation. Although, a general first-order reaction model successfully captures their Ag^+ release data, the fitted ion release rate constants exhibited significant discrepancy from expected values from their kinetic model.

1.2.4. Modeling Particle-Water/NAPL Interface Interactions

For nanoparticles transporting through saturated porous media containing DNAPL ganglia, the particles can collide with and attach to soil grains, aggregate, and lead to pore clogging and straining, or collide with and stick to entrapped DNAPL as shown in Figure 1.1 (borrowed from *Saleh et al.* [13]).

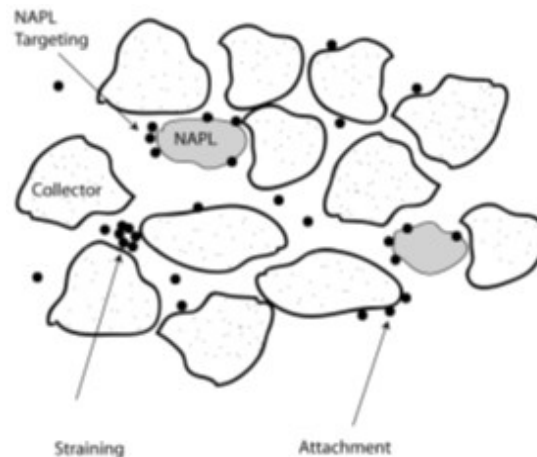


Figure 1-1. Conceptual model of nZVI transport showing filtration, straining, and DNAPL targeting [13].

Studies of capillary interactions have shown that colloidal particles tend to localize at liquid-liquid interfaces when the energy of the two contacting liquids is large compared to the difference between the energies of the two particle-liquid interfaces [49].

In the case of a high energy liquid-liquid interface (e.g., DNAPLs and water), particles with a broad range of moderately hydrophobic coatings are expected to adhere spontaneously to the interface [50]. This is congruous with *Saleh et al.*'s observation of triblock copolymer coated nZVI localized at the TCE-water interface [51].

To date, only a few studies have directly addressed the fate and transport of NPs in porous media containing a secondary NAPL phase [13, 50, 51]. Furthermore, neither of the above mentioned partitioning experiments; except for the study conducted by *Bishop et al.* [50], have taken a quantitative approach to characterizing the nanoparticle transport behavior to the water/NAPL interface.

Saleh et al. [13] performed a bench-scale column study to investigate polymer-coated nZVI targeting of residual dodecane ganglia. They conducted their experiments using 12.5 cm long (1.09cm i.d.) columns packed with silica sand (porosity of 0.33) at a water velocity of 4.66m/day. Injection of 1PV of nZVI suspension was followed by a period of flow interruption to allow for particle diffusion and attachment to the dodecane coated sand. Flow was resumed after 24 hours to flush the column with a 1mM NaHCO₃ solution. *Saleh et al.* [13] did not share any data regarding either the spatial distribution or breakthrough of nZVI. Nevertheless, they suggested that NPs transport behavior was predominantly influenced by the stabilizing particle coating. While bare nZVI was captured completely in both DNAPL-containing and DNAPL-free columns, nZVI modified with polyaspartic acid did not demonstrate any affinity for dodecane-containing sand and eluted completely, as it did for clean sand columns. However, for the nZVI coated with PMMA/PSS polymer with a high hydrophobe/hydrophile ratio, particle elution was lower (~90%) than it was for a clean sand column (~100%). *Saleh et al.* attributed this enhancement in nZVI retention to nZVI adsorption to the dodecane-water

interface. They also speculated that nZVI adsorption was likely to be enhanced for a better solvent for PMMA (e.g., TCE).

More recently, *Bishop et al.* [50] conducted a series of column experiments to study the transport of micrometer-size ZVI particles coated with hydrophobic and moderately hydrophobic anionic polymers in saturated porous media containing uniformly distributed DNAPL ganglia. They reported that ZVI particles modified with two moderately hydrophobic polymers (carboxymethylcellulose and polyacrylate) had up to 30-fold higher attachment coefficient to the model DNAPL surface than they did to the sand surface. They also found that below about 7cm (total length of ~25cm) the iron retention profiles were close to the prediction of the *Tufenkji and Elimelech's* model [24] for particle filtration in the clean-bed limit. They implemented the following CFT-based approach to simulate the ZVI retention profiles:

$$\ln\left(\frac{c}{c_0}\right) = -[(1 - \chi)\alpha_{sand} + \chi\alpha_{DNAPL}]\lambda L \quad (1.17)$$

where χ [-] is the fraction of DNAPL coated sand grains, α_{sand} [-] and α_{DNAPL} [-] are attachment efficiencies for clean sand and for sand containing dichlorobenzene residuals, respectively. L [m] is the column length, and λ [m⁻¹] is the filter coefficient expressed as:

$$\lambda = \frac{3}{2d_c}(1 - \phi S_w)\eta_0 \quad (1.18)$$

Retained ZVI concentrations, however, clearly followed a hyper-exponential pattern (indicative of possible role of particle straining). Moreover, they did not discuss ZVI concentrations eluted from sand columns nor the general experimental conditions under which they conducted their experiments (e.g., flow velocity and DNAPL saturation).

A few investigations within the biocolloidal field have addressed the effect of a residual NAPL phase on bacterial transport through porous media [52, 53]. *Rogers and Logan* [52] found that the presence of a residual saturation of PCE varying between 15 to 21% decreased the retention *Pseudomonas fluorescens* P17 by 41% in quartz sand and by 22% in soil columns. This is inconsistent with the enhanced particle retention due to presence of a NAPL phase reported for non-biological colloids. They attributed this effect to the formation of a large fraction of immobile water in their column. Therefore, their results could not be interpreted with respect to specific influence of NAPL/bacteria interactions [53].

Link et al. [53] reported that coating 20% of the quartz grains with hexadecane as a model NAPL increased the retention of *Pseudomonas Saccharophilia* P15 by as much as a factor of 26 compared to the retention exhibited in NAPL-free quartz sand. They used the analytical solution to a 1-D extension of ADR equation with a first-order bacterial retention term to fit the experimental breakthrough curves.

The presence of a NAPL phase can also affect the ultimate fate of NPs in porous media by providing long-term sources of dissolved constituents reacting with NPs. Such effects were outlined in Subsection 1.2.3 of this dissertation.

1.2.5. Modeling Particle Non-Uniformity

Different NPs can have different physiochemical properties including hydrodynamic diameter and reactivity. Particle size plays a key role in determining the forces that control particle transport and capture in porous media. While *Brownian* diffusion is the dominant transport mechanism for nano-scale particles, the transport of larger aggregates could be governed by straining, interception, and gravitational sedimentation. NPs can originally exhibit a size distribution or can aggregate with other

NPs to possess different effective hydrodynamic diameters. On the other hand, NPs may exhibit different levels of reactivity depending upon their reactive content and/or the available surface reaction sites.

Conventional modeling schemes, based upon the numerical discretization of classical transport equations, however, are usually incapable of taking into account particle non-identicalities. Some modelers like *Chatterjee and Gupta* [21] have attempted to resolve this limitation by separately solving the transport equation for aggregates of varying ranks (i.e. n transport PDEs for colloidal monomers, dimers, trimers, and n -mers) with second order production/decay terms for particle aggregation. Nevertheless, they make the very big assumption that no aggregation occurs after introduction of colloidal suspensions in the porous media, failing to couple the aggregation model with the particle transport model. This example demonstrates the difficulties in representing even the most basic and mathematically-well-established mechanisms that lead to irregular particles using conventional (*Eulerian*) numerical approaches.

1.3. Eulerian Method vs. Lagrangian Method for Solving the Transport Equation

Different methods have been implemented to solve ADR equations. For some simple cases, the transport equation can be solved analytically under a number of simplifying assumptions including but not limited to a constant retardation factor, reaction rate, constant velocity, and simplistic realization of initial and boundary conditions. For more complicated problems, however, numerical approximations are used to solve the transport equation. Numerical methods for solving the ADR equation are generally classified as *Eulerian*, *Lagrangian*, or mixed *Eulerian-Lagrangian*. The *Eulerian* specification of transport is a way of looking at mass transport that focuses on specific locations in space through which the mass is transported as time passes. The

Lagrangian specification of transport, on the contrary, is a way of looking at mass transport where the observer follows individual parcels containing the mass of a component of interest as they move through space and time [54]. In *Lagrangian* methods, the transport equation is solved either in a deforming grid, or in deforming coordinates in a fixed grid. A primary example of the *Eulerian* method for solving the transport equation is the method of Finite Differences (FD) which discretizes space and time in intervals. On the other hand, different *Lagrangian* transport schemes have been implemented in the past that include method of Continuous-Time Random-Walks (CTRW) and the Random-Walk Particle-Tracking (RWPT) method. The latter method (i.e. RWPT) provides a stochastic solution for dispersive transport in porous media. The RWPT method is of great relevance to this study, and thus is presented in more detail in Subsection 1.3.2.

1.3.1. Deterministic Eulerian transport (e.g., Method of Finite Differences)

The FD method is a well-established numerical method which has been extensively applied for flow and transport modeling [54]. A difference equation for transport of a component can be obtained by taking the mass balance of that component over each cell of a grid. Mass balance over each cell requires that over a time interval inputs and outputs due to storage, advection, dispersion-diffusion, and reaction sum to zero [55]. FD has proven effective method for solving transport problems where advection does not dominate dispersive forces, yet it does not allow taking into account non-identical particles. In reality, though, NPs may behave physically and chemically different based upon a number of different factors including their hydrodynamic size and age, a shortcoming which does not apply to the case of dissolved species. A detailed description of the FD technique is beyond the scope of this dissertation.

1.3.2. Stochastic Lagrangian transport (e.g., Random-Walks Particle-Tracking Method)

Lagrangian methods treat mass transport by tracking a large number of moving particles, and avoid solving the ADR equation directly. As a result, these *Lagrangian* methods are free of numerical dispersion and particularly effective for handling advection-dominated transport problems. The RWPT method is a typical example of the *Lagrangian* approach [54]. A widely used transport model based on the RWPT method is given by *Ahlstrom et al.* [56] and *Prickett et al.* [57]; the RWPT method has been applied to the analysis of diffusion and dispersion in groundwater since the “1950s” [55]. Since then this methodology has been implemented in numerous studies to simulate mass transfer processes (e.g., *Salamon et al.* [58]) and the transport of dissolved (e.g., *Ahlstrom et al.* [56]) and particulate (e.g., *Scheibe and Wood* [59]) components through porous (e.g., *Ahlstrom et al.* [56]) and fractured (e.g., *Schwartz et al.* [60]) media in saturated (e.g., *Ahlstrom et al.* [56]) and multiphase (e.g., *Garven and Freeze* [61]) systems. In this Subsection, the principle of the random-walks method will be described, and some of the more important aspects of *Lagrangian* methods will be highlighted. The presented material herein is mainly borrowed from *Kinzelbach* [55].

The original RWPT method uses tracer particles for the description of mass transport. Each particle is assigned a specific mass and is moved in the flow field. The sum over all particle masses constitutes the total amount of tracer injected into the system. Dispersion is modeled by superimposing the advective particle movement with a random movement possessing statistical properties of the dispersive process. By considering many individual particle paths (i.e. random-walks) a dispersing particle could be modeled, which presents a distribution of mass (of a dissolved solute or of particulate matter). The concentration distribution is arrived at by overlaying a grid and counting the

number of particles per grid-cell. Sources and sinks must be simulated by adding or destroying particles. The incorporation of boundary conditions is done by adding or abstracting particles in a cell such as to keep the concentration at a prescribed value.

The basic concepts of the RWPT method are easily demonstrated by looking at the simplest one-dimensional transport problem. An instantaneous release of mass ΔM of an ideal tracer at location $x = 0$ yields the concentration gradient at time t :

$$C(x, t) = \frac{C_0}{\sqrt{4\pi\alpha_L v_w t}} \exp\left(-\frac{(x-v_w t)^2}{4\alpha_L v_w t}\right) \quad (1.19)$$

with $C_0 = \Delta M / (n_e m_w)$ and velocity in positive direction. Here C_0 [mol/L] is the molar concentration at the injection point, α_L [m] is the dispersivity coefficient, and v_w [m/s] is the flow velocity. For a fixed time t , this distribution can be viewed as a normal distribution around an average x -value, $\bar{x} = v_w t$, with a standard deviation $\sigma = \sqrt{2\alpha_L v_w t}$. The same distribution can be generated stochastically. If the pore velocity is a function time and location the random path of particle p , $x_p(t)$, must be determined in discrete time steps Δt . Using *Euler*-integration and starting at time $t = 0$ the following expression is derived:

$$x_p(t + \Delta t) = x_p(t) + u(x_p(t), t)\Delta t + Z\sqrt{2\alpha_L |u(x_p(t), t)|\Delta t} \quad (1.20)$$

where Z [-] is a normally distributed random variable with average 0 and standard deviation 1, and u [m/s] is the corrected velocity proposed by *Kinzelbach* that is expressed as [55]:

$$u(x_p(t), t) = v_w(x_p(t), t) + \frac{\partial D_L}{\partial x} \quad (1.21)$$

Direct implementation of flow velocity v_w yields results that are only approximatively correct, because as shown by *Ito* [62] the space-time probability distribution of an ensemble of particles using v_w -values fulfills the *Fokker-Planck* equation which is very similar to but not identical with the one-dimensional transport equation. However, a direct analogy with the transport equation is achieved when the corrected velocity, u , is used instead of the actual velocity, v_w .

Simple first-order chemical reactions have been incorporated in to the RWPT schemes in two ways. One is to assign every particle a mass $M_p(t)$ which decreases in time according to:

$$M_p(t) = M_p(0)\exp(-\lambda t) \quad (1.22)$$

Alternatively, particles can be destroyed with a constant probability as first-order reaction corresponds to a decay with constant probability. The probability p [-] of decay and the reaction constant λ_d [s^{-1}] are linked:

$$p = \lambda_d \Delta t \quad (1.23)$$

For sufficiently small Δt , *Kinzelbach* [55] recommends the former method as it prevents a depletion of particles which would lead to statistically insignificant results.

A very large number of particles is usually necessary to attain satisfactory results [55], as the statistical fluctuation is inversely proportional to the square root of the number of particles in cell [63]. *Kinzelbach* [55] recommends considering only concentrations calculated from 20 or more particles per cell. The RWPT method does not exhibit numerical dispersion, however, due to the small number of model particles which enhance the stochastic noise, the results at the dispersive edges of the plumes are usually

not statically significant. On the whole, the RWPT method is considered a robust method which can easily be put on the top of every flow model because of the simplicity of the explicit equations. Besides, due to the use of particles as discrete mass parcels, global mass conservation is automatically satisfied [63].

A big disadvantage of the RWPT method, however, is revealed in sensitivity analyses. For parameters with low sensitivity, the physical variations of concentration due to variations in the parameter may be masked by stochastic variations of concentration [55]. In addition, stochastic noise in the model outputs prohibits its applicability to inverse problems. Another issue with the use of the RWPT method is the potentially time and memory intensive simulations as the reactive transport equation must be solved separately for each individual particle in a large population of model particles.

1.4. Summary and Significance

Widespread use of nanotechnology products in the recent years inevitably results in introduction of nanomaterials to the environment. Environmental impacts of such materials, however, are not well understood in spite of ongoing research. Moreover, certain nanomaterials can be employed as remedial agents. Effective employment of such nanomaterials for environmental remediation requires their efficient delivery to the contaminated zones, which in turn is again ultimately dependent upon an accurate knowledge of the environmental fate and transport of nanoparticles.

While there has been substantial effort to understand the transport of NPs in model porous media, and also to identify the chemical fate of NPs in aquatic environments, a lack of adequate knowledge still prevails in the following areas:

- (1) Little attention has been brought to address the reactive transport of NPs in porous media, quantitatively.

- (2) To the best of the writer's knowledge, previous efforts to model the transport of NPs have failed to tackle two challenging aspects of simulating the fate and transport of nanoparticles in porous media: (1) the effects caused by the non-identity of NPs on their transport and reactivity in subsurface and (2) processes that can result in particle non-identity (e.g., particle aggregation and/or particle-specific chemical reactions). This shortcoming is a result of technical limitations inherent in conventional numerical methods (e.g., FD and FE). Numerous experimental reports, however, have indicated that NPs can exhibit a non-uniform particle-size distribution, aggregate to form non-identical groups of particles, and/or possess various reactivity-levels.

The focus of the presented research was to:

- (1) Provide a modeling tool to allow mechanistic quantification of the effects of physiochemical factors and mechanisms controlling the fate and transport of NPs in the subsurface.
- (2) Account for particle non-identity effects on the fate and transport of NPs as well as processes that lead to non-identity.

1.5. Research Objectives

The two main goals for this dissertation are outlined here, and the objectives associated with the respective goals are briefly described.

Goal 1. Development of a hybrid one-dimensional (1-D) *Eulerian-Lagrangian* numerical simulator for modeling the coupled reactive transport of nanoparticles and dissolved constituents in porous media.

Objective 1. This simulator should be capable of accounting for:

- a. Particle-soil grain interactions (i.e. deposition and detachment)
- b. Particle-dissolved species interactions (i.e. chemical reactions)
- c. Particle-particle interactions (i.e. aggregation)
- d. Particles that exhibit a particle size distribution
- e. Particle-water/NAPL interface interactions (i.e. interfacial partitioning).

Goal 2. Applying the developed numerical simulator to investigate the fate and transport of nanoparticles and coexisting and interacting dissolved constituents in porous media. The hybrid simulator will be employed to study the following phenomena:

Objective 2. Reductive dechlorination of chlorinated solvents by zero-valent iron nanoparticles in DNAPL source zones.

Objective 3. Fate and transport of dissolving silver nanoparticles and the emerging dissolved silver ions.

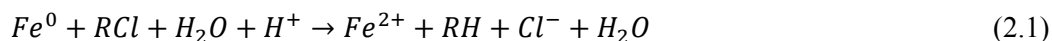
Objective 4. Particle-particle interactions and their effects on the particle-soil grain interactions (i.e. transport and deposition).

Objective 5. Effects of particle-water/NAPL interface interactions on the transport of nanoparticles.

Chapter 2 EFFECTIVENESS OF NANO-SCALE ZERO-VALENT IRON FOR TREATMENT OF PCE-DNAPL SOURCE-ZONES

2.1. Introduction

Significant effort has been directed toward the development of remediation technologies that are capable of transforming contaminants *in situ*, thereby minimizing or eliminating the need for contaminant extraction, above-ground treatment and containment. Of these technologies, elemental iron (Fe^0) or zero-valent iron (ZVI), is of particular interest because it is a strong reducing agent and has been shown to reduce many chlorinated methenes, ethenes, and other halogenated organic compounds at ambient temperature[42], via the general reaction:



Millimeter to sub-millimeter-sized Fe^0 particles have been used for groundwater remediation for approximately two decades through the emplacement of permeable reactive barriers (PRBs) designed for *in situ* treatment of contaminant plumes [64]. Fe^0 particles have been shown to effectively transform chlorinated contaminants at much faster rates than other technologies, including bioremediation, under typical subsurface conditions [65]. For example, *Pooley et al.* [66] observed biologically-mediated dechlorination rates for PCE in the range of $3.33 \times (10^{-4}-10^{-5}) \text{ hr}^{-1}$, which is 1 to 2 orders-of-magnitude lower than Fe^0 -induced PCE reduction rates reported by Arnold and

Roberts [67]. In addition, it is well known that complete biological dechlorination of trichloroethene (TCE) follows the sequence of TCE, cis-dichloroethene (cis-DCE), vinyl chloride (VC), and finally ethane [68], while, Fe^0 reduces TCE directly to acetylene, ethene, and ethane, with only trace production of cis-DCE and VC [46].

The rapid development of the field of nanotechnology has stimulated research into the application of nano-scale zero-valent iron (nZVI) particles in soil and groundwater remediation [42, 69]. The intent of this approach is to capitalize on the greater specific surface area [46], enhanced reactivity [70] and mobility [71, 72], and potential for interfacial accumulation [51, 73] of nZVI to achieve more rapid and cost effective destruction of contaminants in comparison with conventional iron-based materials. Highly concentrated aqueous slurries (e.g., 10 g/L) of nZVI have been injected directly into the subsurface at, or immediately down-gradient from, the source of contamination, with the goal of utilizing nZVI as a targeted reactant [74, 75], in contrast to applications that rely on transport to a passive downstream barrier zone [76, 77].

The majority of the research on dehalogenation reactions mediated by Fe^0 particles, however, has involved batch studies that employ dissolved contaminant concentrations and total mass loadings that are much lower than those typically observed within DNAPL source zones (i.e., < 20 mg/L) [43-45, 65, 67, 73, 78-80]. Similarly, field-scale nZVI demonstration projects have focused on the treatment of relatively dilute dissolved phase contaminant plumes, using an groundwater extraction/reinjection system [75] and direct injection of nZVI under gravity feed [74], with initial TCE concentrations of less than 20 mg/L and 1 mg/L, respectively. In contrast, very few studies have examined the effectiveness of nZVI at higher contaminant concentrations (e.g. *Liu et al.* [46]; 290 mg/L TCE), consistent with a prolonged contaminant source (i.e., DNAPL).

Design of effective nZVI remedial strategies for DNAPL source zones will require a detailed understanding of the mechanisms and processes governing nanoparticle

delivery, contaminant mass transfer, and reductive dechlorination in dynamic subsurface systems. Based upon this conceptual understanding, mathematical models can be developed to represent the coupling of these processes, serving as effective design tools. The kinetics and pathways of the reductive dechlorination reaction of chloroethenes by Fe^0 s have been the subject of extensive research [43, 45, 46, 67, 78, 81]. In most studies, the dechlorination reaction of chloroethenes by Fe^0 is modeled by pseudo-first-order kinetics with respect to contaminant concentration [43-45, 65, 73, 79, 80, 82]. However, most of the investigations that utilized a pseudo-first-order model were carried out under low contaminant concentrations (representative of a downstream plume) where iron was in excess. In addition, to the best of our knowledge, there has been no effort to model the simultaneous transport and nZVI-driven reduction of chlorinated ethenes within DNAPL source zones.

To address the knowledge gaps discussed above, a mathematical modeling study was conducted to investigate the results of a series of column experiments performed by Dr. Jed Costanza. The chemical reactivity of nZVI particles in a one-dimensional (1D) column containing two fluid phases, water and tetrachloroethene (PCE)-DNAPL was evaluated. The column experiment was designed to represent a highly-contaminated source zone, in which PCE-DNAPL was entrapped at residual saturation and a concentrated nZVI suspension was injected to achieve a “best-case” delivery scenario. Water was then flushed through the column and effluent samples were collected continuously and analyzed for the parent compound (PCE) and relevant transformation products (e.g., TCE, ethene). A numerical simulator was developed and utilized to assess the ability of the mathematical model to reproduce the experimental results. The fitted reaction rate, obtained under flowing conditions, was employed in model sensitivity analyses to evaluate the conditions (i.e., initial contaminant to iron molar ratio, spatial

distribution of nZVI, and retention time) required to achieve complete transformation of PCE to ethene.

2.2. Materials and Methods

The experimental information disclosed in this Subsection is not a part of this dissertation. The results of the described experiments (conducted by **Dr. Costanza, J.**) were used in subsequent numerical simulations.

The nZVI reactivity experiments were conducted in 15.8-cm long Kontes® (Kimble-Chase, Vineland, NJ) borosilicate glass columns with an inside diameter of 2.5 cm, equipped with high density polyethylene end plates. The columns were orientated vertically, and packed with 20-30 mesh Ottawa sand (U.S. Silica, Berkeley Springs, WV) under vibration. Following dry packing, the column was saturated with CO₂ gas for 15 minutes at a flow rate of 50 mL/min to facilitate dissolution of entrapped gas during water saturation. De-aired water containing 3.5 mM of calcium chloride was then introduced into the column (Masterflex peristaltic pump, Cole-Parmer, Vernon Hills, IL) in an up flow mode at a flow rate of 2 mL/min until the column was completely saturated. The aqueous pore volume (PV, ca. 28 mL) was determined from the difference in column weight before and after water saturation. A residual saturation of PCE-DNAPL was established by injecting approximately 20 mL of PCE-DNAPL through the bottom (up flow mode) of the water-saturated column at a flow rate of 2 mL/min. Approximately two PVs of de-aired water were then introduced through the top of the column (down flow mode) at a flow rate of 2 mL/min to displace mobile PCE-DNAPL from the column. Two additional pore volumes of de-aired water were then injected into the column in an up flow mode to displace any additional PCE-DNAPL. Following the establishment of residual PCE-DNAPL (saturation = 5.5%, 2.52 g), an aqueous suspension of nZVI (RNIP 10DS, Toda American Inc., Schaumberg, IL) was introduced into the column in a down

flow mode. The nZVI suspension was prepared by pipetting 40 mL of nZVI stock solution into a 1 L Morton flask (Ace Glass Inc., Vineland, NJ) containing de-aired water with 3.5 mM of calcium chloride. The Morton flask was stirred with an impeller rotating at a rate of 200 revolutions per minute, and the stirred suspension was then transferred to the column inlet using a Masterflex peristaltic pump through 1/8-inch outside diameter Teflon® tubing. The average concentration of nZVI at the column inlet was 63.5 ± 3.1 g/L (total iron = $\text{Fe}^{2+} + \text{Fe}^{3+}$), as determined from 6 samples collected during the introduction of nZVI. Emplacement of nZVI throughout the column was achieved by injecting 22.5 pore volumes of the nZVI suspension to the top of the column (downflow mode) at a flow rate of 5 mL/min, which resulted in the emplacement of 40.1 ± 2.0 g of nZVI within the column. During introduction of the nZVI suspension, a small amount of PCE-DNAPL was displaced from the column, reducing the initial residual PCE-DNAPL saturation to 5.4% (2.47 g). Following nZVI delivery, de-ionized (DI) water containing 3.5 mM calcium chloride was continuously pumped through the column in the downward direction at a flow rate 0.25 mL/min for 238 pore volumes. Aqueous effluent samples were collected periodically to determine the concentration of dissolved phase PCE exiting the column, along with potential reaction products including TCE, DCE, VC, and ethene. After 238 pore volumes of water flushing, the column was rinsed with 6.5 pore volumes of isopropanol (IPA, Thermo Fischer Scientific, Waltham, MA) to extract the mass of PCE remaining in the column. Two additional column studies were conducted under similar conditions to confirm results obtained for the experiment reported herein.

2.2.2. Analytical Methods

Aqueous effluent samples and IPA extracts were analyzed for PCE, TCE, cDCE, VC, and ethene content using a Model 6890 Hewlett-Packard gas chromatograph (GC) equipped with a Tekmar® HT3 headspace autosampler (Teledyne Technologies, Inc.,

Mason, OH) and a 30 m long by 0.25 mm outside diameter (OD) DB-5 column (Agilent, Santa Clara, CA) with 0.25 μm film thickness connected to a flame ionization detector (FID). Aqueous samples were introduced using the headspace autosampler, which was programmed to heat samples for 30 min at 70 $^{\circ}\text{C}$ prior to transferring 1 mL of headspace gas into the GC inlet through heated silco-steel tubing. The GC oven was maintained at 35 $^{\circ}\text{C}$ for 7 min, and then increased at a rate of 10 $^{\circ}\text{C}/\text{min}$ to 60 $^{\circ}\text{C}$. Aqueous calibration standards were prepared by injecting small volumes ($< 10 \mu\text{L}$) of a methanol stock solution containing PCE into 22 mL headspace vials that contained 1 mL of DI water. The IPA samples were directly injected into the GC inlet operated at 250 $^{\circ}\text{C}$, where the GC oven was maintained at 35 $^{\circ}\text{C}$ for 7 min then increased at a rate of 10 $^{\circ}\text{C}/\text{min}$ to 60 $^{\circ}\text{C}$. Aqueous-phase concentrations of ferrous iron (Fe^{2+}) and total iron ($\text{Fe}^{2+} + \text{Fe}^{3+}$) were determined using the ferrozine method [83] after digesting samples with 11.1N hydrochloric acid (ACS grade, J.T. Baker, Phillipsburg, NJ).

2.3. Mathematical Model

Two fluid phases are considered in the conceptual model, a flowing aqueous phase and an immobile (residual) DNAPL phase. The mathematical model consists of two phase balance equations, coupled with mole balance equations for Fe^0 and organic constituents. A component mole-balance for Fe^0 is expressed as:

$$\frac{\partial}{\partial t} (\rho_b^* \omega_{\text{Fe}^0}^s) = -k_r a_{\text{Fe}^0}/_{\text{PCE}} C_{\text{PCE}}^w \rho_b^* \omega_{\text{Fe}^0}^s \quad (2.2)$$

where ρ_b^* (kg/m^3) is the bulk density of the dry sand, $\omega_{\text{Fe}^0}^s$ (mole Fe^0/kg of dry sand) is the molar-based Fe^0 concentration; k_r ($\text{m}^3/\text{s mol}$) denotes the first-order PCE reduction rate constant normalized by the number of moles of Fe^0 per unit volume of aqueous phase, $a_{\text{Fe}^0}/_{\text{PCE}}$ (mol/mol) is the stoichiometric ratio of the number of moles of Fe^0 consumed to reduce 1 mole of PCE to ethene, and C_{PCE}^w (mol/m^3) is the molar-based

aqueous concentration of PCE. This single step reaction kinetic equation for PCE dechlorination to ethene was implemented consistent with experimental measurement of ethene as the only detectable reaction product.

Several assumptions are implicit in Equation 2.2. First, the nZVI particles are assumed immobile following their delivery, consistent with experimental observations. In addition, the influence of pH on PCE dechlorination rate is neglected. This assumption is consistent with experimental observations of TCE dechlorination by nZVI particles [45] that indicated only a weak dependence of TCE reduction rate on solution pH (reaction order of 0.16), suggesting that hydrogen does not play a dominant role in determining dechlorination rates. Furthermore, the high buffering capacity of most soils implies that there will be little pH change with a typical injection of nZVI [45].

Anaerobic corrosion of iron with water was considered negligible relative to consumption of iron via the dechlorination reaction. *Liu et al.* [46] observed that non-target anaerobic iron corrosion reactions were mitigated at increased contaminant concentrations (>10 mg/L for TCE), reducing the amount of H₂ evolved. It is likely that this effect will be even more pronounced at the near equilibrium solubility limit concentrations of PCE within a PCE-DNAPL source-zone, as is the case for this study.

Reaction with nZVI is considered herein to take place at the aqueous-nanoparticle interfaces where dissolved-phase PCE is dechlorinated to ethene. Most investigators agree that reductive dechlorination in the presence of Fe⁰ in aqueous systems occurs by direct reduction at the iron surface [43, 46, 81]. Other mechanisms (not considered herein) have also been proposed, including reduction by hydrogen or reduction by ferrous iron, a corrosion by-product [81].

Adsorption of dissolved PCE, desorption of reaction products, as well as transfer of electrons from the Fe⁰ core of the particles to the surface are considered instantaneous, with the overall rate controlled by surface electron exchange [73]. *Doong and Lai* [43]

proposed that the reaction rate is first order with respect to the amount of available metal surface area. Here, changes in the specific surface area of nZVI particles with time are neglected, consistent with the experimental observations of *Liu and Lowry* [45]. They suggested that the particle surface area did not change significantly during oxidation in water, consistent with the conceptual model of a shrinking Fe^0 core with a growing magnetite shell at the $\text{Fe}^0/\text{Fe}_3\text{O}_4$ interface. Based upon this conceptualization, the particle surface area available for electron exchange is considered to be independent of time, and the surface concentration of electrons becomes a function of the Fe^0 content of the particle.

In equation 2.2, reduction reaction kinetics are assumed to be first-order with respect to both the Fe^0 content of nanoparticles and the aqueous-phase concentration of PCE. Most studies report that the degradation of chlorinated organic compounds by Fe^0 proceeds by pseudo-first-order kinetics with respect to contaminant concentration [43-45, 65, 73, 79, 80, 82]. The one exception to this was a batch study conducted under iron-limited conditions, (a molar Fe^0 : TCE ratio of ~ 2.9), where the product formation showed a clear lag phase (~ 10 h of slow reaction), followed by 2-3 days of steady rapid reaction, and finally a period of where the reaction slowed and eventually stopped [46].

Although *Liu and Lowry* [45] found that reduction of TCE was zero-order with respect to Fe^0 content over the life of the particles in their batch experiments, the Fe : TCE molar ratio employed was very large (>1000). In DNAPL source zones, however, where the achievable Fe:TCE molar ratio would likely be lower, due to the larger contaminant mass, Fe^0 availability could become a limiting factor (the initial Fe^0 : PCE molar ratio in the present study was ca. 11.4). Hence, based upon the above studies, the nZVI-driven dechlorination reaction is assumed first-order with respect to Fe^0 concentration and aqueous phase organic concentration, enhancing the overall reaction kinetics to the second order.

Transport of solute organic compounds in the aqueous phase is modeled by a traditional advection-dispersion-reaction (ADR) transport equation. The component mole-balance equations for dissolved phase PCE and ethene are given as:

$$\frac{\partial}{\partial t}(\phi S_w C_{PCE}^w) + \frac{\partial}{\partial x} \left[\phi S_w \left(C_{PCE}^w V_w - D_{wPCE}^h \frac{\partial C_{PCE}^w}{\partial x} \right) \right] = -k_r C_{PCE}^w \rho_b^* \omega_{Fe^0}^s + k_f a_0 (C_{PCE}^{sol} - C_{PCE}^w) \quad (2.3)$$

and

$$\frac{\partial}{\partial t}(\phi S_w C_{ethene}^w) + \frac{\partial}{\partial x} \left[\phi S_w \left(C_{ethene}^w V_w - D_{wethene}^h \frac{\partial C_{ethene}^w}{\partial x} \right) \right] = k_r C_{PCE}^w \rho_b^* \omega_{Fe^0}^s \quad (2.4)$$

where C_i^w (mol/m³) is the aqueous phase organic concentration, ϕ is the effective porosity of the sand taking into account the pore space occupied by the emplaced Fe⁰, S_w is the aqueous phase saturation, V_w (m/s) is the interstitial velocity of the aqueous phase, and D_{wi}^h (m²/s) denotes the hydrodynamic dispersion coefficient of dissolved organic in the aqueous phase. The second term on the right-hand-side of Equation 2.3 is a linear driving force expression, based on the assumption that NAPL dissolution in the aqueous phase is a rate-limited process controlled by diffusion across the stagnant water layer surrounding an entrapped NAPL droplet [84]. C_{PCE}^{sol} (mol/m³) is the molar aqueous solubility limit of pure phase PCE, k_f (m/s) and a_0 (m²/m³) are the mass transfer rate coefficient and the specific surface area of the NAPL blobs per unit volume of medium, respectively [84]. Here, $k_f a_0$ was estimated as a function of the system hydrodynamics, pore structure, and volumetric fraction of NAPL in the pore space from a dimensionless Sherwood number (Sh') correlation presented by Powers *et al.* [84]:

$$Sh' = \frac{\hat{k} a_{50}^2}{D_L^{PCE}} = 4.13 Re'^{0.598} \delta_g^{0.673} U_{ig}^{0.369} \left(\frac{\theta_n}{\theta_{n0}} \right)^{0.518+0.114\delta_g+U_{ig}} \quad (2.5)$$

in which \hat{k} (1/s) is a lumped mass-transfer coefficient ($\hat{k} = k_f a_0$), d_{50} (m) is the median grain diameter, D_L^{PCE} (m²s⁻¹) is the free liquid diffusivity of PCE in water, Re' is the dimensionless Reynolds number, δ_g (-) is the normalized median sand grain diameter ($\delta_g = \frac{d_{50}}{d_M}$), where d_M (m) is taken as the diameter of a “medium” sand grain ($d_M = 5 \times 10^{-4}m$), and U_{i_g} (-) is the uniformity index of the sand. Equation 5 has been validated through numerous experimental investigations in iron-free systems [85-88] and implemented in DNAPL source zone modeling (for a recent example see *Christ et al.*[89]).

A multiphase extension of Darcy’s Law [90] is used to express the aqueous phase mass balance:

$$\frac{\partial}{\partial t}(\phi \hat{\rho}_w S_w) = \frac{\partial}{\partial x} \left[\hat{\rho}_w \lambda_w \left(\frac{\partial P_w}{\partial x} - \hat{\rho}_w \bar{g} \right) \right] \quad (2.6)$$

where $\hat{\rho}_w$ (g/m³) is the mass density of the aqueous phase, S_w (-) is the saturation of the aqueous phase, \bar{g} (m/s²) is the gravitational acceleration vector, and λ_w (m³ s/g) is the mobility of the aqueous phase ($\lambda_w = k \frac{k_{rw}}{\mu_w}$), where k (m²) is the intrinsic permeability of the medium, k_{rw} (-) denotes the relative permeability of the aqueous phase, and μ_w (g/m s) is the aqueous phase dynamic viscosity. Here the influence of interphase mass-transfer on the aqueous phase mass balance is neglected.

For this pure phase PCE contamination, the mass balance for the NAPL phase is written in terms of moles as:

$$\frac{\partial}{\partial t}(\phi \rho_n S_n) = -k_f a_0 (C_{PCE}^{sol} - C_{PCE}^w) \quad (2.7)$$

where ρ_n (mol m⁻³) is the molar density of the NAPL phase.

Water phase saturation is obtained by assuming that pore spaces are fully saturated with the two liquid phases ($S_w + S_n = 1$). Changes in NAPL phase density due

to back-partitioning of reaction products (i.e. ethene) were considered to be insignificant due to the relatively low by-product concentrations observed in the column experiments. Additionally, the mass of organic constituents sorbed by the solid phase was assumed negligible relative to the mass existing as PCE-DNAPL and dissolved in the aqueous phase, and was therefore neglected in the overall mass balance calculations.

The phase and organic constituent mass balance equations were discretized using a Crank-Nicolson finite-differencing scheme. A Lagrangian random-walk particle-tracking (RWPT) method was implemented for discretizing the nZVI mass balance equation. Simulations start with solution of the aqueous phase flow equation (i.e. Equation 6), and then proceed with solution of the nZVI mass balance equation (i.e. Equation 2). The reactive transport equations for organic constituents (i.e. Equations. 3-4) are solved sequentially. Phase saturations are then computed by solving the NAPL phase mass balance equation (i.e. Equation 7). The numerical simulator was verified through comparisons with analytical solutions for transport of a nonreactive pulse of a tracer solute and a pulse of a reactive solute (See Appendix II for more detail). Model mass balance errors, computed on a mole basis for total C_2 (i.e. the sum of the number of moles of PCE and that of ethene) in the system, were in the range $3.5 \pm 2.5 \times 10^{-2}\%$ for all simulations reported herein.

2.4. Results and Discussion

2.4.1. Experimental Results

The nZVI delivery ($60 \text{ g}_{\text{Fe}}/\text{L}$ aqueous suspension) phase of the column experiment is presented in Figure 1, which was carried out at a constant flow rate of 2 mL/min and was associated with minimal displacement of PCE-DNAPL from the column. Fingering was not observed and the overall process resulted in the establishment of a uniform distribution of both nZVI and residual PCE DNAPL throughout the column.

Following nZVI emplacement, 267 PVs of a 3.5mM CaCl₂ aqueous solution were flushed through the column. No displacement of RNIP particles or PCE-DNAPL was observed in column effluent samples during this water flushing phase. Figure 2 presents effluent concentrations of organic constituents measured during the first 170 PVs aqueous solution flushing which were used for model validation since only one additional data point was collected at 267 PVs. Despite the presence of nZVI, no substantial reductions in PCE effluent concentrations was observed during the experiment, i.e., a near equilibrium solubility concentration of PCE (average effluent concentration of 240.2 mg/L) was measured. Significant ethene evolution (average concentration of 18.2 mg/L), however, was also observed, indicating that nZVI was reacting with PCE. Other relevant daughter products, including TCE, cis-DCE, and vinyl chloride were not detected in any of the effluent samples. Additional column experiments conducted using the same or similar nZVI material yielded similar results, including effluent PCE concentrations at or near the aqueous solubility limit and production of ethene at concentrations ranging from 10 to 30 mg/L (data not shown). Only intermittent emergence of gas bubbles was observed during the experiments, suggesting that hydrogen gas production via the anaerobic corrosion reaction of nZVI with water was minimal. This observation at high PCE concentration levels is consistent with the findings of Liu and Lowry [45], who reported a substantial decrease in H₂ gas evolution with increasing organic contaminant concentrations (above 10 mg/L for TCE). At the conclusion of the column experiment, approximately 20% of in the initial PCE-DNAPL mass remained in the column.

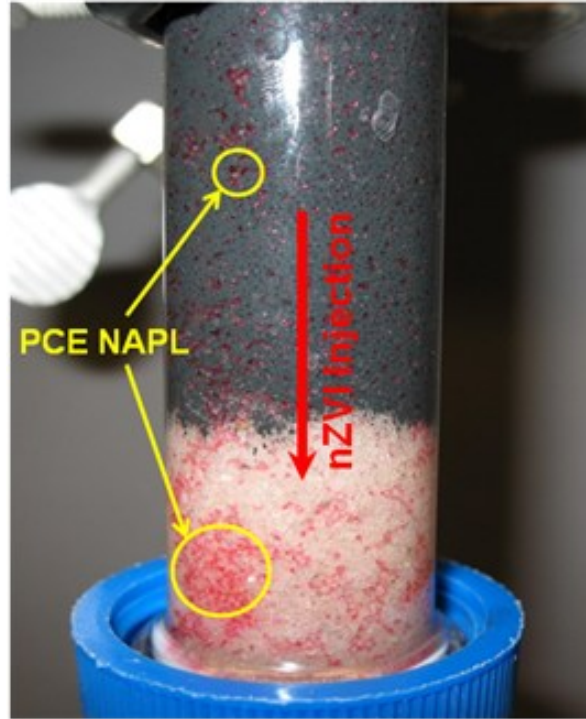


Figure 2-1. Placement of the RNIP particles in the PCE-DNAPL containing sand column [91].

2.4.2 Mathematical Modeling Results

The numerical model, developed from the mathematical model described in Section 2.3 of this dissertation, was used to simulate the measured effluent concentrations. Values of the model input parameters are provided in Table 2.1. Only one modeling parameter was fit to reproduce experimental results, an effective PCE reduction reaction rate constant (k_r) of 1.42 1/hr, which provided a close match to the measured effluent data (Figure 2.2). A least sum of squared residuals-based (LSSR) optimization method was used to estimate this value. When normalized by the mass of nZVI per unit aqueous phase volume, the value of this rate constant is 3.9×10^{-3} L/hr g (equivalent to 1.70×10^{-4} L hr⁻¹ m² assuming a specific surface area of 23 m²/g for RNIP particles as reported by *Liu et al.*[46]). This normalized rate is consistent with the magnitude of the Fe⁰ mass normalized rate constant (2.1×10^{-3} L/hr g) reported by *Shin et al.* [79] for the

dechlorination of dissolved phase TCE by micron-sized uncoated iron particles (<0.15mm) with a specific surface area of (0.5 m²/g). However, these rates are approximately one order-of-magnitude smaller than the continuously mixed batch reactor (CMBR)-based dechlorination rate constant of 7.1×10^{-2} L/hr g reported by *Liu et al.* [46] for TCE with RNIP, and one order-of-magnitude larger than the CMBR-based pseudo first-order rate constant of (4.8×10^{-4} L hr⁻¹ g⁻¹) measured by *Doong and Lai* [92] for dechlorination of PCE with micron-sized iron powder (measured specific surface area of 0.14 m²/g).

Table 2-1. Summary of experimental properties and model input parameters [91].

Property	Units		Source/Reference
Column porosity	-	0.354	Gravimetric measurement
Effective column length	cm	16.1	Gravimetric measurement
Column pore volume	mL	28.0	Gravimetric measurement
Darcy velocity	m/day	0.73	Gravimetric measurement
Peclet number	-	50	Estimated from bromide tracer test
Median blob diameter	mm	0.5	<i>Powers et al. [84]</i>
Median sand grain diameter	mm	0.71	<i>Cho and Annable [93]</i>
Uniformity Index	-	1.21	<i>Cho and Annable [93]</i>
Sand grain density	g/cm ³	2.65	
Fe particle density	g/cm ³	7.784	<i>Kaye and Laby [94]</i>
Viscosity of Water	g/m·s	1.0	
Viscosity of PCE	g/m·s	0.89	<i>Qin et al. [95]</i>
Aqueous diffusivity of PCE	cm ² /s	1.02×10^{-5}	<i>Chiao et al. [96]</i>
Aqueous diffusivity of ethene	cm ² /s	8.8×10^{-6}	
PCE-DNAPL saturation	%	5.5	Estimated by volume and weight
PCE equilibrium solubility	mg/L	250	<i>Pennell et al. [97]</i>
Mass of iron in the column	g	40	
Initial Fe ⁰ -content of particles	%	24	Measured by digestion in hydrochloric acid from the amount of hydrogen production
Fe ⁰ : PCE Stoichiometric ratio	-	4.0	
Initial Fe ⁰ : PCE molar ratio	-	11.4	Measured experimentally

These data indicate that the effective PCE dechlorination rate obtained from the column study falls within the range of values observed in batch studies of Fe⁰ particle reactivity with dissolved-phase chlorinated ethenes. However, inherent differences in the

mixing conditions of columns and batch reactors, and in the reactivity of the PCE and TCE, preclude direct comparisons.

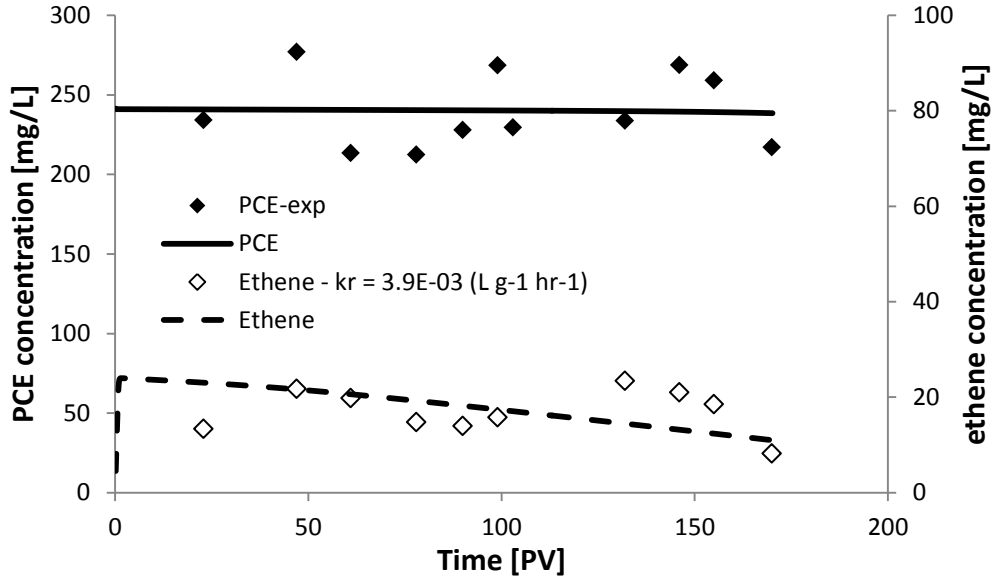


Figure 2-2. Experimental and model breakthrough curves of dissolved-phase PCE and ethane [91].

The fitted model predictions of PCE-DNAPL saturation distribution, Fe^0 content, and dissolved species (PCE and ethene) at various times are presented in Figure 2.3. Model mass balance results indicate that, after flushing with 170 PV of aqueous solution, 7% of the initial Fe^0 mass emplaced in the column was consumed in the dechlorination of approximately 20% of the initial mass of PCE-DNAPL to ethene (measured in effluent samples), while experimental measurements showed that 40% of the initial mass of PCE-DNAPL was dissolved from the column at the aqueous solubility limit (Figure 2). Approximately, 40% of the initial mass of PCE-DNAPL remained in the column at the conclusion of the simulation period (i.e. 170 PV). Note that, if only dissolution had occurred (i.e. no reaction), according to model prediction 58% of the initial mass of PCE-DNAPL would have remained in the column after 170 PV injection of aqueous solution. At 170 PV, the model predicts the complete dissolution/transformation of PCE-DNAPL

near the influent end of the column, with saturations increasing to a residual of 4.4% near the effluent (Figure 2.3(a)). The model also predicts that less Fe^0 consumption occurs closer to the column inlet (Figure 2.3(b)), consistent with near zero dissolved-phase PCE concentrations as the experiment proceeds (Figure 2.3(c)).

The model also predicts that effluent ethene concentrations should gradually decrease over time. This decrease in concentration is attributed to two factors: (1) decrease in Fe^0 content of RNIP particles which render them less reactive over time, and (2) the gradual decrease in dissolved PCE residence time in the column as the PCE-NAPL is gradually dissolved from the influent end of the column. The latter effect is more significant, however, as only 7% of the Fe^0 mass was estimated to be consumed during the course of experiment.

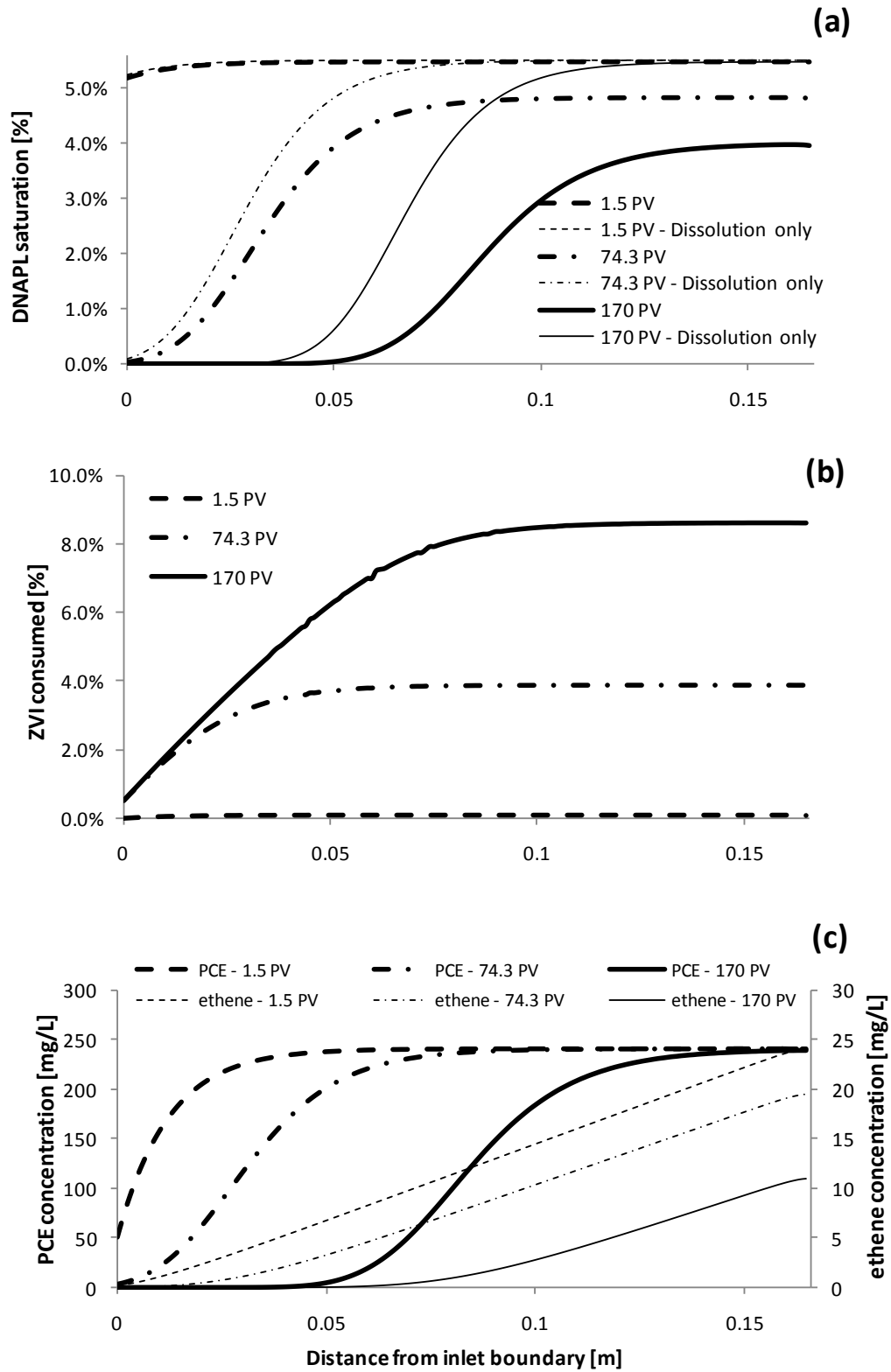


Figure 2-3. Spatial distribution profiles of (a) DNAPL saturation, (b) Fe^0 content of soil, and (c) dissolved PCE and ethene concentrations at different simulation times [91].

2.4.3. Sensitivity Analysis

A model sensitivity analysis was undertaken to gain additional insight into the potential influence of flow and emplacement conditions on DNAPL source zone treatment efficiency. For all simulations, the total simulation time was adjusted to allow for complete removal of contaminant mass from the domain. Four input parameters were varied in this analysis: (1) the emplaced nZVI concentration, (2) the aqueous flow rate, (3) the DNAPL source zone length, and (4) the emplaced nZVI zone length. Several model outputs were examined, including: (1) the fraction of initial DNAPL mass remaining, (2) a dimensionless PCE Transformation Efficiency Index (TEI), and (3) effluent concentrations of dissolved phase PCE and ethene concentrations. Here the dimensionless TEI is defined as the ratio of the total moles of reaction products (i.e. ethene) recovered in the effluent to the initial moles of emplaced PCE-DNAPL. This index represents the percentage of the initial contaminant mass present in the source zone that has been transformed to ethene.

2.4.3.1. Sensitivity to Decreased Soil Iron Concentration

The emplaced nZVI concentration in the experimental system was approximately 283 g_{Fe}/kg soil. This iron concentration is higher than reported values from documented pilot-scale field-injection studies. *Henn and Waddill* [75] performed a pilot test using Pd-catalyzed and polymer-coated nanoscale iron particles, in which 4.5 PV of an aqueous nanoparticle suspension (4.5 g_{Fe}/L) was injected into the treatment zone. Assuming an approximate soil bulk density of (1500 kg/m³), this yields an average nZVI content of 10-15 g_{Fe}/kg soil over the injection field. This estimated value is more than one order of magnitude lower than that in our column experiment. *Zhang* [98] reviewed the results from a field demonstration of nZVI injection for *in situ* groundwater treatment, where 11.2 kg nZVI was injected into a shallow surficial aquifer. The radius of influence was

reported as 6-10m, with a bed-rock depth 6.6m below the ground surface. Assuming a bulk density of 1500 kg/m³, the average Fe⁰ content for this demonstration was on the order of 1×10⁻² g_{Fe}/kg soil, more than five orders of magnitude lower than the experimental column system presented herein.

To explore the sensitivity of model predictions to the amount of iron emplaced, the emplaced iron concentration ($\omega_{\text{Fe, exp}}=283$ g/kg dry soil) was varied over a one order of magnitude range (from 283 to 28.3 g_{Fe}/kg dry soil), with all other original column parameter values held constant. It was assumed that the normalized PCE dechlorination constant is the same for all particles and remains constant regardless of the mass loading of the particles in the system. The accuracy of these assumptions depends on a number of factors including (1) the influence of particle concentration on the effective reaction surface area available on each particle, and (2) the effect of particle loading on system hydrodynamics and flow regime. Results of these simulations are presented in Figure 4. Simulation results reveal that a decrease in emplaced iron concentration was associated with an increase in the mass of PCE-DNAPL remaining in the source zone at the conclusion of the water flushing period and a decrease in PCE transformation efficiency. For example, a one order of magnitude decrease in iron concentration (from 283 to 28.3 g_{Fe}/kg dry soil) resulted in an increase in PCE-DNAPL mass remaining (from 40% to 56% at 170 PV), and resulted in an order-of-magnitude decline in the PCE TEI, (from 25.2% to 3.0%) (Figure 2.4(a)). A decrease in emplaced iron concentration was also associated with a slight increase in effluent PCE concentration and a substantial decrease in effluent ethene concentrations, respectively. For a one order of magnitude change in emplaced iron concentration, the effluent PCE concentration increased (~3%) from 241 mg/L to >249 mg/L (Figure 2.4(b)), while the simulated maximum ethene effluent concentration decreased by one order-of-magnitude. Unlike the PCE TEI and effluent concentrations of ethene, PCE-DNAPL dissolution scales only slightly with the amount

of emplaced iron due to the significant contribution of the dissolution process in the removal of mass from the DNAPL phase.

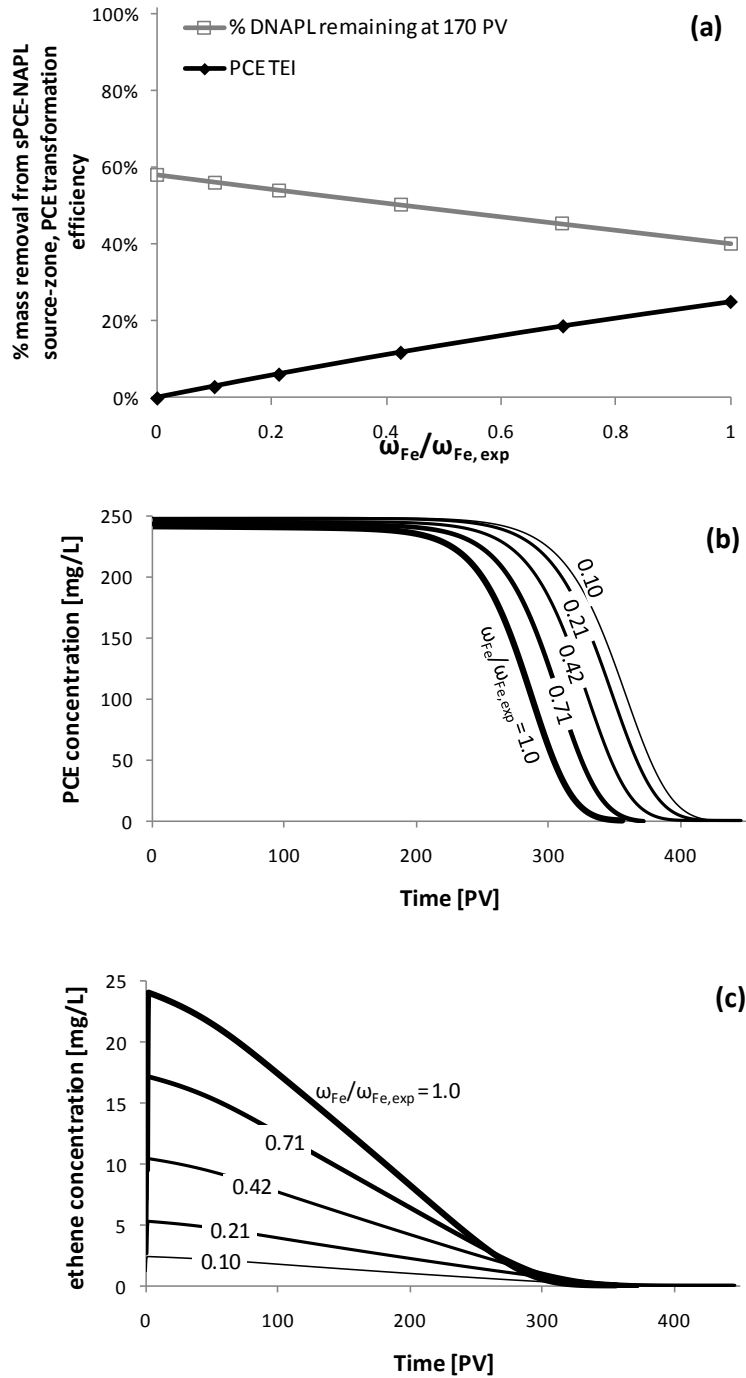


Figure 2-4. Influence of initial emplaced nZVI concentration on (a) DNAPL mass remaining in the source zone and PCE transformation efficiency, and effluent concentrations of (b) PCE, and (c) ethane [91].

2.4.3.2. Sensitivity to the Reduced Flow Rate

The applied experimental volumetric flow rate resulted in a pore water velocity of 2.1 m/day, which is at the upper range of typical groundwater velocities (0.15-1.4 m/day in shallow sandy aquifers [99]). Thus, the influence of pore-water velocity on treatment efficiency was explored over a two order of magnitude range (from 2.1 m/day (0.25 mL/min) to 0.02 m/day (2.5×10^{-3} mL/min)), while holding all other experimental parameters constant. It was assumed that the normalized PCE dechlorination rate constant does not vary with the aqueous phase flow velocity. Results of these simulations are presented in Figure 2.5. For an identical volume of water flushing, decreasing the flow rate to 2.5×10^{-2} mL/min resulted in an increase in the PCE TEI from 25% to 81%, and an increase in DNAPL removal (from 60% to 99.8% of the initially emplaced mass of DNAPL at 170 PV) (Figure 2.5(a)). Further decreasing the flow rate to 2.5×10^{-3} mL/min increased the PCE TEI to 99%, thereby yielding almost complete transformation of the initial PCE-DNAPL mass to ethene after flushing with 170 PVs of water. Approximately, one-third of the initial mass of Fe^0 was consumed under these conditions.

Although the contaminant transformation efficiency increases at lower flow rates, the time-length of DNAPL persistence also increases. The time to complete DNAPL removal increased by an approximate factor of 3 when the flow rate decreased by one order of magnitude from 2.5×10^{-2} mL/min to 2.5×10^{-3} mL/min; as shown on Figure 2.5(b), ca. 100 PV is required for complete clean-up of the column in the lower flow case, whereas at a 10-times faster flow rate complete removal of mass from the column is reached at ca. 350 PV. In addition, the sensitivity analysis indicates that regardless of the flow rate, the effluent concentrations of dissolved PCE remain substantial (i.e. >100 mg/L) until significant removal of PCE-DNAPL from the source zone (Figure 2.5(c)). Also plotted in Figure 2.5(a) (dotted curves), are results for simulations at a lower nZVI content ($\omega_{\text{Fe}}=28.3$ g/kg) more representative of field test conditions. The model results

demonstrate a greater sensitivity to reduced flow rate with respect to the PCE TEI. For example, at this lower emplaced nZVI concentration, the PCE TEI increases (one order of magnitude) from 3% to 16% and then to 27% and at the same time the mass of PCE-DNAPL remaining (at 170 PV) in the source zone decreases from 56% to 45% and then to 31% as flow rate decreases from 0.25 mL/min to 2.5×10^{-2} mL/min and then to 2.5×10^{-3} mL/min.

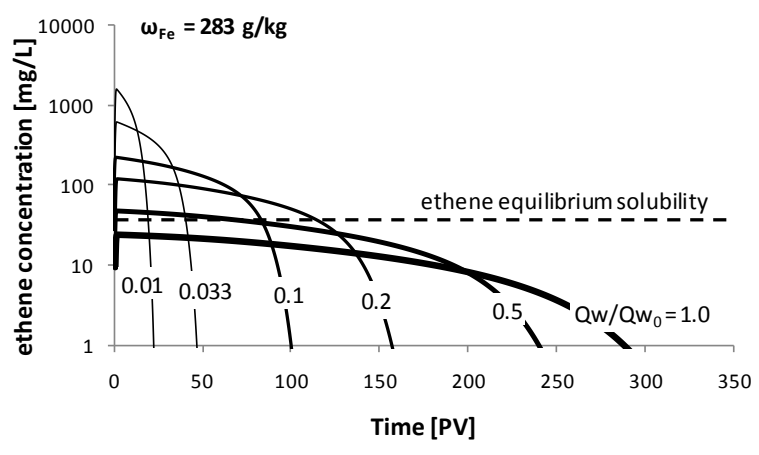
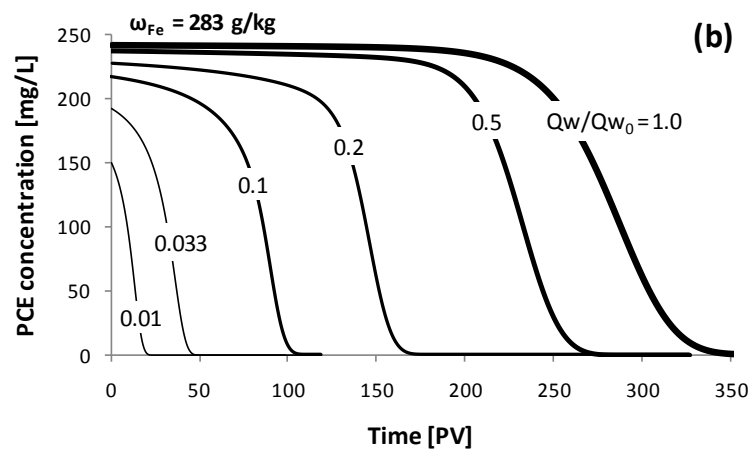
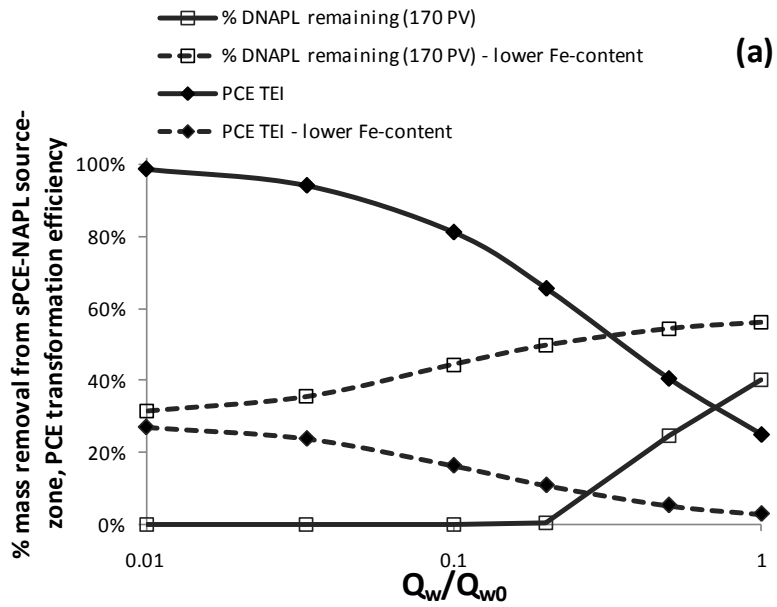


Figure 2-5. Influence of flow rate on (a) DNAPL mass remaining in the source zone and PCE transformation efficiency index, and effluent concentrations of (b) PCE, and (c) ethene. Here lower Fe content=28.3 g/kg [91].

The sensitivity of both source zone PCE-DNAPL mass removal and PCE transformation efficiency to flow velocity can be attributed to the increase in retention time of dissolved contaminant in the column. An increase in the residence time is associated with an increase in the reaction (contact) time and, consequently, with the production of reaction products (i.e., ethene). For the lower nZVI content scenario, the reduction in flow rate enhances the PCE TEI by one order of magnitude from 3% to 27%. However, complete contaminant reduction is not achieved at the lower emplaced iron concentration because of the passivation of particles due to the Fe^0 consumption (95% loss of the initial Fe^0 content) during the 170 PV injection period.

Care must be taken in interpreting the ethene effluent concentration predictions (Figure 2.5(c)). For example, note that, when the flow rate decreased by two orders-of-magnitude, the predicted ethene concentration is 40 times greater than the aqueous solubility of ethene under atmospheric pressure and ambient room temperature (22 °C). Thus, the simulations suggest that, under these flow conditions, an ethene gas phase would evolve in the pore space, resulting in significant gas accumulation in the system. This produced ethene gas would be sufficient to occupy a volume approximately 12 times greater than the column pore volume. Thus, if gas were unable to escape the column, gas accumulation would likely create substantial pore blockage, thereby causing a reduction in the flow through the reactive zone, potentially enhancing the relative contribution of dispersive mixing down gradient from the entrapped gas zone [100] and reducing the efficacy of the nZVI technology for field scale applications.

2.4.3.3. Sensitivity to Reduced DNAPL Source Zone Size

In this phase of the sensitivity analysis, the length of the residual PCE-DNAPL contaminated zone was incrementally reduced to assess the potential for emplaced nZVI to treat dissolved phase PCE emanating from the source zone. This sensitivity analysis

was performed at two uniform nZVI content levels: 283 g_{Fe}/Kg soil (experimental iron content) and 28.3 g_{Fe}/Kg soil (lower iron content), with nZVI emplaced throughout the column bed length (Figure 2.6). Inspection of Figure 2.6(a) reveals that, when the length of PCE-DNAPL was reduced to 4.15 cm ($L/L_0=0.25$), complete removal of mass from the DNAPL source zone was achieved prior to 170 PV, regardless of the emplaced iron concentration. This mass removal was attributed to both reaction (44% of the initial PCE mass) and dissolution (41% of the initial PCE mass). Furthermore, the effluent concentration of PCE decreased from near the PCE solubility limit to less than 50 mg/L (Figure 2.6(b)), and at the same time, the effluent concentration of ethene decreased from 23 mg/L to 7mg/L (Figure 2.6(c)). Although complete mass removal from the source zone was accomplished by reducing the size of the DNAPL source, more than 50% of the total mass in the effluent was present as dissolved-PCE, regardless of the relative size of the source zone. This outcome was exacerbated at the lower emplaced iron content, where $95.5\pm 1.5\%$ of the total eluted mass was in the form of dissolved-phase PCE. When the PCE-DNAPL source zone was further reduced to the first 0.5cm of the column ($L/L_0=0.03$), the PCE TEI increased from 20% to 49%. At the lower emplaced iron concentration, the same reduction in source zone length increased the PCE TEI from 3% to 6% (Figure 2.6(a)). The average residence time of dissolved-phase PCE in a column containing a uniform saturation of PCE-DNAPL is equal to one-half of the average residence time of the water. As the DNAPL source zone length in the column becomes smaller, the average residence time of dissolved-phase PCE approaches that of water for the extreme case where all DNAPL mass is concentrated on a point source at the column inlet. Thus, the observed increase in the PCE TEI was attributed to the increase in the residence time of dissolved-phase PCE within the nZVI zone.

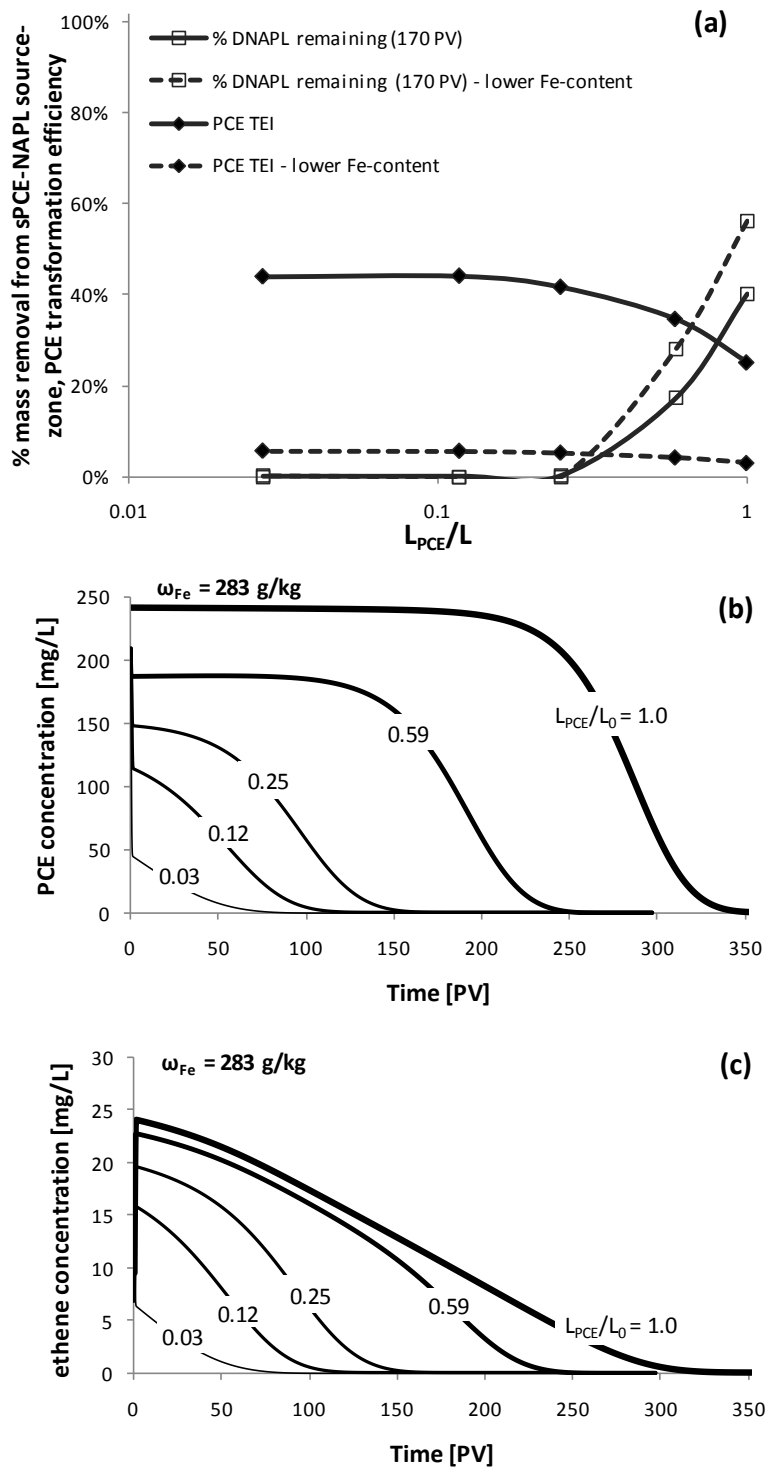


Figure 2-6. Influence of DNAPL source zone size on (a) DNAPL mass remaining in the source zone and PCE transformation efficiency index, and effluent concentrations of (b) PCE, and (c) ethene. Here lower Fe content=28.3 g/kg [91].

2.4.3.4. Sensitivity to the Length and Spatial Distribution of the nZVI Zone

A final set of simulations was conducted to explore the influence of the length of the downstream nZVI zone on treatment efficiency based on the assumption that PCE dechlorination rate does not strongly depend on the PCE concentration (i.e., constant k_r). This assumption permitted implementation of the same dechlorination rate coefficient throughout the length of the reactive zone within and outside of the DNAPL source zone. However, it should be noted that several experimental investigations suggest a dechlorination rate dependency on the initial concentration of chlorinated ethane [45, 46]. Maintaining the original column conditions (i.e., nZVI content, length, PCE-DNAPL saturation, flow rate, and simulation time), a second column containing nZVI at the same concentration level was placed at the effluent end of the initial column (i.e., extending the length of the nZVI reactive zone). Decreasing the emplaced iron concentration from 283 $\text{g}_{\text{Fe}}/\text{kg}$ to 28.3 $\text{g}_{\text{Fe}}/\text{kg}$ resulted in a decline in the total PCE-DNAPL mass removal from the column from 60% to 44%. The fraction of mass removed from the source zone increases only slightly with the addition of a second reactive zone (an increase from 60% to 61% with a 9-fold increase in L_{ZVI} (see Figure 2.7(a)), indicating that placement a reactive zone down-gradient from a DNAPL source zone does not result in the enhanced dissolution of DNAPL, but does reduce the down-gradient aqueous PCE concentration eluting from the source zone as shown in Figure 2.7(b). As anticipated, this resulted in a substantial enhancement of dissolved PCE transformation (see Figure 2.7). Consider the case for which the column extension was 83.4cm. Under these conditions, for the emplaced iron concentration of 283 $\text{g}_{\text{Fe}}/\text{kg}$, 96% of the total organic mass in the effluent was present in the form of ethene (Figure 2.7(a)). To achieve near complete conversion of PCE-DNAPL to ethene (>99%), the sensitivity analysis indicates that the length of the second column must be increased to 133.4cm. For this higher emplaced iron concentration, a 9-fold increase of the reactive zone (to 150cm from 16.1 cm), which was

associated with a 9-fold increase in the implemented mass of nZVI, decreased the breakthrough PCE concentrations by two orders of magnitude (Figure 2.7(b)), while the predicted effluent concentrations of ethene tripled to exceed the aqueous solubility of ethene (Figure 2.7(c)). If contained within the column, the excess ethene would be enough to occupy nearly one-third of the column pore volume under ambient pressure and temperature conditions.

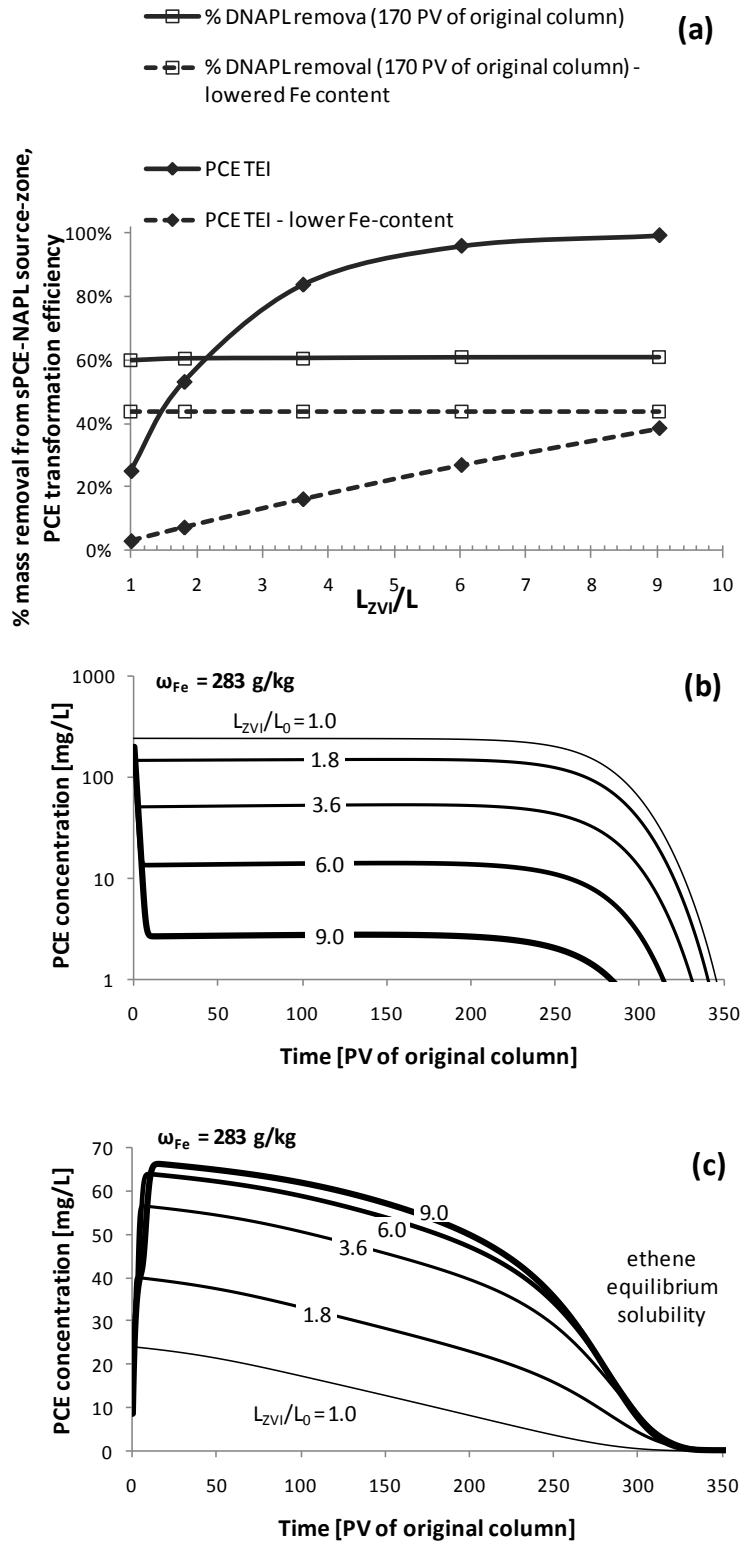


Figure 2-7. Influence of downstream nZVI zone on (a) DNAPL mass remaining in the source zone and PCE transformation efficiency index, and effluent concentrations of (b) PCE, and (c) ethene. Here lower Fe content=28.3 g/kg [91].

These simulations reveal that a significant enhancement in the PCE conversion efficiency can be achieved only by changing the spatial distribution of the nZVI particles. This can be seen by comparing two case scenarios. The first case is the original column scenario (initial 0.172 mole of Fe⁰), and the second case is the increased nZVI zone length ($L_{ZVI} = 150\text{cm}$) at the lower emplaced nZVI content (initial 0.155 mole of Fe⁰). The PCE TEI was found to increase significantly from 25% to 38% (i.e. >50% enhancement), when the mass of nZVI was distributed down-gradient of the source (case #2) instead of being densely packed in the DNAPL source zone (case #1). It should be noted that the amount of nZVI in the latter case was even less than that in the original case and still yielded a higher level of transformation efficiency.

2.4.4. Damköhler Number Analysis

A *Damköhler* number analysis was performed with the objective of identifying a metric that could aid in predicting the PCE TEI from the characteristics of a system of interest. Such a metric would be beneficial in the design of nZVI-based remedial schemes for treatment of DNAPL source zones.

Damköhler numbers are dimensionless numbers used in the chemical engineering literature to relate the timescales of chemical reaction to those of transport in a system [101], and have been used to describe mass transfer in multiphase systems [87, 102]. Here, the initial *Damköhler* type (I) (Da_I) was employed to characterize the relative importance of reaction kinetics to advection for PCE transport through the multiphase system containing entrapped PCE-DNAPL ganglia. Da_I was computed using the following expression:

$$Da_I = \frac{\hat{k} \cdot l_R}{v_w} \quad (2.8)$$

where \hat{k} [1/s] is an effective reaction rate coefficient, l_R [m] is the average contact length of the contaminant in the reactive zone, and v_w [m/s] is the pore water velocity. By substituting the effective reaction coefficient with the normalized PCE dechlorination rate, k_r [L/hr g], the following expression is derived:

$$Da_I = \frac{\left(k_r \cdot \frac{\rho_b \omega_{Fe^s}^s f_{Fe^0}^{init}}{\phi S_w} \right) \cdot (L_{ZVI} - 0.5L_{PCE})}{\frac{q_w}{\phi S_w}} \quad (2.9)$$

where the second term in the numerator is the initial average contact length of dissolved PCE in the reactive zone. Simplifying the terms in Eq.9 yields the following expression:

$$Da_I = k_r \rho_b f_{Fe^0}^{init} \omega_{Fe^s}^s \frac{L_{ZVI} - 0.5L_{PCE}}{q_w} \quad (2.10)$$

Results of the *Damköhler* number analysis are presented in Figure 8, which reveals that $\text{Log } Da_I$ exhibits the same relation with the PCE TEI, independent of nZVI zone length (Figure 2.8(a)). However, it is also apparent that the Da_I scaling does not work under reduced flow conditions. However, as shown in Figure 2.8(b), use of a modified *Damköhler* number $\hat{D}a_I$ resulted in a similar $\text{Log } \hat{D}a_I$ -PCE TEI relationship for all of the scenarios considered. Here, $\hat{D}a_I$ is defined as:

$$\hat{D}a_I = Da_I \cdot \left(\frac{L_{ZVI}}{L_{obs}} \right)^{0.5} \quad (2.11)$$

where L_{obs} [m] is the distance between the upstream end of the reactive zone and the location of the observation point for PCE TEI measurement, here the length of the

longest column considered in the sensitivity study (i.e. $L_{obs}=1.5m$). A log-linear relationship between \hat{Da}_1 and PCE TEI was observed within a wide PCE TEI range of values (10% - 95%) with an r^2 value of 0.988 (Figure 2.8(c)).

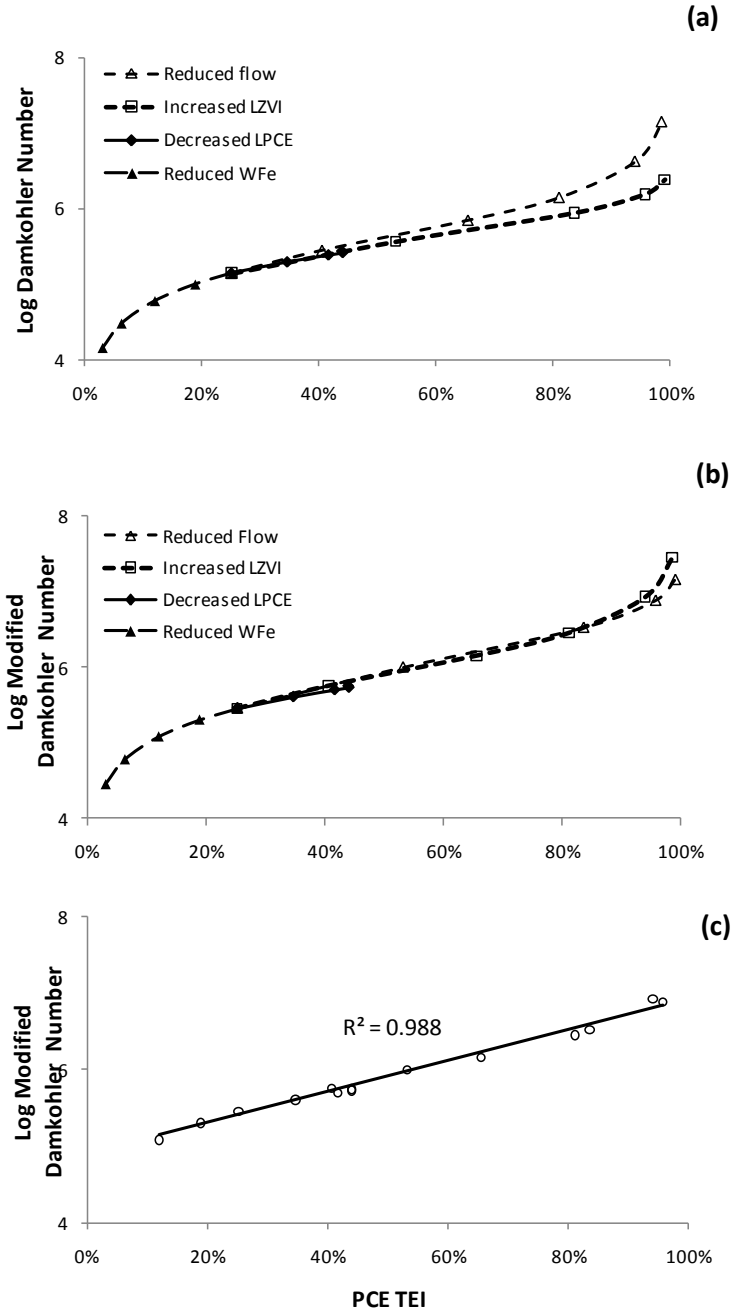


Figure 2-8. Logarithmic diagrams of (a) Da_1 -PCE TEI, (b) modified Da_1 -PCE TEI relations, and (c) range of linearity of Log modified Da_1 -PCE TEI relationship [91].

2.5. Summary and Conclusions

Experimental results demonstrate that the emplacement of nZVI into the PCE-DNAPL source zone resulted in partial conversion of PCE to ethene (20%). Even though nZVI was successfully delivered to the source zone at a high concentration (60 g/L), observed effluent concentrations of PCE persisted at or near the solubility limit throughout the duration of the experiment (267 pore volumes). The developed numerical simulator accurately captured these experimental findings. Subsequent sensitivity analyses revealed that treatment effectiveness was strongly dependent upon the mass and spatial distribution of nZVI, as well as the initial PCE mass and the mean residence time of dissolved contaminant in the reactive zone. For example, when the flow rate was reduced by two orders-of-magnitude, the mean residence time of dissolved-phase PCE in the column increased sufficiently to allow for almost complete conversion of PCE (98%) to ethene. However, the time required for PCE-DNAPL removal significantly increased with decreasing the flow rate, and effluent concentrations of PCE were predicted to be substantial (> 100 mg/L) even at low flow rates. When the size (length) of the DNAPL source within the treatment zone was decreased by 50% or more, both the concentration and duration of PCE in the effluent decreased substantially.

Alternatively, placement of additional nZVI zone down-gradient from the DNAPL source zone not only enhanced the transformation efficiency of PCE, but also reduced the effluent concentrations of PCE. Based on the normalized (by the mass of Fe^0 per unit aqueous phase volume) PCE dechlorination rate constant of 3.9×10^{-3} L/hr g obtained from the column results, placement of a 133.4cm long (thick) nZVI zone downstream of the PCE-DNAPL source zone would increase the residence time of the dissolved PCE enough to result in complete conversion of PCE to ethene under the flow and porous medium conditions of the column experiment. The spatial distribution of

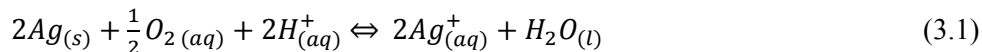
nZVI particles was found to significantly influence PCE transformation efficiency, to the extent that when the same mass of nZVI was located immediately down-gradient of the DNAPL source zone, rather than being emplaced within the source zone, the PCE TEI increased by more than 50%. This finding suggests that for field applications, injection of nZVI particles in the down-gradient region of a defined DNAPL source zone may improve the overall contaminant transformation efficiency. Taken in concert, the experimental and mathematical modeling results presented herein demonstrate that careful attention to remedial design parameters, including flow rate/residence time, source strength, reactivity, and location and amount of nZVI delivered, will be necessary to achieve meaningful treatment of DNAPL source zones with nZVI.

Chapter 3 MODELING OF THE TRANSPORT AND DISSOLUTION OF SILVER NANOPARTICLES IN POROUS MEDIA

3.1. Introduction

Understanding the transport behavior and reactivity of nanoparticles (NPs) in porous media is essential for accurate assessment of their fate and potential influence on subsurface ecosystems and water supplies. Concerns over the potential adverse impacts of nAg on human health and the environment have arisen based upon their widespread use in a variety of household products [3]. Although the risks posed by nAg to mammalian cells are currently unclear [36, 103], existing evidence suggests potential harm to organisms at lower ranks of the food chain. *George et al.* [103] reported multiple morphological and physiological effects on the development and hatching of nAg-treated zebra fish embryos. An understanding of nAg environmental fate is complicated by the coexistence of the particulate (nAg) and ionic (Ag^+) forms, which likely exhibit different biological potency [48] and physiochemical and transport characteristics, and may exhibit independent or synergistic toxicity pathways[47]. nAg may undergo significant transformation by dissolution, which has been shown to be a cooperative oxidation process requiring both dissolved oxygen (DO) and protons[104]. nAg Oxidation produces unstable peroxide intermediates, proceeding to complete reactive dissolution[47]. The biocidal activity of Ag^+ is substantially greater than that of nAg[105], and thus, the extent and rate of dissolution will be of primary importance in assessing the

environmental impacts of nAg releases. The following reaction stoichiometry has been proposed for the oxygen-mediated release of Ag^+ from nAg in the absence of other oxidants [47, 48]:



Batch system studies of the kinetics of ion release from nAg have explored the influence of various factors, including solution pH [35, 47], temperature, NOM [47], electrolyte concentration and ionic strength [36], and particle coating and particle size [48, 106]. A comprehensive assessment of nAg behavior in the subsurface, however, requires an understanding of nAg particle physical interactions with the porous matrix (i.e. transport and retention), coupled with knowledge of the dissolution process. Similar to other colloidal particles, the transport and retention of nAg is controlled not only by physicochemical properties but also by environmental conditions, such as flow velocity, soil grain size, and solution chemistry [10]. In addition, temporal changes in NP size and shape may influence nAg transport and retention [1] and dissolution behavior. In contrast to nAg dissolution kinetics, there has been limited research on the transport of nAg [107, 108]. This critical knowledge gap was identified in a recent review of environmental fate of nanomaterials [12]. Based upon a conceptual understanding of the processes controlling the environmental fate of nAg, mathematical models can be developed to represent the coupling of these processes, serving as effective tools for risk assessment and design of treatment or remediation strategies. Previous modeling attempts, however, have focused on either transport [108] or dissolution [47, 48] of nAg in terrestrial systems. To the best of our knowledge, no prior study has explored the coupling of the chemical reactions and physical processes that simultaneously control the fate and transport of nAg in porous media. As stressed by *Zhang et al.* [48], there is a clear need

for better predictive models that link the ion release behavior of nAg to its environmental fate and transport.

To address these limitations, HELP-1D simulator was modified to capture the coupled particle dissolution, transport, and retention processes that govern the fate of nAg in the subsurface. While prior NP transport modeling studies have assumed particle uniformity and stability during interactions with surfaces and with other reactive compounds [10, 15], the hybrid modeling approach, based on the numerical framework presented in *Taghavy et al.* [91], can account for temporal and spatial changes in the physicochemical properties of nanoparticles subject to dissolution. HELP-1D was validated through comparisons with the experimental results of a nAg transport and dissolution column study conducted under conditions representative of natural aquifer systems. Batch experiments were conducted to assess the short term and long term dissolution kinetics of nAg on a time scale relevant to the residence time of columns used in subsequent transport study. A model sensitivity study was conducted to gain additional insight into the potential influence of flow velocity and particle size on the transport and dissolution of nAg particles.

3.2. Materials and Methods

The experimental information disclosed in this Subsection is not a part of this dissertation. The results of the described experiments (conducted by Prof. Pennell's research group, Ms. **Mittelman A.** and Dr. **Wang Y.**) were used in subsequent numerical simulations.

Citrate-stabilized nAg particles were prepared based on the method of *Liu and Hurt* [47] using sodium borohydride as the reducing agent and silver nitrate as the precursor. This method produced a 16 mg/L solution of nAg with a mean diameter of 12

± 2 nm and non-detectable levels of silver ion (Ag^+). Silver concentrations were quantified by inductively coupled plasma optical emission spectrometry (ICP-OES 7300DV, Perkin Elmer). The method detection limit for silver ions by ICP-OES was 0.01 mg/L [109]. Silver ions were separated from the particulate form by centrifugation at $2800 \times g$ for 20 minutes (Eppendorf) in 15 mL ultrafiltration units (Amicon Ultra 4, Millipore).

3.2.1. Batch Dissolution Experiments

3.2.1.1. Short Term Experiments

Silver ion release from nAg was monitored at pH 4 and 7 under oxygen-saturated conditions (ca. 8.9 mg/L O_2). Batch experiments were conducted in duplicate in glass bottles (Corning) and mixed continuously (700 rpm). All experiments were conducted with an initial total silver concentration of ca. 3 mg/L at room temperature (23 ± 1 °C) and with 10 mM NaNO_3 as the background electrolyte. Samples were collected every twenty minutes over a period of two hours and analyzed for total silver and dissolved silver.

3.2.1.2. Long Term Experiments

Six 48-hour batch experiments were conducted to assess the dissolution kinetics of nAg in aqueous suspension as a function of dissolved oxygen (DO). Silver ion release was monitored at three different DO levels (8.9, 2 and < 0.2 mg/L) and pH 4 or pH 7 under constant stirring (700 rpm) at 23 ± 1 °C. Batch reactors consisted of glass bottles containing 100 mL suspensions of nAg solution (ca. 3 mg/L initial nAg). Samples were collected for 48 hours, with more frequent sampling (every 20 minutes) during the first 2 hours of mixing to capture nAg dissolution kinetics on a time scale relevant to the 25-min residence time of column transport studies.

3.2.2. Column Experiments

3.2.2.1. Short Term Experiments

A series of four column experiments was conducted at either pH 4 or 7 under oxygen-saturated conditions (ca. 9 mg O₂/L) to measure the transport and dissolution of nAg. Glass chromatography columns (Kontes, 12 or 16 length x 2.5 cm I.D.) were packed with acid washed 40-50 mesh Ottawa sand (sand grain density of 2.65 g/cm³ and $d_{50} = 360 \mu\text{m}$) and saturated with a background electrolyte solution (10 mM NaNO₃) based on the methods of *Wang et al.* [17]. Following a non-reactive tracer test (bromide), a three pore volume pulse of nAg suspension (ca. 3 mg/L) was introduced, followed by three pore volumes of nanoparticle-free solution. A peristaltic pump delivered both the feed solution and background electrolyte to the column in upflow mode at a flow rate of 1 ml/min. This flow rate corresponded to a pore-water velocity of ca. 7.6 m/d and yielded a column residence time of ca. 27 minutes. The influent nAg suspension was sampled at the beginning and conclusion of the pulse injection and analyzed for total (nAg + Ag⁺) and dissolved (Ag⁺) phase silver. Column effluent data were expressed as breakthrough curves (BTCs), where the concentration of nAg and Ag⁺ was plotted against the number of pore volumes delivered to the column.

3.2.2.2. Long Term Experiments

Six column experiments were performed to evaluate the transport and retention of nAg in water-saturated quartz sand and to assess the dissolution kinetics of retained nAg particles as a function of DO (8.9, 2.0 or < 0.2 mg/L) and pH (4 or 7). Borosilicate glass columns (12.5 cm length × 2.5 cm inside diameter, Kontes) were packed with washed 40-50 mesh Ottawa sand ($d_{50} = 354 \mu\text{m}$, U.S. Silica) and saturated with background electrolyte solution (10 mM NaNO₃) following the procedures of *Wang et al.* [17]. Each experiment consisted of a particle deposition phase, designed to assess nAg

mobility as a function of DO and pH, followed by a dissolution phase to evaluate the longer term release of Ag^+ from the retained nanoparticles. A flow rate of 1 mL/min corresponding to a pore-water velocity of ca. 7.6 m/d was applied, which yielded a column residence time of ca. 25.5 min. Effluent samples were collected and analyzed for total silver and dissolved silver.

3.3. Mathematical Model

3.3.1. The Transport of nAg and Dissolved Constituents

Two phases, aqueous and solid, are considered in the conceptual model of the porous medium. Consistent with the results of non-reactive tracer tests, the pore space is assumed to be fully accessible to aqueous phase flow. A general mass balance equation (i.e. ADR equation) for component i can be expressed as [91]:

$$\frac{\partial}{\partial t} (\theta_w C_w^i + \rho_b \omega_s^i) + \frac{\partial}{\partial x} \left[\theta_w \left(C_w^i v_w - D_{w_i}^h \frac{\partial C_w^i}{\partial x} \right) \right] = r^i \quad (3.2)$$

where subscript i denotes particulate and dissolved components (i.e. nAg, DO and Ag^+), C_w^i [mol/m³] is the molar concentration of component i in the aqueous phase, and ω_s^i [mol/kg dry sand] is the molar concentration of component i associated with the sand grains per unit weight of the solid phase, v_w [m/s] is the interstitial velocity of water, and $D_{w_i}^h$ [m²/s] is hydrodynamic dispersion coefficient of component i in the aqueous phase. The reaction term r^i [mol/m³ s] is the net molar rate of production of component i in the aqueous phase per unit bulk volume.

The retention of NPs in porous media is typically assumed to be described by clean-bed colloid filtration theory (CFT) [15, 108]. Consistent with this theory, particles are removed from suspension through the mechanisms of interception, diffusion, and sedimentation [25]. In the present work, a more general, modified version of colloid

filtration theory (MFT) is implemented, which was developed and validated for transport of fullerene nanoparticles (nC60, dia ca. 95 nm) in water-saturated porous media. [15] The MFT model incorporates a maximum retention capacity and rate-limited attachment kinetics, as well as a first-order expression for particle detachment:

$$\frac{\rho_b}{\theta_w} \frac{\partial \omega_s^{nP}}{\partial t} = k_{att} \psi_{att} C_w^{nP} - \frac{\rho_b}{\theta_w} k_{det} \omega_s^{nP} \quad (3.3)$$

here $\psi_{att} = \left(1 - \frac{\omega_s^{nP}}{\omega_s^{nP,max}}\right)$ [-] is a site blocking function with $\omega_s^{nP,max}$ [mol/kg soil] as the particle retention capacity of the soil. When $\psi_{att} = 1$ the model is consistent with the classical CFT. k_{att} [s^{-1}] and k_{det} [s^{-1}] are the NP attachment and detachment rate coefficients, respectively. The attachment rate coefficient can be expressed as [25]:

$$k_{att} = \frac{3(1-\theta_w)v_w}{2d_c} \alpha_d \eta_0 \quad (3.4)$$

where d_c [m] is a representative collector (sand grain) diameter, the attachment efficiency, α_d [-], represents the fraction of collisions that result in attachment of particles to the collector surface, and the single collector contact efficiency, η_0 [-], is a measure of the frequency of particle collisions with the porous medium collector surfaces. The value of η_0 can be written as the sum of contributions from each collision mechanism (i.e. *Brownian* diffusion, interception, and gravitational sedimentation) [24]:

$$\eta_0 = 2.4A_s^{1/3} N_R^{-0.081} N_{Pe}^{-0.715} N_{vdW}^{0.052} + 0.55A_s N_R^{1.675} N_A^{0.125} + 0.22N_R^{-0.24} N_G^{1.11} \quad (3.5)$$

here A_s [-], the *Happel* correction factor, a porosity dependent parameter; $N_R = \frac{d_p}{d_c}$ [-] is the aspect ratio with d_p [m] being a representative particle diameter; $N_{Pe} = \frac{U_w d_c}{D_p}$ [-] is the Peclet number; $N_{vdW} = \frac{A}{k_B T}$ [-] is the *van der Waals* number, with A [J], k_B [J/K] and

T [K] denoting the *Hamaker* constant, *Boltzman* constant, and temperature, respectively; $N_A = \frac{A}{3\pi\mu d_p^2 U_w}$ [-] is the attraction number; and $N_G = \frac{d_p(\rho_p - \rho_w)g}{18\mu_w U_w}$ is the gravity number, with μ_w [g m⁻¹ s⁻¹], U_w [m s⁻¹], ρ_p [g m⁻³], and ρ_w [g m⁻³] representing the flowing phase dynamic viscosity, approach (superficial) velocity of water, particle and aqueous phase densities, respectively. Based on the values provided in Table 3.1, the overall *Hamaker* interaction parameter, A_{123} , for the attachment of nAg “1” onto a quartz sand surface “3” with water as the intervening medium “2” was estimated $A_{123} = A_{121}^{1/2} \cdot A_{323}^{1/2} = 5.36 \times 10^{-20} J$ with $A_{121} = 1.02 \times 10^{-20} J$ [110] and $A_{323} = 28.2 \times 10^{-20} J$ [111]. Note that, although, Brownian diffusion is usually considered to be the dominant mechanism that controls the attachment of nano-sized particles to collector surfaces [18], for completeness, all three mechanisms are taken into account in Eq. 3.5. Note that, although, Brownian diffusion is usually considered to be the dominant mechanism that controls the attachment of nano-sized particles to collector surfaces [18], for completeness, all three mechanisms are taken into account in Eq. 3.5.

3.3.2. nAg Dissolution

3.3.2.1. Short Term Dissolution

The nAg dissolution reaction is assumed to take place at the nanoparticle-water interface, where silver ions are then released into the bulk aqueous phase, thereby reducing the effective size of the nanoparticles. Consistent with the approach of Liu and Hurt [47], nAg dissolution is represented using a first-order kinetic expression with respect to nAg concentration and the stoichiometric coefficients; $a_{Ag^+}/_{nAg} = 1$ and

$$a_{DO}/_{nAg} = 0.25 \text{ (Eq. 3.1):}$$

$$r^{nAg} = -k_{diss}(\theta_w C_w^{nAg} + \rho_b^* \omega_s^{nAg}) = -r^{Ag^+} = 0.25 r^{DO} \quad (3.6)$$

here $r^{Ag^+} = \frac{\partial}{\partial t} (\theta_w C_w^{Ag^+} + \rho_b^* \omega_s^{Ag^+})$, $r^{DO} = \frac{\partial}{\partial t} (\theta_w C_w^{DO})$ and $r^{nAg} = \frac{\partial}{\partial t} (\theta_w C_w^{nAg} + \rho_b^* \omega_s^{nAg})$ are the rate of change in concentrations of Ag^+ , DO, and nAg per unit volume of porous medium. k_{diss} [s^{-1}] is the nAg dissolution rate coefficient, which is a function of the specific surface area (SSA) [m^2/g] of particles:

$$k_{diss}(x, t) = k_{diss0} \cdot \frac{SSA(x, t)}{SSA_0} \quad (3.7)$$

where the subscript 0 refers to the initial condition of the system.

3.3.2.2. Long Term Dissolution (Surface Aging Model)

To quantify the effect of DO concentration on dissolution rate, a modified first-order expression was implemented to capture the dissolution behavior observed in the batch experiments. Here the previously reported approach of *Li et al.* [36] was implemented to model the effect of particle aging on Ag^+ release kinetics. Their mathematical form is based on the assumption of passivation of surface dissolution sites:

$$\ln \left(1 - \frac{C_w^{Ag^+}}{C_w^{Ag^+,f}} \right) = -k_d t \quad (3.8)$$

where $C_w^{Ag^+,f}$ (mg/L) is the maximum dissolvable concentration of Ag^+ . Assuming that nAg provides the only source of Ag^+ , the following expression can be derived from Eq. 3.8, which represents nAg concentration as a function of time (i.e. age of a particle),

$$C_w^{nAg}(t) = C_w^{nAg,0} - C_w^{Ag^+}(t) = C_w^{nAg,0} - C_w^{Ag^+,f} (1 - e^{-k_d t}) \quad (3.9)$$

where $C_w^{nAg,0}$ (mg/L) is the initial concentration of nAg in the batch reactor. The modified first-order model (Eq. 3.8) assumes that only a limited amount of silver, $C_w^{Ag^+,f}$, is available for dissolution during a given time frame.

3.3.3. Numerical Implementation

The reaction modules of HELP-1D were refined to incorporate nAg dissolution, Ag⁺ formation, and DO depletion. HELP-1D uses a Lagrangian random-walk particle-tracking approach to solve the transport and component interaction equations for the NPs, and a conventional Eulerian finite difference method is implemented to discretize reactive transport equations governing the dissolved species. Although each transport system is modeled independently, the RWPT and FD modules communicate via a message-passing module that transfers the reaction data through the sink/source term. HELP-1D tracks particle changes (in mass, size, and surface area) for sub-populations of particles as dissolution proceeds and updates associated attachment and dissolution rate parameters. A flow chart of the numerical solution is provided in Appendix I.

3.3.3.1. Lagrangian Particle-Solid Phase Interactions

The RWPT module distributes the nAg mass among discrete ‘particles’, each of which represents a sub-population (i.e., a binned collection) of actual nanoparticles. According to the RWPT method, the random path of a particle p , $x_p(t)$, is determined in discrete time steps Δt as [55]:

$$x_p(t + \Delta t) = x_p(t) + u(x_p(t), t)\Delta t + Z\sqrt{2\alpha_L|u(x_p(t), t)|\Delta t} \quad (3.10)$$

where Z [-] is a normally distributed random variable with average 0 and standard deviation 1, and u [m/s] is a corrected velocity expressed as:

$$u(x_p(t), t) = v_w(x_p(t), t) + \frac{\partial D_{w,nP}^h}{\partial x} \quad (3.11)$$

To implement the transport equation (i.e. Eq. 3.2) in the RWPT scheme, the attachment and detachment terms on the right-hand-side (RHS) of Eq. 3.3 are treated

separately. In this approach, simultaneous capture and release processes are reduced to two successive attachment and detachment steps (principle of superposition). A capture probability is computed for all suspended model particles, and then a random chance is selected for each particle (a random number from a uniform distribution ranging between 0 and 1). Those particles whose capture probability exceeds the random chance are marked as attached and fixed in their current position. The advection and dispersion terms on the left-hand-side (LHS) of Eq. 3.2 are computed using Eq. 3.10 and Eq. 3.11. Particle-soil grain interactions for each particle at a particular time are expressed by noting that:

$$\frac{dC_w^{nP}}{dt} + \frac{\rho_b}{\theta_w} \frac{d\omega_s^{nP}}{dt} = 0 \quad (3.12)$$

By substituting the attachment term from Eq. 3.3 for the solid phase accumulation term in Eq. 3.12 and rearranging the terms, the following expression for the capture probability, P_p^{att} [-], of particle p can be written:

$$P_p^{att} = -\frac{dC_w^{nP}}{C_w^{nP}} \approx -\frac{\Delta C_w^{nP}}{C_w^{nP}} = k_{att} \psi_{att} \Delta t \quad (3.13)$$

The RHS term in Eq. 3.13 corresponds to the fraction of particles that are immobilized by deposition at the soil collector surfaces during a time period Δt .

The particle detachment process is modeled in an analogous way; a particle detachment probability, P_p^{det} [-], of particle p can be calculated from the following expression:

$$P_p^{det} = -\frac{d\omega_s^{nP}}{\omega_s^{nP}} \approx -\frac{\Delta \omega_s^{nP}}{\omega_s^{nP}} = k_{det} \Delta t \quad (3.14)$$

3.3.3.2. Particle-Dissolved Phase Interactions (i.e. nAg Dissolution)

3.3.3.2.1. Short Term Dissolution

Chemical reactions are incorporated into the RWPT by assuming that, over a small time interval, Δt , the fractional change in the Ag-mass of each particle residing in a grid-block $\left(\frac{\Delta M_{p_i}}{M_{p_i}}\right)$ can be approximated by the change in the average Ag-mass of all particles over that grid-block. That is:

$$\forall i \in e: \frac{\Delta M_{p_i}}{M_{p_i}} = \frac{\Delta(\sum_p^e M_p)}{\sum_p^e M_p} \quad (3.15)$$

where ΔM_{p_i} denotes the number of moles of Ag in particle i inside grid-block e . In a control volume, $\Delta V_e = A_c \Delta x^e$, where A_c [m^2] is the cross-sectional area and Δx^e [m] is the grid spacing at element e , the molar concentration of nAg particles in the aqueous-phase can be defined as:

$$C_w^{nAg} = \frac{\sum_p^e M_p}{\theta_w^e \Delta V_e} \quad (3.16)$$

Substituting Eq. 3.16 into Eq. 3.6, rearranging, and simplifying the terms assuming that $\theta_w^e \Delta V_e$ does not vary with time at a fixed position in space, yields:

$$\frac{dC_w^{nAg}}{C_w^{nAg}} = \frac{\Delta\left(\frac{\sum_p^e M_p}{\theta_w^e \Delta V_e}\right)}{\frac{\sum_p^e M_p}{\theta_w^e \Delta V_e}} = \frac{\Delta(\sum_p^e M_p)}{\sum_p^e M_p} = \frac{\Delta M_{p_i}}{M_{p_i}} = -k_{diss} \cdot \Delta t \quad (3.17)$$

Eq. 3.17 can be used to calculate the change in Ag-content of each particle (i.e. $\frac{\Delta M_{p_i}}{M_{p_i}}$) during time step, Δt . The same approach was used to derive a similar expression for

the retained particles. As dissolution proceeds, the total surface area of nAg particles will

decrease and the SSA will increase, resulting in differential dissolution rates for nAg particles based on their age and dissolution history. While conventional continuum-based transport models cannot capture changes in NP morphology, HELP-1D accounts for particle non-uniformity caused by dissolution by tracking the surface area of each simulated sub-population of particles. The following expression is used to estimate the SSA of each particle as a function the number of moles of Ag in each particle, assuming that the particles remain spherical in shape during dissolution:

$$SSA_p = \frac{SA_p}{V_p} = SSA_{p,0} \left(\frac{M_p}{M_{p,0}} \right)^{-\frac{1}{3}} \quad (3.18)$$

where $SA_p[\text{m}^2]$ and $V_p[\text{m}^3]$ are the surface area and volume of the particle p , respectively. Here, SSA_p is calculated from Eq. 3.18 and then incorporated into Eq. 3.7 to compute the particle-specific dissolution coefficient for each time step. After summing up the number of moles of Ag dissolved from all particles in each element e during time step Δt , the nAg dissolution information is conveyed as a source/sink term to the FD module to simulate reactive transport of DO and Ag^+ :

$$r^{Ag^+}_e = -0.25 r^{DO}_e = -\frac{\sum_p^e \Delta M_p}{\Delta V_e \Delta t} \quad (3.19)$$

3.3.3.2.2. Long Term Dissolution

The incorporation of the aging-based dissolution reaction (i.e., Eq. 3.9) into the RWPT scheme was based on the assumption that over a very small time interval, Δt , within each grid block, a relative change in the nAg concentration (i.e. $\frac{dC_w^{nAg}}{C_w^{nAg}}$) is equal to

the relative change in the mass of each particle (i.e. $\frac{d\Delta m_p}{m_p}$) residing in that grid block (i.e.

$\frac{dC_w^{nAg}}{C_w^{nAg}} = \frac{d\Delta m_p}{m_p}$ for all p). The Lagrangian transformation of Eq. 8 yields the following

expression for computing the change in the number of moles of nAg due to dissolution within each time step calculation,

$$\Delta m_{p_i}^e(t) = -k_d \cdot \frac{f_a \cdot e^{-k_d \cdot t_{p_i}}}{1 - f_a(1 - e^{-k_d \cdot t_{p_i}})} \cdot m_{p_i}^e \cdot \Delta t \quad (3.20)$$

where m_{p_i} (mol) and t_{p_i} (s) denote the number of moles of Ag and age of particle i

residing in grid-block e , respectively, and $f_a = \frac{C_w^{Ag^+,f}}{C_w^{nAg,0}_B}$ is the fraction of nAg particles

available for dissolution. Here, the rate constant, k_d , represents how rapidly the particle

aging process occurs. Previous studies have also reported that aging of nAg particles (i.e.

a physical or chemical transformation) is linked to a reduction in dissolution [112, 113].

For example, *Coutris et al.* [113] reported a reduction in the bio-accessible fraction (i.e.

the water soluble and ion exchangeable fractions) of citrate-stabilized nAg particles from

$37 \pm 4.8\%$ after 2 hours to $1.8 \pm 0.1\%$ after 70 days. This finding is consistent with the

current treatment of nAg dissolution, which considers a maximum available fraction for

dissolution.

3.4. Results and Discussion

3.4.1. nAg Dissolution Kinetics

3.4.1.1. Short Term Kinetics

Formation of a small amount of Ag^+ ions (<0.02 mg/L) was observed in pH 7 batch reactors, whereas at pH 4 about 2.5% of the initial mass of silver had dissolved by the end the experiment (140 min) (Figure 3.1). At pH 4 the measured Ag^+

concentrations yielded a hyper-exponential reduction in nAg dissolution rate over the course of experiment, indicating that a first-order kinetic model would not accurately describe the observed Ag^+ release. However, a first-order model with respect to nAg concentration was able to capture early time batch dissolution data, i.e. the first 43 min of the experiment, consistent with residence time of the column (ca. 27 min). A least sum of squared residuals (LSSR) method yielded a dissolution rate constant of 0.0242 1/hr at pH 4 (r^2 -value of 0.98). This rate parameter is 2-3 folds higher than the previously reported values of 0.01 1/hr [47] and ca. 0.014 1/hr [48] measured at higher pH values of 5.6 and 5.67, respectively.

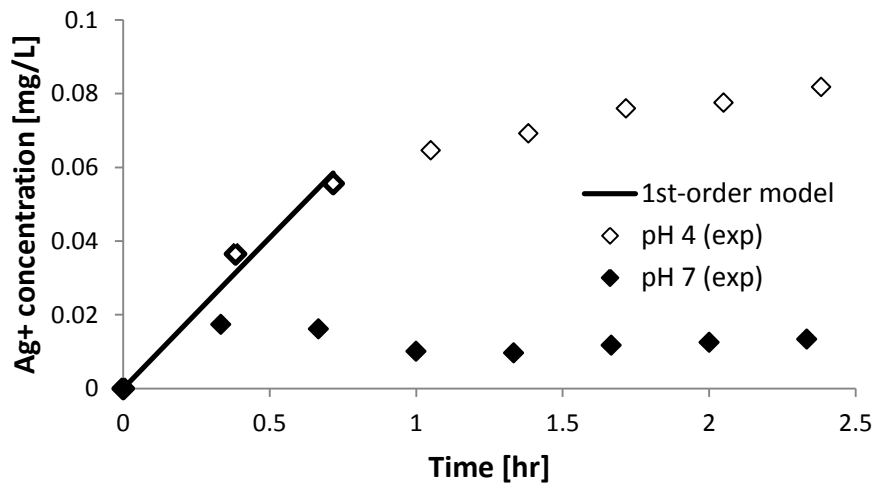


Figure 3-1. Dissolved silver ion concentrations measured in batch reactors as a function of pH and mixing time. First-order model (Eq. 3.6) fit obtained for pH 4 data set based on a LSSR procedure [114].

3.4.1.2. Long Term Kinetics

The 48 hour time release of Ag^+ from nAg suspensions at pH 7 and 4 are shown in Figs 1a and 1b, respectively [115]. Early time data for the first 2.5 hours are detailed in Figs 3.2 (c) and 3.2 (d). Ag^+ release increased with DO at pH 4 and 7 over the course of the 48-hour experiments, with higher degrees of dissolution observed at pH 4.

The modified first-order model (Eq. 3.9) assumes that only a limited amount of silver, $C_w^{Ag^+,f}$, is available for dissolution during a given time frame. Batch values for k_d were estimated using a non-linear least-squares regression program (SigmaPlot v10, Systat Software). Examination of Fig 3.2 (d) reveals that the model accurately captures early-time nAg dissolution (up to 2.5 hours) at pH 4, yielding rate constants (h^{-1}) that increase with DO content (1.25, 1.46 and 1.63 for DO concentrations of 0.2, 2 and 9 mg/L, respectively). The coefficient of determination (R^2) values for the model fits were 0.98 or higher. The model was also able to capture the general shape of the entire 48-hour data set at both pH values. The fitted dissolution rate of $0.088 h^{-1}$ for the 48 hour pH 4 air-saturated batch data (Fig 3.2 (b)) is of the same order of magnitude as values reported in previous studies [48, 116]. Overall, results of the batch studies indicate that long term nAg dissolution does not follow first order kinetics and an accurate description requires a particle surface aging model.

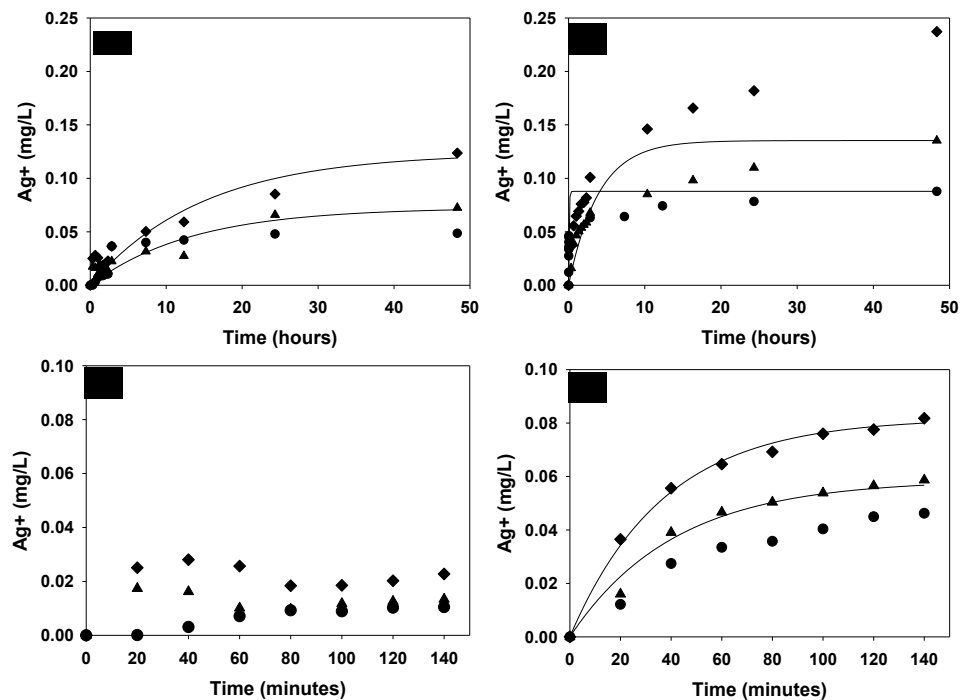


Figure 3-2. Time release of Ag^+ from nAg solutions over 48 hours at (a) pH 7 and (b) pH 4 for DO concentrations of 9 mg/L (◆), 2 mg/L (▲) and < 0.2 mg/L (●). Early time data (time 0 to

2.33 hours) for pH 7 and 4 are shown in detail in plots (c) and (d), respectively. Solid lines show modified first order model predictions for all data except early time pH 7 [115].

3.4.2. Simulation of Coupled nAg Transport and Dissolution

3.4.2.1. Short Term Transport and Dissolution

Effluent concentration data were obtained from four column experiments conducted to measure the transport of nAg and dissolved ions (Ag^+) in 40-50 mesh Ottawa sand at pH 7 and 4. A summary of column experimental conditions is presented in Table 3.1. At pH 7, ca. 83% of the injected nAg mass was recovered in column effluent samples in the form of particulate silver, with no detectable levels of Ag^+ (Figure 3.3). When the pH was reduced to 4, however, delayed breakthrough and lower maximum concentrations of nAg were observed in all three replicate columns (Figure 3.4). Substantially reduced mobility of nAg particles was observed; with only about 6% of the injected nAg mass recovered in effluent samples as nanoscale silver particles (an additional 6% was recovered as dissolved ion (Ag^+)). Batch zeta-potential measurements indicate that, at pH 7, nAg particles form a more stable aqueous suspension (- 41 mV) in comparison to that at pH 4 (-30 mV), consistent with the column results.

Table 3-1. Summary of experimental properties and model input parameters [114].

Property	Units	pH=7	pH=4 (1)	pH=4 (2)	pH=4 (3)	Source/Reference
Column porosity	-	0.362	0.360	0.370	0.367	Gravimetric measurement
Column length	cm	16.0	12.0	12.1	16.0	Gravimetric measurement
Column pore volume	mL	29.5	25.6	25.6	29.9	Gravimetric measurement
Darcy velocity	m/day	2.81	2.52	2.52	2.52	Gravimetric measurement
Peclet number	-	243	175	185	160	Bromide tracer test
Injected mass of silver	μg	275	243	234	228	ICP-OES
nAg pulse width	PV	3.02	3.08	2.88	3.04	Gravimetric/ICP-OES
Influent nAg conc.	mg/L	3.08	3.09	3.17	2.51	ICP-OES
Influent Ag^+ conc.	mg/L	0.01	0.05	0.06	0.05	Ultrafiltration/ICP-OES
Attachment efficiency	-	2.87×10^{-3}	5.69×10^{-2}	6.55×10^{-2}	5.43×10^{-2}	<i>Li et al.</i> [15] model fit
Retention capacity	$\mu\text{g/g}$	Inf.	8.51	3.91	2.80	<i>Li et al.</i> [15] model fit
Dissolution rate coefficient	1/hr	N/A	3.86×10^{-2}	3.45×10^{-2}	3.16×10^{-2}	HELP-1D fit

To examine the influence of pH on nAg deposition parameters, a single equation Eulerian nanoparticle transport model [15], based on modified filtration theory (MFT), was fit to experimental nAg effluent data using the LSSR method courtesy of Prof. Abriola's PhD student, Mr. **Becker, M.D.** This approach was used since direct application of HELP-1D to inverse problems is hindered by the stochastic oscillations around the expected value inherent in the RWPT particle transport scheme. Figures 3.3 and 3.4 (a) present a comparison of HELP- 1D simulations, using these fitted parameters, with measured nAg effluent concentration data at pH 7 and pH 4, respectively. Inspection of these figures reveals that the shape of the nAg breakthrough curve at pH 7 (Figure 3.3) is consistent with CFT model predictions (symmetric curve with a plateau region), while an MFT modeling approach is necessary to accurately represent effluent data obtained from pH 4 experiments (Figure 3.4). A single-collector attachment efficiency of 2.87×10^{-3} provided the best fit to pH 7 effluent data; at pH 4, the estimated attachment efficiencies were ca. 20 times higher, with a mean value of $(5.89 \pm 0.56) \times 10^{-2}$. The higher affinity for the sand surface was consistent with the lower negative charge of nAg at pH 4 (-30 mV) relative to pH 7 (-41 mV). A maximum retention capacity ($\omega_s^{nP,max}$) of $5.07 \pm 2.86 \mu\text{g/g}$ was estimated from the MFT-model simulations at pH 4.

At pH 7, very low concentrations of Ag^+ (<0.015 mg/L) were detected in effluent samples, consistent with the minimal nAg dissolution observed in the batch experiments. Given this absence of significant dissolution, a traditional CFT model [25] is able to capture the measured transport behavior for total silver under these conditions. Due to the significant dissolution of nAg at pH 4, however, a coupled transport/dissolution modeling approach is required to simulate total Ag concentrations. Figure 3.4 (b) provides a comparison of HELP-1D model simulations for Ag^+ breakthrough with data obtained

from the column experiments conducted at pH 4. All model input parameters are provided in Table 3.1. Inspection of the figure reveals that the hybrid model successfully captures the observed trends in Ag^+ release under dynamic flow conditions. Here the nAg dissolution rate constant (k_{diss}) was fit to reproduce each of the Ag^+ effluent BTCs. The mean dissolution rate constant obtained from the three pH 4 columns was $(3.49 \pm 0.35) \times 10^{-2}$ 1/hr. Note that, while the fitted rate constants from column experiments are of the same magnitude, they are approximately 1.4-times larger than the batch determined rate constant (i.e. 2.42×10^{-2} 1/hr). This discrepancy can be attributed to different mixing conditions in the water-saturated sand columns and batch reactors and the higher overall oxygen to silver molar ratio in the column. In addition, a higher column-based dissolution constant is consistent with the smaller residence time for the water in the columns (ca. 27 min) compared to the time interval (ca. 45 min) over which the batch-based constant was determined. *Liu and Hurt* [47] presented a batch-derived empirical correlation to estimate the rate of nAg dissolution as a function of a number of physicochemical characteristics of the aqueous medium including temperature and pH. For the conditions in the present study, this correlation yields a dissolution rate constant of 9.62×10^{-2} 1/hr, which is approximately 3 times larger than the value obtained in the batch reactors. This discrepancy is consistent with the smaller size of the nAg particles used by *Liu and Hurt* (ca. 5 nm versus ca. 12 nm diameter), which would possess approximately 2.5 times greater surface area, assuming similar particle geometries. In addition, *Liu and Hurt* used a significantly lower initial concentration of nAg (0.05 mg/L) compared to the value employed herein (ca. 3 mg/L). *Liu and Hurt* observed a decrease in the dissolution rate constant (from 3.67×10^{-2} to 2.21×10^{-2} 1/hr) with increasing total silver concentration (from 0.05 to 0.2 mg/L) at pH 5.6.

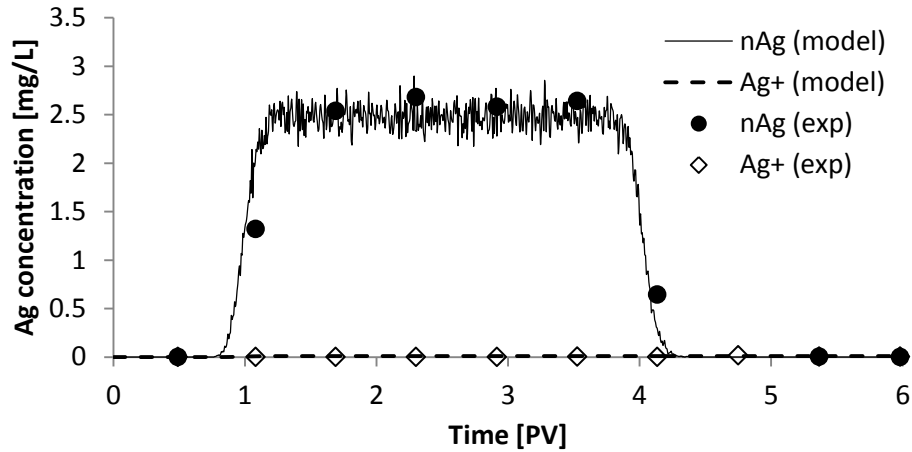


Figure 3-3. Measured and simulated effluent concentrations of nAg particles and Ag^+ ions at pH 7 performed in water-saturated columns packed with 40-50 mesh Ottawa sand [114].

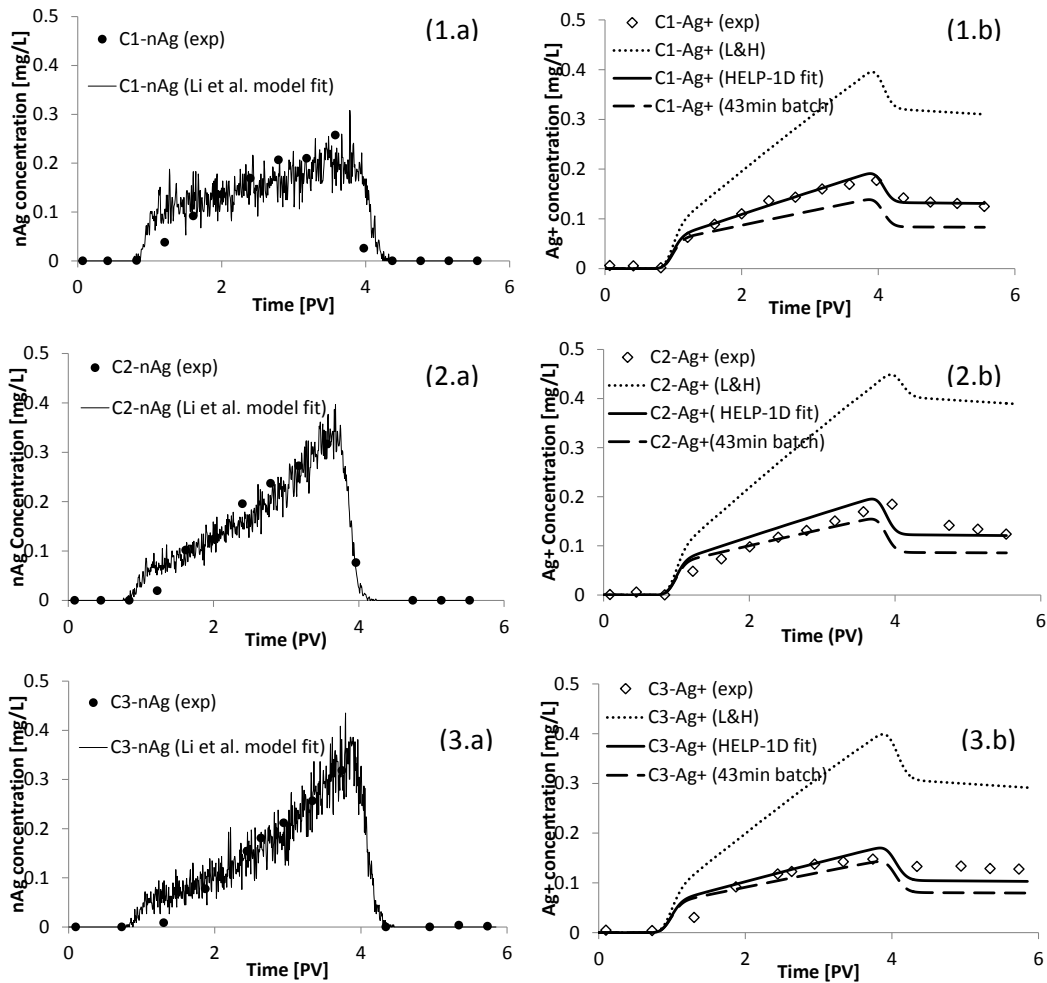


Figure 3-4. Measured and simulated effluent concentrations of (a) nAg particles and (b) Ag^+ ions in water-saturated column experiments (1, 2, 3) conducted at pH 4 [114].

3.4.2.2. Long Term Transport and Dissolution

To address aging effects on long-term dissolution of nAg, a particle surface passivation model (Eq. 3.20) was incorporated into HELP-1D. Furthermore, an nAg dissolution rate expression was developed to account for DO effect on Ag^+ release from nAg (described in this subsection). The modified model was applied to predict the nAg and dissolved solute behavior observed in a column study conducted by Prof. Pennell's group, Ms. **Mittelman, A.** and Dr. **Wang, Y.**

Aging, as a physical or chemical transformation over time, is considered essential for understanding the fate of nanoparticles in the environment [112]. To date, however, most of the effort pertaining to the aging of nanoparticles has focused on the surface oxidation of nZVI particles [117, 118]. Only a few have evaluated the aging and transformation of nAg particles [112, 113]. *Scheckel et al.* [112] did not observe any alteration in the speciation of nAg particles in their batch reactors for aging times up to 18 months. However, they purged their reactors with nitrogen to eliminate the dissolved oxygen, preventing any direct implication for our experiments. More recently, *Coutris et al.* [113] reported temporal reduction in the bioaccessible fraction (i.e. the water soluble and ion exchangeable fractions) of citrate-stabilized nAg particles from $37 \pm 4.8\%$ (with a water extractible fraction of $25 \pm 5.5\%$) after 2 hours to $1.8 \pm 0.1\%$ after 70 days of aging time. Moreover, the results of their sequential extraction analyses suggested that even at the early times (i.e. 2 hr of aging time) only a fraction of particle mass was water soluble (i.e. $25 \pm 5.5\%$). This is consistent with our treatment of nAg dissolution that considers a maximum available fraction for dissolution. Simulation results suggest a water soluble fraction of ca. 39% for the timeframe and experimental conditions of our column study.

A rate-constant of $8.4 \times 10^{-2}/\text{hr}$ and f_a of 0.39 provided the best fit to experimental observations for the oxygen-saturated system (DO = 8.9 mg/L) (Figure 3.5). Model

predictions based on Liu and Hurt (L&H) correlation [47] and the short-term batch data (i.e. 43min batch), based on a first order model for nAg dissolution with respect to nAg concentration, are also shown in Figure 3.5. For the L&H model-based simulation, nAg particles were assumed to possess an initial specific surface area of $328.95\text{m}^2/\text{g}$ as reported by Liu and Hurt [47]. In all simulations, the dissolution coefficient scales linearly with the specific surface area (SSA) of particles which in turn increases as Ag dissolves from the particles. The L&H model significantly overestimated the Ag^+ elution. This could be attributed to smaller particle sizes reported by Liu and Hurt (i.e. $< 5\text{nm}$) as opposed to those used in this study (i.e. a mean particle size of 12nm). Simulation results suggest that the implementation of 43min batch-based nAg dissolution coefficient in a true first order dissolution model underestimates the long term Ag^+ elution from the column system. Direct implementation of the aging-based dissolution parameters obtained from 24 hr batch data also resulted in significant underestimation of Ag^+ effluent concentrations. This can be attributed to the different mixing conditions in a batch reactor compared to those in a column system.

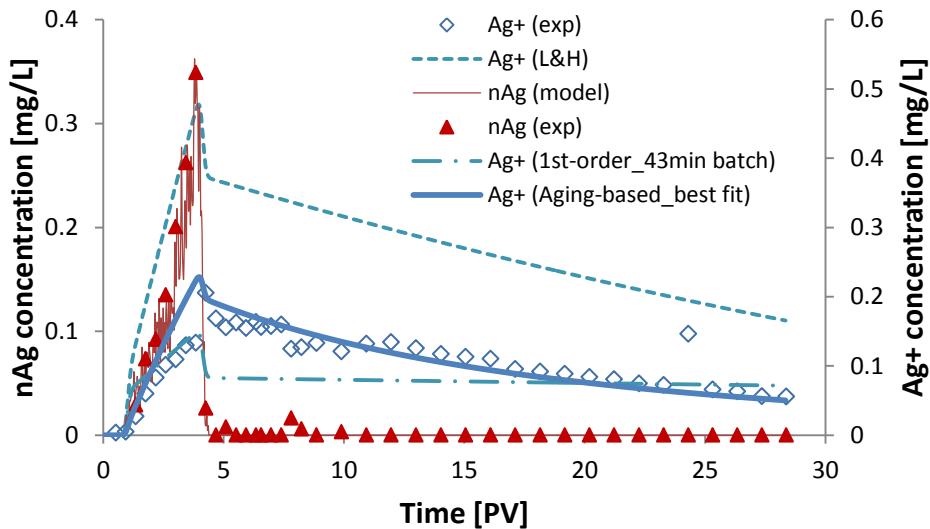


Figure 3-5. HELP-1D fits to nAg and Ag^+ effluent concentrations, and Liu and Hurt (2010) correlation based prediction of nAg dissolution.

To address the dependence of dissolution rate on DO, a reaction order of 0.25 with respect to DO-concentration was incorporated into the dissolution rate expression, consistent with the reaction stoichiometry (Eq. 3.1) where one mole of DO is consumed for every four moles of silver ion released. Hence, the following expression was derived for estimating dissolution constants at the lower DO levels (i.e., 2 and 0.2 mg/L) based on the rate constant computed for oxygen-saturated column:

$$k_d(C_w^{DO}{}_x) = k_d(C_w^{DO}{}_{sat}) \cdot \left(\frac{C_w^{DO}{}_x}{C_w^{DO}{}_{sat}} \right)^{0.25} \quad (3.21)$$

where $C_w^{DO}{}_{sat}$ and $C_w^{DO}{}_x$ [mg/L] are dissolved oxygen concentrations at saturation and at a lower level, x . The available fraction of nAg mass was held constant at $f_a = 0.39$.

Simulation results for pH 4 Ag^+ column effluent data are shown in Fig 3.6. Model predictions of Ag^+ formation and release for the DO 2 mg/L and DO 0.2 mg/L column studies based on dissolution parameters derived from model fits to DO saturated (i.e. DO = 8.9 mg/L) column data are in close agreement with Ag^+ effluent concentration data.

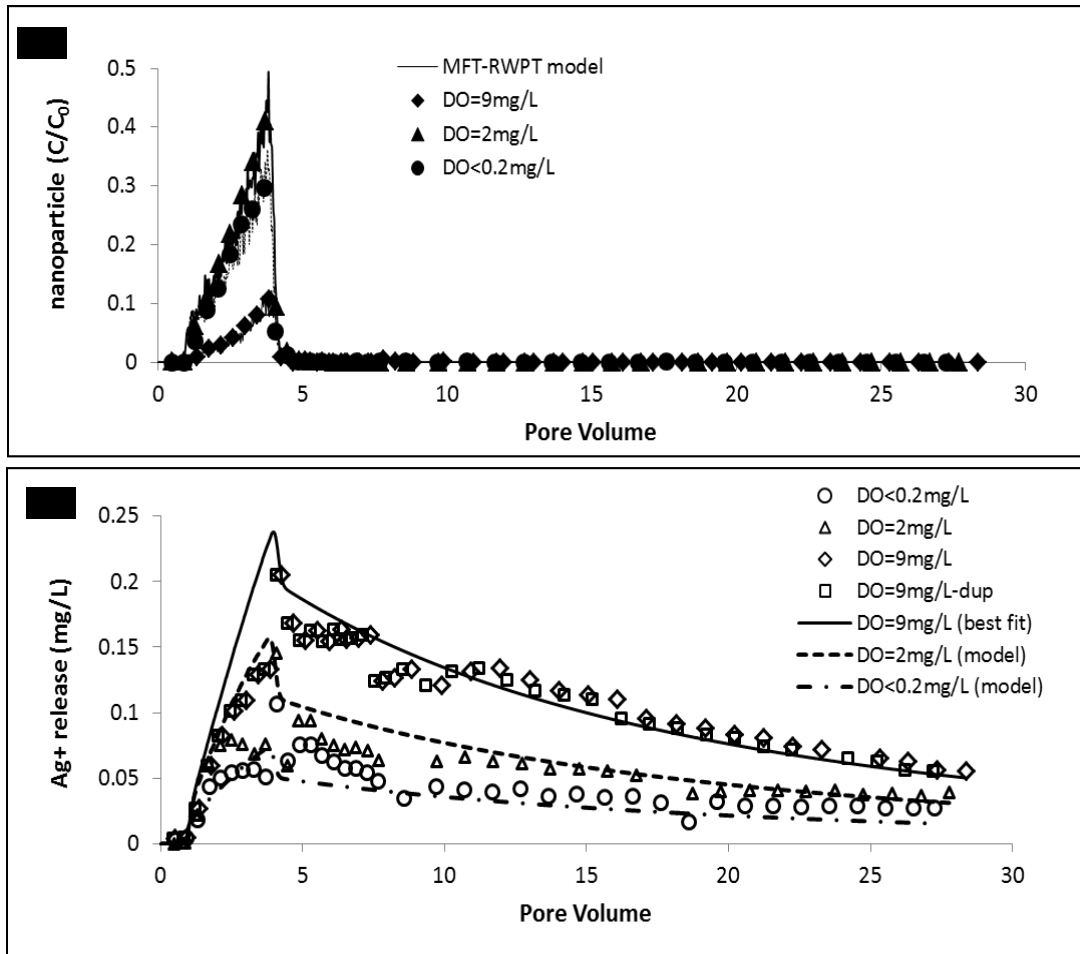


Figure 3-6. (a) Effect of dissolved oxygen concentration in pH 4 column experiments on (a) Nanoparticle breakthrough and (b) Ag⁺ breakthrough. HELP-ID fits (DO=9 mg/L) and predictions (DO=2 and <.2 mg/L) for nAg and Ag⁺ breakthrough data are shown. Inset shows nAg breakthrough during first 6 pore volumes in greater detail [115].

3.4.3. Model Sensitivity Analysis

A model sensitivity analysis was undertaken to explore the potential effects of flow velocity and particle size on the **short term** transport and dissolution of nAg particles. Several model outputs were examined, including the percent recovery of nAg, Ag⁺, and total Ag in the column effluent.

3.4.3.1. Sensitivity to Flow Rate

The applied experimental volumetric flow rate resulted in a pore water velocity of ca. 7.6 m/day, which is several times larger than typical groundwater velocities (e.g., 0.15-1.4 m/day in shallow sandy aquifers [99]). Thus, sensitivity of the model output was evaluated over a one order-of-magnitude range lower than the experimental flow (i.e., from 0.1 to 1.0 mL/min). Here, it was assumed that the nAg dissolution rate constant did not vary over the range of flow velocities considered. The attachment efficiency (α_d) of nAg particles was also assumed independent of velocity (i.e., influenced only by chemical factors), consistent with filtration theory [20, 25, 38]. Model simulations suggest that, for identical volumes of nAg injection and background solution flushing, nAg recovery will decrease (from 6% to 0%) and Ag^+ recovery will increase (from 6% to 38%) with an order of magnitude reduction in flow rate (Figure 3.7 (a)). Although an two-fold decrease in flow rate slightly reduced the total Ag elution (from 12% to 10%), when expressed in terms of total Ag recovery, further reductions in flow rate (one order of magnitude) resulted in a substantial enhancement in the total silver recovery (from 12% to 38%) (Figure 3.7 (1.a)). This behavior, which has been experimentally observed by other investigators [107], can be explained by the dependence of nAg retention on flow rate. As the flow rate is decreased, the collision efficiency (α_d) increases, resulting in enhanced retention of nAg particles. For identical injection volumes, particle residence time increases as flow velocity decreases, with a corresponding enhancement in nAg dissolution. The results of this sensitivity analysis indicate that seepage velocity will have a pronounced effect on the transport and dissolution of nAg under typical groundwater flow conditions.

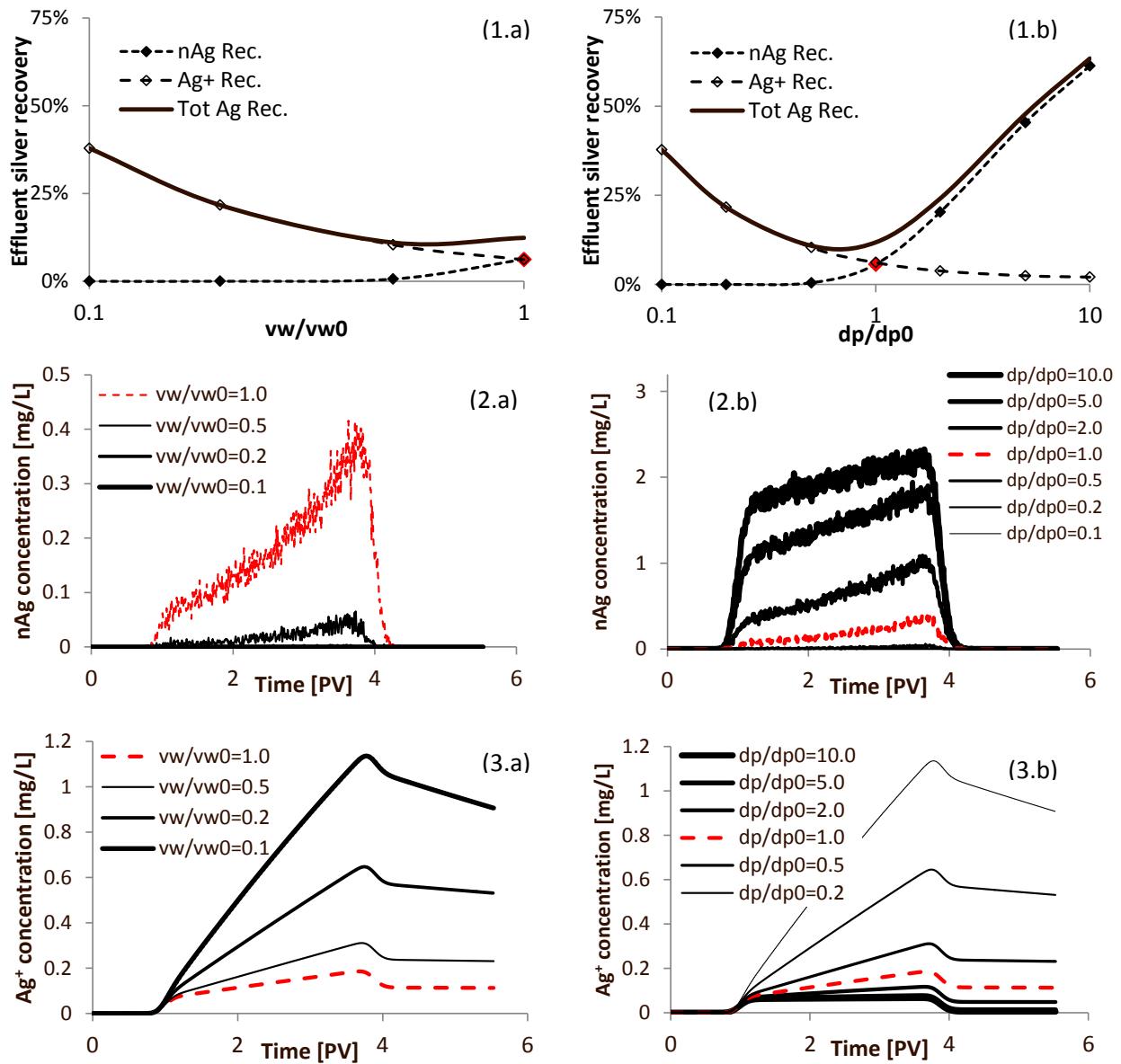


Figure 3-7. Influence of (a) applied flow rate (0.1 to 1.0 mL/min) and (b) nanoparticle diameter (12 to 120 nm) on (1) total Ag recovery and on effluent concentrations of (2) nAg and (3) Ag⁺ in water-saturated 40-50 mesh Ottawa sand at pH 4 [114].

3.4.3.2. Sensitivity to Nanoparticle Size

A number of factors, including the method of production, nAg dissolution, and ionic strength, influence the size of nAg particles in aqueous suspension. The measured mean particle diameter in this study was ca. 12 nm, while nAg sizes reported in the

literature range from less than 10 nm [47, 119] to greater than 100 nm [120, 121]. For this sensitivity analysis, the initial mean particle diameter was varied over two orders-of-magnitude, from 1.2 to 120 nm. The particle attachment efficiency (α_d) and the SSA-normalized nAg dissolution constant were assumed to be independent of the nanoparticle size. With a 10-fold increase in particle size, the model predicts an overall increase in total Ag recovery from 12% to 63%, which can be attributed to enhanced particle mobility (Figure 3.7 (b)). This behavior is a consequence of the *Tufenkji and Elimelech* [24] correlation (Eq. 3.5), which predicts a lower collision efficiency value for nAg with an increase in primary particle diameter from 12 to 120nm. Note that enhanced recovery occurs even though the recovery of Ag^+ decreases from 6% to 2%, due to the lower SSA of the larger particles. A 10-fold decrease in particle size also enhanced total Ag recovery, from 12% to 38%. This trend was attributed to an increase in nAg dissolution associated with the higher SSA of the smaller particles. Simulations predicted complete retention of particles smaller than 6 nm, resulting from the strong influence of Brownian diffusion on particle attachment, suggesting that oxidative dissolution would be the governing mechanism for Ag transport for very small particles. This is in agreement with previous studies that observed that citrate-stabilized nAg is not persistent as a particle in aquatic environments [47].

3.5. Conclusions

Findings of this study reveal the importance of accounting for nAg dissolution in the integrated assessment of nAg fate in terrestrial environments. Simulations conducted with the hybrid Eulerian-Lagrangian model were able to capture the observed transport trends of both particulate and dissolved forms of silver in column experiments. In long term, dissolved oxygen content was shown to affect dissolution kinetics of nAg in both batch and column systems, with the extent and rate of nAg dissolution increasing 2-3 fold

with an increase in DO from <0.2 to 8.9 mg/L. The coupled experimental-modeling approach demonstrates the importance of accounting for both the particulate and dissolved forms of metallic nanoparticles. The modified HELP-1D model was able to accurately simulate observed nAg and Ag⁺ column effluent data at lower DO levels (2.0 and < 0.2 mg/L) using a stoichiometric relationship. The RWPT approach may prove useful in tracking the behavior of other metallic nanoparticles prone to dissolution in aqueous environments, such as ZnO and CdSe quantum dots. HELP-1D provides a numerical framework that can be used to simulate the reactive transport of other NPs that exhibit non-uniform physicochemical characteristics and/or NPs that experience a transformation of properties based on particle-specific and/or path-specific migration in porous media.

Chapter 4 MODELING PARTICLE-PARTICLE INTERACTIONS AND THEIR INFLUENCE ON THE TRANSPORT AND RETENTION OF NPs IN POROUS MEDIA

4.1. Introduction

Stability of nanoparticles (NPs) in aqueous systems is a key factor controlling their transport and ultimate fate in aqueous environments [1]. Changes in particle shape and size resulting from particle-particle (PP) interactions (i.e. aggregation) may significantly alter transport potential [122] as well as the reactivity [9] of NPs. There have been numerous reports, particularly in the nanometer range, of the effect of particle aggregation on colloidal transport in porous media [9, 22, 34, 122, 123]. The aggregation process is then controlled by the properties of the NPs (e.g., size, chemical composition, surface charge, surface roughness and heterogeneity), and chemistry of the aqueous phase (e.g., ionic strength, pH, and NOM) [37].

Theoretically, the kinetics of particle aggregation depend on the height of the energy barrier [38]. Particles that overcome the energy barrier will aggregate with another particle in a deep primary energy minimum. The height of the energy barrier for deposition or aggregation depends directly on the size of the interacting particles, with smaller particles (i.e. NPs versus micrometer-sized particles) exhibiting much lower

energy barriers [18, 20]. Therefore, it is expected that NPs aggregate more in the primary minimum [18], implying higher propensity for aggregation for NPs compared to larger colloids. It has been suggested that nanoparticles that aggregate in primary energy minima are less likely to dissociate following changes in solution chemistry, such as reduction of ionic strength or changes in solution pH [39].

Depending upon particle surface and solution chemistry, aggregation can influence particle-soil surface collector (PC) interactions (i.e. transport and retention behavior) by increasing the effective particle hydrodynamic size. According to colloidal filtration theory [25], hydrodynamic size strongly influences the behavior of particles approaching collector surfaces. Thus, an understanding of PP interactions is imperative when considering the transport and retention of NPs in aquatic environments [18]. Unfortunately, models based upon the classical deep bed filtration theory do not have the ability to capture spatiotemporal variations in particle sizes encountered during aggregation within the porous medium. In the case of many metallic particles such as nanoiron, however, aggregation can be one of the main processes governing their environmental behavior. This is particularly true at high concentrations (i.e. in the g/L range [124]).

Smoluchowski (1917) [40] first laid the mathematical foundation for describing aggregation kinetics, and in the past few decades, the various processes governing colloidal particle transport have been subject to extensive investigation [15, 20, 25, 39]. A coupling of the mathematical formulations representing aggregation kinetics and particle transport is difficult because conventional Eulerian models conceptually employ an average particle to represent the entire population of particles and do not address non-uniform particle characteristics. Chatterjee and Gupta [21] attempted to resolve this limitation by solving the transport equation separately for each family of aggregates (i.e.

n separate transport PDEs for colloidal monomers, dimers, trimers, and n-mers) with second order production/decay terms estimated from Smoluchowski's equation. However, in their numerical implementation, they neglected PP interactions inside the simulation domain. That is, their coupled transport/aggregation mathematical model reduced to a transport-only model inside the porous medium. More recently, *Raychoudhury et al.* [123] developed a coupled finite difference model to simulate the transport of carboxymethyl cellulose (CMC)-modified nanometer sized particles of zero-valent iron (nZVI) in laboratory-scale water-saturated sand columns. Their approach, however, is subject to two limitations: (1) the assumption of occurrence of binary collisions only, and (2) a finite maximum number of primary particles for the largest cluster.

In this work, we present a general Lagrangian random-walk particle tracking (RWPT) based approach for coupling particle-soil and particle-particle interactions that is not affected by the limitations of the Eulerian approaches cited above. The RWPT method is a robust method that can easily be coupled with any flow model because of the simplicity of the explicit equations. In addition, through the implementation of particles as discrete mass parcels, global mass conservation is automatically satisfied [63]. The model development and implementation are described below. The accuracy of the numerical solution of the Lagrangian model is then verified by comparison of model outputs with those from an existing Eulerian model [123]. A model sensitivity study is then presented to explore the effects of changes in physicochemical properties on PP and, subsequently, PC interactions.

4.2. Mathematical model

A general one-dimensional mass balance equation (i.e. advection-dispersion equation) describing the transport of (chemically non-reactive) NPs in porous media can be expressed as:

$$\frac{\partial}{\partial t}(\theta_w C_w^{NP} + \rho_b \omega_s^{NP}) + \frac{\partial}{\partial x} \left[\theta_w \left(v_w C_w^{NP} - D_{wNP}^h \frac{\partial C_w^{NP}}{\partial x} \right) \right] = r^{NP} \quad (4.1)$$

where C_w^{NP} [mg/L] and ω_s^{NP} [mg/kg dry soil] are the aqueous and solid phase concentrations of NPs, respectively. θ_w [-] is soil moisture content which equals soil porosity for water-saturated conditions and ρ_b [kg/m³] is bulk density of sand. v_w [m/s] and D_{wNP}^h [m²/s] are pore water velocity and hydrodynamic dispersion coefficient of the NPs. The reaction term r^{NP} [mol/m³ s] is the net molar rate of production of NPs in the aqueous phase per unit bulk volume, which equals 0 for non-reactive particles. Here, PC interactions (i.e. NPs retention) are described by clean-bed colloid filtration theory (CFT), consistent with the approach implemented by *Raychoudhury et al.* [123], whose results are used here for model verification. According to this theory, particles are removed from the suspension through three mechanisms; interception, diffusion, and sedimentation [25]:

$$\frac{\rho_b}{\theta_w} \frac{\partial \omega_s^{NP}}{\partial t} = k_{att} \psi_{att} C_w^{NP} - \frac{\rho_b}{\theta_w} k_{det} \omega_s^{NP} \quad (4.2)$$

where ψ_{att} [-] is a site blocking function. If $\psi_{att} = 1$, Eq. 4.2 is consistent with the classical CFT model which assumes an unlimited capture capacity for the collector surfaces. k_{att} [1/s] and k_{det} [1/s] are first-order attachment and detachment constants.

The particle attachment rate constant can be expressed as [25]:

$$k_{att} = \frac{3(1 - \theta_w)v_w}{2d_c} \alpha_{PC} \eta_0 \quad (4.3)$$

where d_c [m] is a representative collector diameter (sand grain), α_{PC} [-], attachment efficiency, represents the fraction of collisions that result in attachment of particles to the collector surface, and, η_0 [-], collision efficiency, is a measure of the frequency of particle collisions with soil collector surfaces. η_0 is a function of physical characteristics of the system, which include particle size. η_0 -values are estimated from an empirical correlation presented by *Tufenkji and Elimelech* [24] (See Eq. 3.5).

PP interactions are described by the second order theoretical formulation proposed by *Elimelech et al.* [38] based on *Smulochowski's* formulation [125]. Three transport mechanisms govern the collision of particles during aggregation: Brownian diffusion (perikinetic aggregation), fluid motion (orthokinetic aggregation), and differential settling [38]. For NPs, it is recognized that Brownian diffusion is the predominant mechanism with negligible contribution from fluid shear and sedimentation [18]. The following 2nd-order expression for the time rate of change of number concentration of aggregates of rank k due to aggregation is written as:

$$\frac{dn_k}{dt} = \frac{1}{2} \alpha_{pp} \sum_{i+j=k} h(i,j)n_i n_j - \alpha_{pp} n_k \sum_{i=1}^{z-1} h(i,k)n_i \quad (4.4)$$

where α_{pp} [-] is the attachment efficiency for aggregation, n_i [m^{-3}] denotes the number concentration of i -size clusters, z is the maximum size of a cluster. Number and mass concentrations can be related by the following expression:

$$n_i = \frac{C_w^{NP} i}{m_{p(i)}} = \frac{C_w^{NP} i}{\pi/6 d_{P(i=1)}^3 \rho_p i} \quad (4.5)$$

where $d_{p(i=1)}$ [m] is the diameter of a primary particle, ρ_p [g/m³] is the density of particles, and $m_{p(i)}$ [g] is the mass of an i -size cluster.

The first term on the right hand side (RHS) of Eq. (4) denotes the formation of k -size clusters due to aggregation of lower-ranked clusters and the second term represents the loss of k -size clusters aggregating with other aggregates to create larger cluster. $h(i, j)$ [m³/s] is the second order attachment constant of j -size clusters to i -size clusters. $h(i, j)$ can be estimated from the following expression derived from Stokes-Einstein equation under diffusion-limited conditions for aggregation (i.e. $\alpha_{pp} = 1$) [38]:

$$h(i, k) = \frac{2}{3} \frac{k_B T}{\mu} \frac{(d_{p(i)} + d_{p(j)})^2}{d_{p(i)} d_{p(j)}} \quad (4.6)$$

where k_B [=1.381×10⁻²³J/K] is the Boltzmann constant, T [K] is the absolute temperature, and μ [g m⁻¹ s⁻¹] is water viscosity. When particles attach, the hydrodynamic size of the resulting cluster will be greater than that of the attaching particles (or aggregates). To account for this increase in the diameter, clusters are treated as “fractal objects”. According to this approach, the hydrodynamic diameter of an i -size cluster, $d_{p(i)}$ [m], is calculated as [123]:

$$d_{p(i)} = \left(i^{1/D_f} \right) \times d_{p(i=1)} \quad (4.7)$$

in which D_f [-] is the fractal dimension varying (based on the geometry of clusters and not the primary particles) from 3 for regular 3-dimensional objects such as spheres (case of coalescing droplets) to considerably less than 3 for irregular clusters [38]. Reported values in the literature range from 1.8 for diffusion-limited [41] to ca. 2.0 for reaction-limited conditions for aggregation under conditions of low ionic strength [123].

4.3. Numerical Implementation

4.3.1. Numerical Implementation of Particle-Collector Interactions

The above aggregation model was incorporated into the RWPT transport module of HELP-1D simulator. PC interactions (i.e. NPs retention and re-entrainment) were modeled following the approach presented in Chapter 3 of these dissertation, where two probability values for the attachment of suspended particles, P_p^{att} [-], and detachment of retained particles, P_p^{det} [-], are computed. A random chance (from a uniform distribution ranging between 0 and 1) is then selected for each model particle. Those particles whose capture/release probability exceeds the random chance are labeled as attached/suspended for the next time-step of calculations. The attachment and detachment probability values for a time interval Δt [s], can be calculated from the following expressions:

$$P_p^{att} = k_{att} \psi_{att} \Delta t \quad (4.8)$$

$$P_p^{det} = k_{det} \Delta t \quad (4.9)$$

4.3.2. Numerical Implementation of Particle-Particle Interactions

HELP-1D uses a hybrid approach to solve aggregation equation (i.e. Eq. 4.4). An Eulerian (i.e. finite difference) method was used at the inlet boundary of the domain to determine the size distribution of the influent particles as a function of time. A Lagrangian method was developed and incorporated in the RWPT model to simulate aggregation inside the domain. Implementation of Eq. 4.4 in the RWPT scheme requires its transformation to the *Lagrangian* domain. In an *Eulerian* approach, the observer looks at a fixed aggregate size, k , at a fixed position in space, and calculates how many k -size clusters are formed (due to association of smaller clusters) and how many k -size clusters are lost (due to association of k -size clusters with other clusters). The same procedure

needs to be repeated for all values of k up to the maximum value, z (Eq. 4.4). In a *Lagrangian* approach, however, all processes are explicit in time and the observer moves with aggregates.

Unlike *Eulerian* clusters that are born and may die so that a higher ranked cluster is created, *Lagrangian* aggregates are neither born nor lost; they **evolve** as they interact with other particles. That is, at a fixed point in time, one does not account for what might produce new clusters of a particular size. In other words, in a Lagrangian approach all particles are analogous to “primary” particles in an Eulerian approach. Hence, the first term on the RHS of Eq. 4.4 is the only term that must be implemented in a Lagrangian scheme. Rearranging the remaining terms, the following expression can be derived from Eq. 4.4 to determine an aggregation probability, $\mathbf{P}_{p(i) \leftarrow p(j)}^{agg}$ [-], for association of a j -size cluster with an i -size cluster:

$$\mathbf{P}_{p(i) \leftarrow p(j)}^{agg} = -\frac{dn_i}{n_i} = \alpha_{pp} h(i, j) n_j \Delta t \quad (4.10)$$

Similar to the procedure applied for modeling PC interactions, a random chance is selected for each neighboring particle pair and those pairs whose aggregation probability exceeds the random chance are marked as “clustered”. The new cluster size will be equal to the summation of cluster sizes of the two aggregating particles and the new cluster diameter can be calculated from Eq. 4.6.

Note that there is no systematic constraint on how large clusters can grow. As particles grow in size, however, new governing mechanisms can influence PC (e.g., physical straining) and PP (e.g., differential settling) interactions. HELP-1D is readily capable of addressing straining effects on NP retention, however, the current model can describe PP interactions only within the range of dominance of Brownian diffusion.

Also note that in the proposed probabilistic approach, regardless of attachment of any given pair, clusters will have a chance to interact with and attach to other surrounding clusters during the time increment Δt . This removes the binary collisions constraint from our proposed approach. Modeling aggregation for all existing particle pairs, however, can be computationally intensive. To overcome this problem, we suggest limiting the allowable spatial range for aggregation, based on the limited diffusion length of the nano-scale Brownian particles. The diffusion coefficient, D_∞ [m²/s], of a particle of diameter d_p [m] in an infinite medium with an absolute viscosity μ [g m⁻¹ s⁻¹] at temperature T [K] is expressed [24] as:

$$D_\infty = \frac{k_B T}{3\pi\mu d_p} \quad (4.11)$$

For the smallest particle size in the nanometer range (i.e. 1 nm) suspended in water ($\mu_w = 1 \text{ g m}^{-1} \text{ s}^{-1}$) at room temperature (23°C), Eq. 4.11 estimates a diffusion coefficient of $4.34 \times 10^{-10} \text{ m}^2/\text{s}$. This yields a diffusion length of $9.316 \times 10^{-5} \text{ m}$ over a 5 s time period. In this study, we have limited the time step sizes to 5 s and, thus, in the simulations presented here the allowable spatial range for aggregation was set to 1 mm which is one order-of-magnitude greater than the calculated diffusion length. The diffusion lengths of larger particles (i.e. $d_p \geq 1 \text{ nm}$) over smaller time intervals (i.e. $\Delta t \leq 5 \text{ s}$) will be smaller than $9.314 \times 10^{-5} \text{ m}$. Also note that the primary particle size used in this study was 45 nm (as reported by *Raychoudhury et al.* [123]).

4.4. Results and Discussion

4.4.1. Verification of the Coupled Aggregation-Transport Model

HELP-1D was applied to reproduce the results of a coupled Eulerian transport and aggregation model (herein called R-model) developed by *Raychoudhury et al.* [123].

They applied R-model to simulate the transport of aggregating CMC-coated nZVI particles in a series of column experiments. Experiments consisted of continuous injection of 8 pore volumes of CMC-nZVI at three input concentrations of 70, 200, and 725 mg/L into 9 cm long water-saturated mesh 40-45 silica sand columns at pH 7.4±0.4 with a background electrolyte concentration of 0.1 mM NaHCO₃. The particle residence time in the reservoir syringe ranged from 0 to 48 min, and the average residence time in the column was ca. 6.5 min. CMC-nZVI was stirred gently in the syringe pump to prevent settling [123], however, the feed suspension was not sonicated to allow for NPs aggregation in the reservoir.

Table 4-1. Summary of experimental properties and model input parameters reported by Raychoudhury *et al.* [123].

Property	Symbol	Unit	Value
Packed Length	L_c	cm	9.0
Moisture content	θ_w	–	0.32
Dispersion coefficient	D_{wNP}^h	m ² /s	5.0×10^{-7}
Mean sand grain size	d_c	µm	375
Primary Particle size	$d_{p(i=1)}$	nm	45
Darcy velocity	q_w	m/day	6.4
Input CMC-nMag concentration	$C_{w,0}^{NP}$	mg/L	725
Attachment efficiency	α_{pc}	–	0.12
Aggregation efficiency	α_{pp}	–	3.08×10^{-4}
Fractal dimension	D_f	–	2.0

A summary of model input parameters is presented in Table 4.1. The effluent concentrations of CMC-nZVI, simulated by R-model and HELP-1D, were compared for the 725 mg/L experiment ($\alpha_{pp} = 3.08 \times 10^{-4}$). This experiment was selected because the influence of aggregation on the NP transport was the most pronounced (compared to the 70 mg/L (α_{pp} : not reported) and 200 mg/L ($\alpha_{pp} = 1.85 \times 10^{-4}$) experiments). HELP-1D successfully mimicked R-model results (Figure 4.1 (a)). During the experiment, the dimensionless effluent NP concentration (i.e. C/C_0 -value) increased from

0.44 at 2 PV to 0.54 at 8 PV (Figure 4.1 (a)). This enhancement in the transport can be explained by PP interactions. Note that system hydrodynamics would be different in the inlet reservoir and inside the column potentially resulting in differential aggregation rates. HELP-1D, therefore, requires separate specification of α_{pp} -values applicable to the inlet boundary and the porous medium. Here, however, identical aggregation efficiencies were used consistent with the single value reported by *Raychoudhury et al.* (i.e. $\alpha_{pp} = 3.08 \times 10^{-4}$).

Figure 4.1 (b) presents the HELP-1D predictions for the influent and effluent PSD curves consistent with these times. Note that the predicted average (volumetric mean) diameter of effluent particles increased from 195 to 255 nm. The corresponding collision efficiencies (i.e. η_0), as computed from Eq. 3.5 (Subsection 3.3.1), are ca. 0.024 and 0.020, respectively (Figure 4.1 (c)). Recall that collision efficiency is linearly related to attachment rate constant, k_{att} (Eq. 4.3), where a lower collision efficiency yields lower retention. Figure 4.1 (a) also shows that the slope of the fitted NPs breakthrough curve (BTC) decreased gradually with time. This decline in the enhancement of the transport of NPs can be explained by comparing PSD curves of NPs entering and exiting the column at different times (Figure 4.1 (b)). The predicted average diameter of influent particles was ca. 85 nm at 1 PV, which then increased to 195 nm when particles reached column outlet ($x = 9 \text{ cm}$) at 2 PV. This yielded an outlet to inlet aggregate size ratio of ca. 2.3, which decreased to ca. 1.2 at the end of simulation when predicted average influent and effluent aggregate diameters were 215 (at 7 PV) and 255 nm (at 8 PV), respectively. Given the constant influent NP concentration, an increase in particle sizes (due to aggregation) reduces the number-concentration of particles (i.e. n in Eq. 4.4). This decrease in n reduces the likelihood of PP interactions, as aggregation kinetics has a second order dependence on n . Moreover, the slope of the collision efficiency-particle

diameter curve decreases with increase in particle diameter in the 50 to 350 nm range (Figure 4.1 (c)). That is, for nZVI particles subject to the reported experimental conditions, collision efficiency becomes less sensitive to a change in aggregate diameter when the particle sizes increases from 85 to 215 nm.

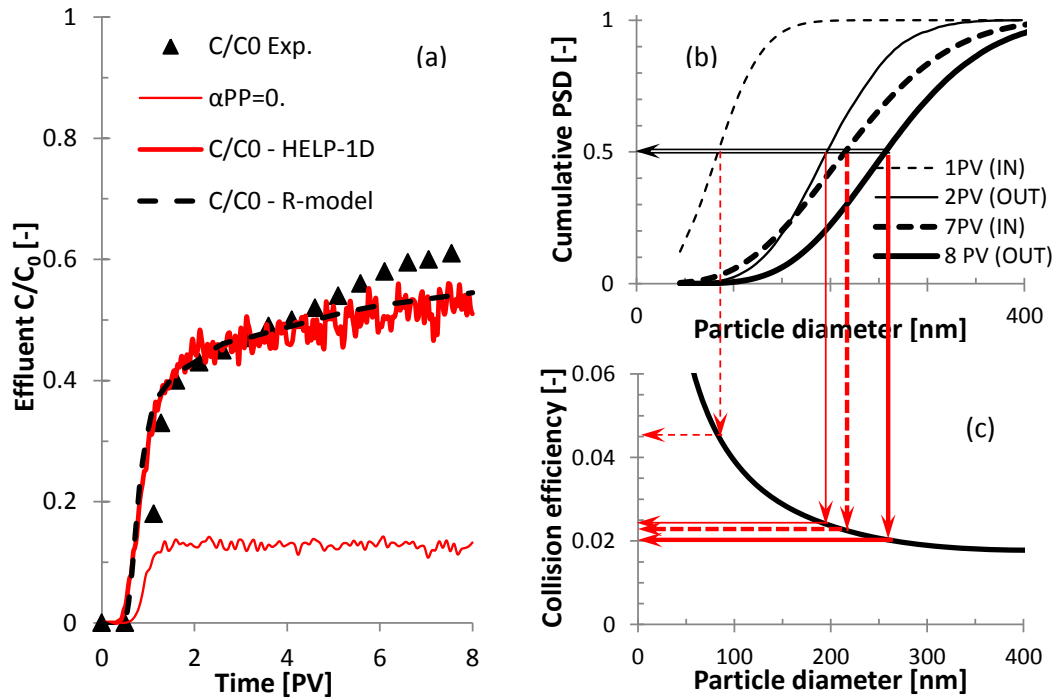


Figure 4-1. (a) Experimental (\blacktriangle) and modeled (HELP-1D – solid and R-model – dashed lines) effluent CMC-nZVI concentrations, (b) influent (dashed lines) and effluent (solid lines) cumulative volumetric PSD curves predicted by HELP-1D, and (c) changes in collision efficiency with particle diameter (50-400 nm) at flow velocity of 6.4 m/day.

Further inspection of Figure 4.1 (a) reveals that neither one of the coupled aggregation-transport models fully describe the observed increase in the effluent concentrations after the first 4 pore volumes. *Raychoudhury et al.* attribute this discrepancy to NP detachment and use a detachment rate constant of $5 \times 10^{-3} \text{ min}^{-1}$ to provide a better fit to their experimental effluent data. Particle detachment, however, seems an unlikely scenario because of the small energy barrier associated with NPs [20]. Therefore, the deposition of NPs is likely to occur in the primary energy minimum [18].

Chen and Elimelech [39] observed that NPs that deposit in primary energy minima are less likely to be re-entrained following changes in solution chemistry (e.g., changes in ionic strength (IS) or solution pH). In *Raychoudhury et al.*'s column study, a constant solution chemistry was maintained during the course of all experiments (including the 725 mg/L experiment – IS: 9.6 mM, pH: 7.4±0.4), which further reduces the probability of NP detachment. Furthermore, *Raychoudhury et al.* could have easily investigated the validity of their hypothesis had they implemented a pulse (rather than a continuous) NP injection scheme, as in the case of NP detachment, the detaching particles produce a tailing in the NP BTCs after the injected pulse elutes from the column. Unfortunately, they only implemented a continuous injection scheme in all of their experiments.

Site-blocking, based on the idea of a finite maximum retention capacity for the collector surfaces, is another process that can potentially explain temporal increases in the NP effluent concentrations. *Raychoudhury et al.*, however, reject the possibility of site-blocking through two main reasons; (1) a small surface coverage of the collector grain surfaces (0.015-0.24% at 8 PV), and (2) a reduction in effluent concentrations with an increase of the influent concentration.

Despite this reasoning, the author of this dissertation believes that site-blocking can be a relevant process, because:

- (1) There have been other studies reporting site-blocking effects for similar surface coverage levels (e.g., ca. 0.1% for the quantum-dot NPs [126] to ca. 0.9% reported for silver NPs [115]). Furthermore, *Mittelman et al.*'s [115] SEM images of the deposited silver NPs indicated that the NP deposition occurred in sparse patches on the sand surface, which is consistent with the potentially significant sensitivity of

NPs to “patchwise geochemical heterogeneities” and/or collector surface roughness [18].

- (2) Under a given set of physicochemical conditions, the effluent C/C_0 -values are expected to increase with an increase in the influent concentration due to site-blocking effects. This, **apparently**, contradicts with the trend seen in *Raychoudhury et al.*'s study where the measured average C/C_0 decreased from ca. 0.7 to 0.5 as the influent concentration was increased from 70 to 725 mg/L. The missing key factor in *Raychoudhury et al.*'s argument is the “solution chemistry”! According to their report, the increase in the influent concentration was associated with a significant increase of the effective IS from 1.2 (at 70 mg/L) to 9.6 mM (at 725 mg/L), which in turn, is expected to facilitate NP deposition by suppressing the repulsive forces acting on particles approaching a collector surface. That is, the surface capacity for NP deposition is subject to change and would increase with an increase in the solution IS [127]. Therefore, comparing effluent C/C_0 -values for different C_0 -values for different systems with dissimilar retention capacities is unjustifiable.

4.4.1.1. Polyadic Collisions vs. Binary Collisions

As an Eulerian model, the R-model only simulates binary collisions; therefore, when higher order collisions (i.e. ternary, quaternary... and n-ary (a.k.a. polyadic) collisions) are taken into account, a potential enhancement in the degree of aggregation is expected. In order to test this hypothesis, an option for eliminating higher order collisions was added to HELP-1D, simply by precluding particles marked as “clustered” during a time step from further interaction (i.e. aggregation) with its surrounding particles.

When aggregation occurred both inside the column and at the column inlet (Figure 4.2 (a)), the comparison of simulations conducted in the binary and polyadic modes did not reveal any detectable variation in the NP elution from the column (binary: 43.0% vs. polyadic: 43.2%) or the mean effluent particle diameter (50% quantile - d_p^{50}) (binary: 248 nm vs. polyadic: 249 nm) (Figure 4.2 (c.1)). Further inspection of predicted size distributions of effluent particles showed that the 90% quantile values (d_p^{90}) were similar for binary (350 nm) and polyadic (352 nm) models. For the d_p^{99} values the difference was more pronounced (binary: 441 nm vs. polyadic: 450 nm) (Figure 4.2 (c.2)), however, this difference in NP size is applicable to only ca. 1% (by weight) of particles which explains the similarity of predicted NP elution by the binary and polyadic models. Here d_p^x [nm] is defined as the NP diameter at weight percentage equal to x%.

However, further analyses suggest that higher than binary order collisions may have a significant effect on the modeling results under a different set of experimental conditions. For example, if the aggregation process was limited to only inside the column (a condition that can be attained by sonication of particles in the inlet reservoir), HELP-1D results suggest that the consideration of polyadic collisions results in an increase in the predicted NP mobility (ca. 36.5% elution) in comparison with that from a binary collisions-based solution (ca. 34% elution) (Figure 4.2 (b)). Higher order collisions also influenced the predicted mean diameter of effluent particles (binary: 165 nm vs. polyadic: 183 nm) (Figure 4.2 (c.1)).

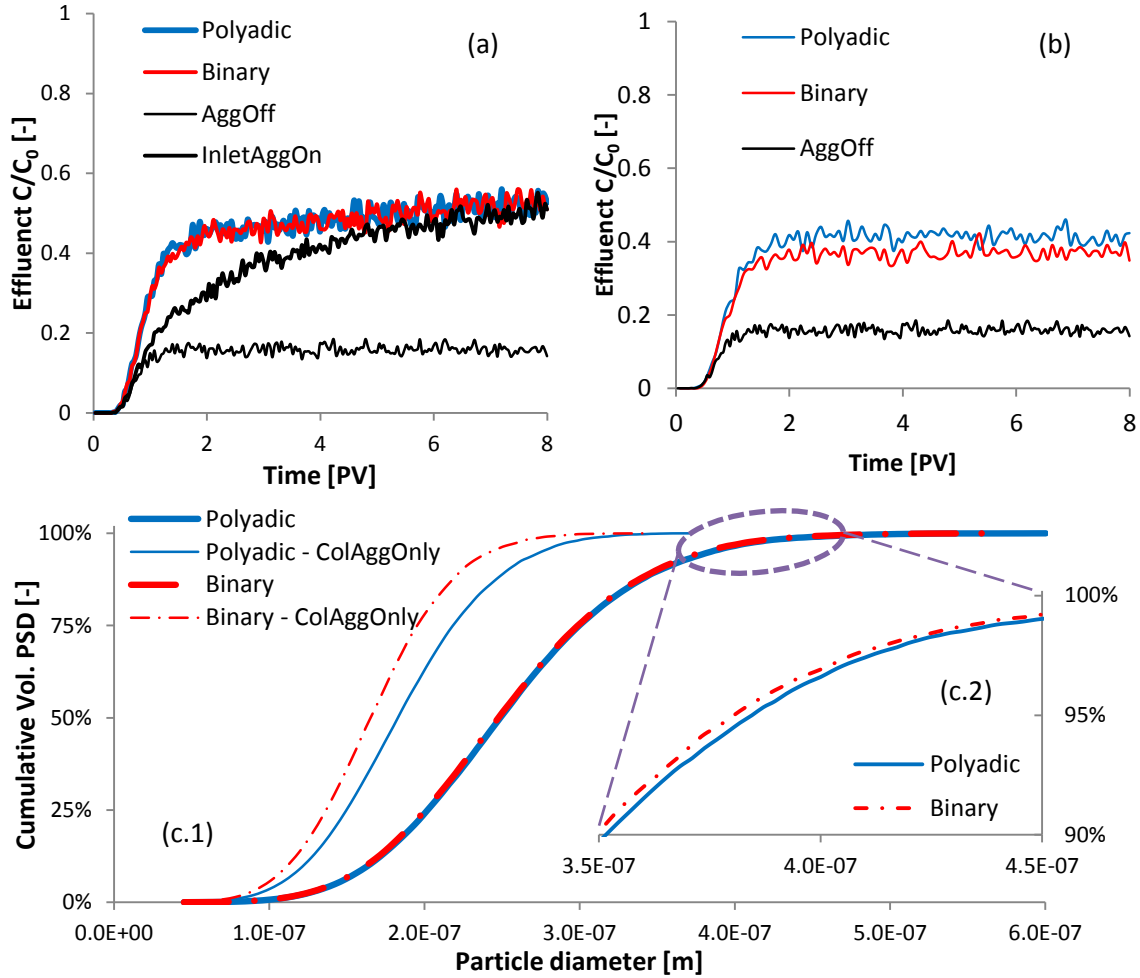


Figure 4-2. Comparison of simulated CMC-nZVI BTCs based on binary (shown in black) and polyadic (shown in red) (a) with aggregation at the inlet boundary and inside the column, and (b) with aggregation only inside the column for $C_{0,NP} = 725$ mg/L, and (c) the predicted cumulative volumetric particle size distribution for each simulation after 80 PV.

4.4.1.2. Numerical Approximation in the Lagrangian Solution

The RWPT method does not exhibit numerical dispersion; however, a very large number of particles is usually necessary to attain satisfactory results from RWPT [55], as the statistical fluctuation (i.e. associated with variable Z in Eq. 4.7) is inversely proportional to the square root of the number of particles in an averaging volume [63]. Increasing the number of model particles, however, is at the expense of increased time and memory requirements, based upon the fact that the transport equation is solved

separately for each model particle, and the aggregation equation for all neighboring particle pairs. A total number of 485.5×10^3 model particles (ca. $60 \times 10^3/\text{PV}$) was injected for the simulation shown in Figure 4.1, where a computational time of ca. 154 min was recorded on an Intel(R) Xeon(R) E31245 CPU (3.30GHz). The effect of the number of injected model particles on model predictions was explored by running a series of simulations with variable model particle flux (J_{in}^{mP} [1/PV]). Increasing J_{in}^{mP} resulted in a decrease in stochastic fluctuation (i.e. increased precision) as expected (Figure 4.3 (a)). However, when J_{in}^{mP} increased from $12 \times 10^3/\text{PV}$ to $240 \times 10^3/\text{PV}$, the computational time increased significantly from ca. 29 min to 25.44 hr. The computational time exhibits a second order relationship with the number of model particles (r^2 -value of 1) (Figure 4.3 (b)), which is consistent with the second-order (aggregation model-induced) dependence of the number of computational operations on the number of model particles. The computational time and particle flux ratios plotted in Figure 4.3 (b) were calculated by normalizing the time to complete a simulation and the applied model particle flux by corresponding values used in the original simulation (i.e. $60 \times 10^3/\text{PV}$ and 154 min), respectively.

Decreasing J_{in}^{mP} to save computational time and memory, in addition to reducing the precision of the numerical solution of both the aggregation and transport equations, also may compromise the numerical accuracy of the Lagrangian solution to the aggregation equation (i.e. Eq. 4.4). A discrepancy between model predictions of effluent NP concentration was observed based on the chosen value for J_{in}^{mP} (Figure 4.3 (a)). Model predictions converged, however, when the selected J_{in}^{mP} -value was greater than $60 \times 10^3/\text{PV}$ (< 3% difference by area under curve between 60 and 240 k/PV curves and < 1% between 120 and 240 k/PV curves).

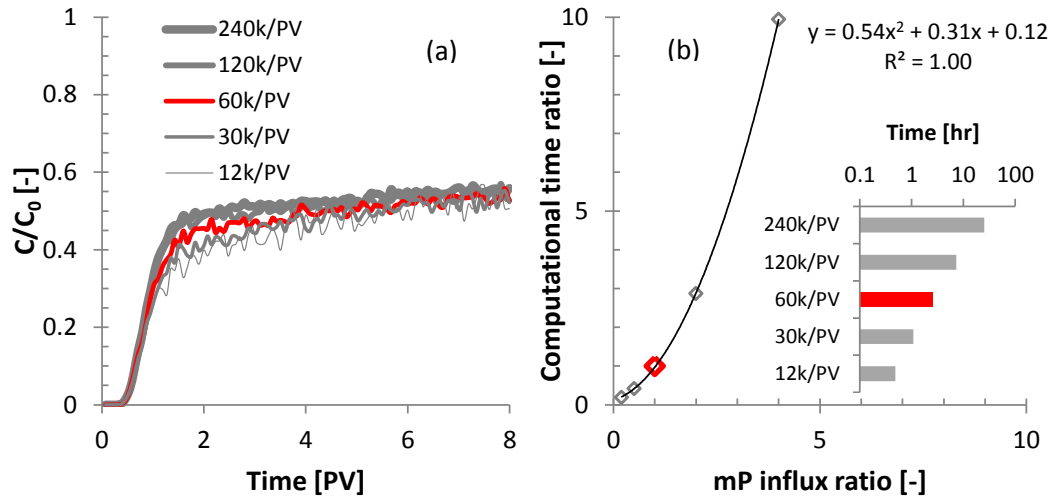


Figure 4-3. Effect of changes in the influx of model particles on (a) predicted effluent NP concentrations and (b) computational time.

4.4.2. Sensitivity Analysis

A model sensitivity study was undertaken to explore the effects of physicochemical characteristics of the system on PP and PC interactions. Four modeling parameters (including pore water velocity, influent particle concentration, aggregation efficiency, and primary particle diameter) were varied and the changes in concentration and PSD of effluent particles were investigated. A summary of scenarios implemented in the sensitivity study is provided in Table 4.2. For all scenarios, simulations included aggregating particles considering binary (B) and polyadic (P) collisions, and non-aggregating particles ($\alpha_{PP} = 0$). Numbers reported in this subsection for aggregating particles, unless otherwise indicated, reflect predictions based on binary collisions.

Table 4-2. Summary of scenarios considered in the sensitivity study.

Case #	Varying parameter	v_w [m/day]	$C_{w,0}^{NP}$ [mg/L]	α_{PP} [-]	d_p [nm]
<i>Original scenario</i>					
		6.4	725	3.08×10^{-4}	45
1	Particle velocity	1.28–6.4	725	3.08×10^{-4}	45
2	Influent concentration	6.4	72.5–725	3.08×10^{-4}	45
3	Aggregation efficiency	6.4	725	3.08×10^{-5}– 3.08×10^{-3}	45
4	Primary diameter	6.4	725	3.08×10^{-5}	10–100

4.4.2.1. Sensitivity to Flow Velocity

The experimental flow rate applied by *Raychoudhury et al.* [123] resulted in an interstitial velocity of ca. 6.4 m/day, which is at the upper range of typical groundwater velocities (e.g. 0.15-1.4 m/day in shallow sandy aquifers [99]). Thus, the interstitial velocity was reduced 5 fold and the influence of velocity on PP and PC interactions was explored in the range of 1.28 – 6.4 m/day. It was assumed that attachment (α_{PC}) and aggregation (α_{PP}) efficiencies do not vary with pore water velocity (i.e. depending only upon chemical factors) consistent with filtration theory [38].

Results of these simulations are presented in Figure 4.4. For an identical volume of injected suspension, a 5-fold reduction of velocity reduced the percent NP elution for aggregating particles ($\alpha_{PP} = 3.08 \times 10^{-4}$) from 41.3% to 13.6%, and increased the average effluent particle diameter from ca. 230 ($\eta_0 = 0.020$) to 410 nm ($\eta_0 = 0.070$) (Figures 4.4 (b) and (c)). In comparison, a filtration-only scenario (i.e. $\alpha_{PP} = 0$ and $d_{p(i=1)} = 45$ nm) yielded a reduction in NP elution from 14.3% ($\eta_0 = 0.074$) to less than 0.7% ($\eta_0 = 0.235$). While both coupled (i.e. filtration and aggregation) and

filtration-only models predict an overall decline in the effluent concentration, it is noteworthy that the difference between the predicted NP elution curves increases as flow velocity decreases. That is, NP elution from the coupled model was ca. 3 times greater than that predicted by filtration-only model (i.e. an aggregation-induced elution enhancement of 300%) at a pore velocity of 6.4 m/day; this ratio increased to ca. 20 when velocity was reduced to 1.28 m/day. This magnification of the effect of aggregation on the transport characteristics of NPs is associated with the increased residence time of particles in the column at a lower velocity.

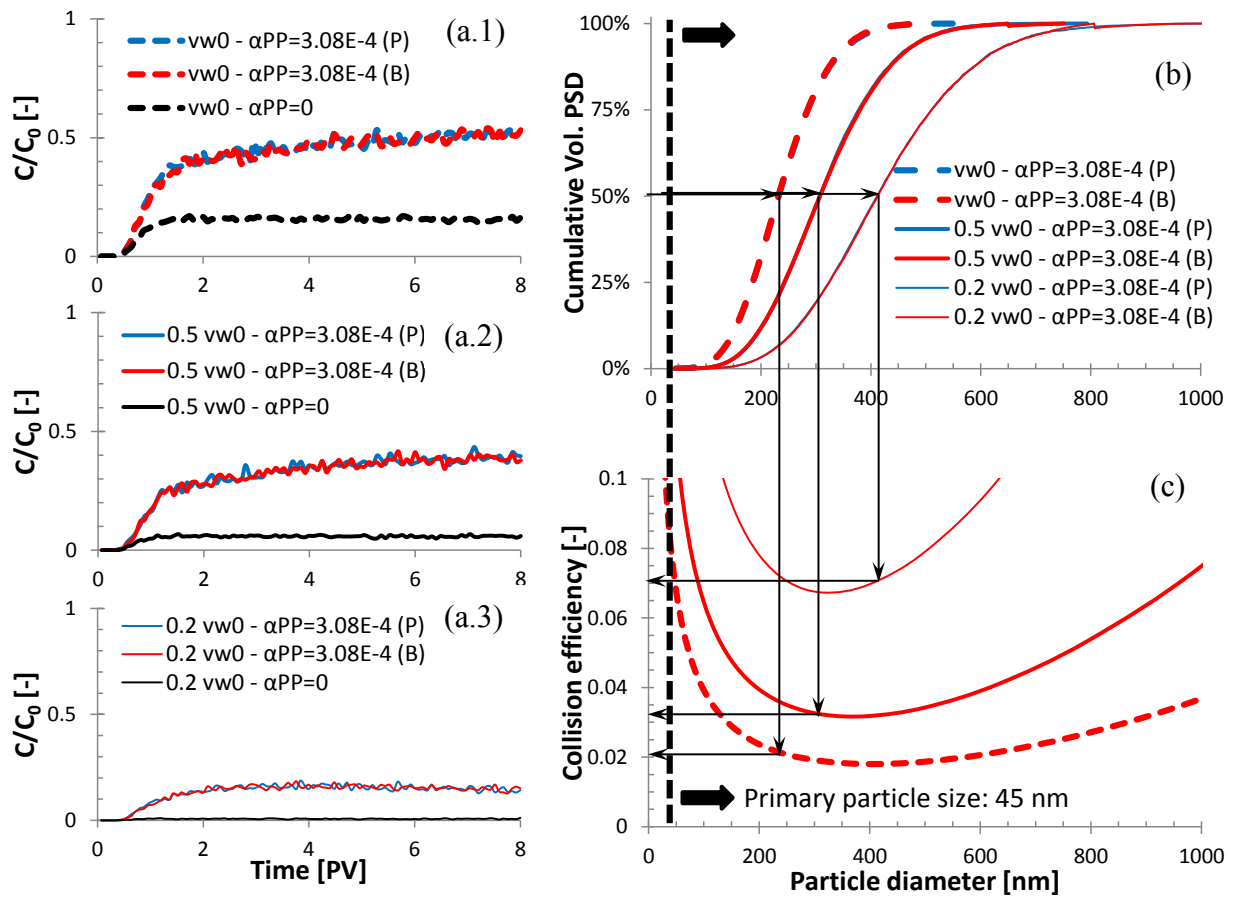


Figure 4-4. Influence of pore water velocity on (a) effluent NP concentration for aggregating (in red and blue) and non-aggregating (in black) particles, (b) predicted cumulative volumetric PSD curves for effluent NPs, and (c) collision efficiency – particle diameter relationship.

Simulations results did not exhibit any sensitivity to higher order collisions, and predicted similar effluent concentrations for scenarios based on polyadic (P) and binary (B) collisions (Figure 4.4 (a)). While the maximum aggregate diameters predicted by (P) model exceeded those predicted by (B) model (e.g., ca. 580 nm (P) vs. 500 nm (B) ($v_w = 6.4$ m/day) and ca. 800 nm (P) vs. 750 nm (B) ($v_w = 3.2$ m/day)), the volumetric average diameter of effluent particles were equal (e.g., ca. 230 nm (P & B) ($v_w = 6.4$ m/day) and ca. 300 nm (P & B) ($v_w = 3.2$ m/day)) (Figure 4.4 (b)) which is consistent with the similarity in the NP elution predictions by (P) and (B) models.

A significant difference between (P) and (B) models predictions was observed, however, when PP interactions were restricted to the time of transport within the porous medium (i.e. no aggregation at the inlet reservoir) (Figure 4.5). Considering polyadic collisions increased the predicted NP elution by 13% (from ca. 32.7% (B) to 36.9% (P) (Figure 4.5 (a.1))) for the pore water velocity of 6.4 m/day. This difference in predicted NP elution then increased to ca. 27% (from ca. 20.3% (B) to 25.9% (P) (Figure 4.5 (a.2))) and 58% (from ca. 7.2% (B) to 11.4% (P) (Figure 4.5 (a.3))) when v_w decreased to 3.2 m/day and 1.28 m/day, respectively. Also, the difference between effluent PSD curves predicted by (P) and (B) models was more pronounced at lower velocities (Figure 4.5 (b)). When v_w decreased from 6.4 to 3.2 m/day the ratio of the average effluent NP diameter predicted by (P) model to that predicted by (B) model (i.e. $d_p^{50}(P)/d_p^{50}(B)$) increased from ca 1.2 (194 nm/164 nm (Figure 4.5 (b.1))) to ca. 1.3 (232 nm/180 nm (Figure 4.5 (b.2))).

This suggests that higher order collisions are more likely to influence aggregation kinetics when the primary particles comprise a large fraction of interacting particles. The number concentration of particles which has a second-order dependence on aggregation

kinetics, in turn has a second-order dependence on the diameter of particles for the chosen fractal dimension (i.e. $D_f = 2.0$), and thus, a decrease in size of particles significantly enhances PP collisions which include binary and higher order collisions.

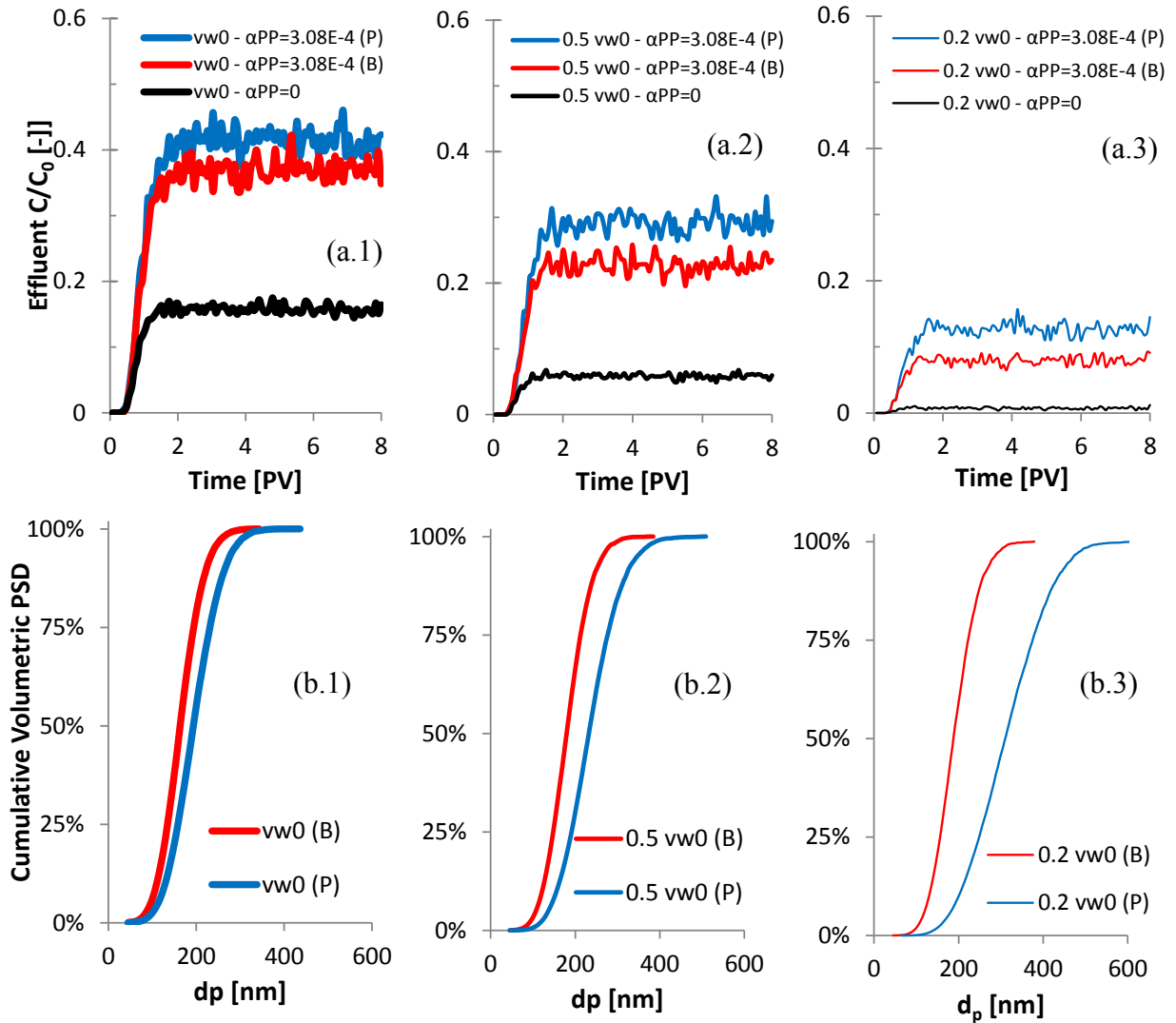


Figure 4-5. Influence of pore water velocity on (a) effluent NP concentration for aggregating (in red and blue) and non-aggregating (in black) particles, (b) predicted cumulative volumetric PSD curves for effluent NPs. Here, aggregation occurs only inside the column (i.e. $\alpha_{PP} = 0$ at the column inlet boundary and $\alpha_{PP} = 3.08 \times 10^{-4}$ inside the column).

4.4.2.2. Sensitivity to Particle Concentration

A decrease in the influent particle concentration ($C_{w,0}^{NP}$) from 725 mg/L to 72.5 mg/L reduced the extent of aggregation-induced enhancement of NP elution from ca. 290% to 170% (Comparison of red and black lines in Figure 4.6 (a.1)). The enhanced mobility of particles at a higher influent concentration is also illustrated by the predicted NP retention profiles (Figure 4.6 (a.2)). The reduction in influent concentration reduced the average diameter of effluent particles from ca. 230 to 100 nm (Figure 4.6 (a.3)). This is consistent with the second-order dependence of aggregation kinetics on the number concentration of NPs. Note that a filtration-only model cannot capture any changes in the dimensionless effluent concentration (i.e. $\frac{C}{C_0}$) as a consequence of changes in the influent concentration.

4.4.2.3. Sensitivity to Aggregation Efficiency

Aggregation efficiency (α_{pp}) depends on particle surface and solution chemistry and can vary based on particle coating, solution pH and/or ionic strength. The influence of aggregation efficiency on PP and PC interactions was explored over a two orders-of-magnitude range from 3.08×10^{-5} to 3.08×10^{-3} . A one order-of-magnitude decrease/increase in the aggregation efficiency (from that of the original scenario, i.e. 3.08×10^{-4}) was associated with a ca. 39%/22% decrease/increase in the level of aggregation-induced enhancement of NP elution that was predicted for the base case (Figure 4.6 (b.1)). The predicted average effluent particle diameter was ca. 100 nm with $\alpha_{pp} = 3.08 \times 10^{-5}$ and 610 nm with $\alpha_{pp} = 3.08 \times 10^{-3}$ compared to ca. 230 nm estimated for $\alpha_{pp} = 3.08 \times 10^{-4}$ (Figure 4.6 (b.3)). The rate of growth of cluster ranks increases linearly with α_{pp} . NP retention, however, is a function of collision efficiency (η_0) which has a non-linear dependence on cluster diameters, which is in turn, a function of cluster rank and fractal dimension.

Simulations based on α_{PP} values 3.08×10^{-4} and 3.08×10^{-3} predict similar effluent NP concentrations after ca. 7 PV (4.5 (b.1)). The explanation, once again, lies in the non-linear nature of the relationship between η_0 and d_p . As illustrated by Figure 4.4 (c), there is a limit to the extent of enhancement of NP mobility by the aggregation process. The tendency of a particle for deposition was estimated (Eq. 3.5) to be at its minimum ($\eta_0 = 0.018$) for a d_p of ca. 400 nm. The predicted average effluent particle diameters for α_{PP} values of 3.08×10^{-4} and 3.08×10^{-3} are ca. 230 and 610 nm after 8 PV (Figure 4.6 (b.3)) for which the corresponding η_0 -values, respectively, are ca. 0.0219 and 0.0209. This similarity in the average collision efficiency, despite of the contrast between aggregation efficiency values, rationalizes the similar effluent concentrations between ca. 7 to 8 PV.

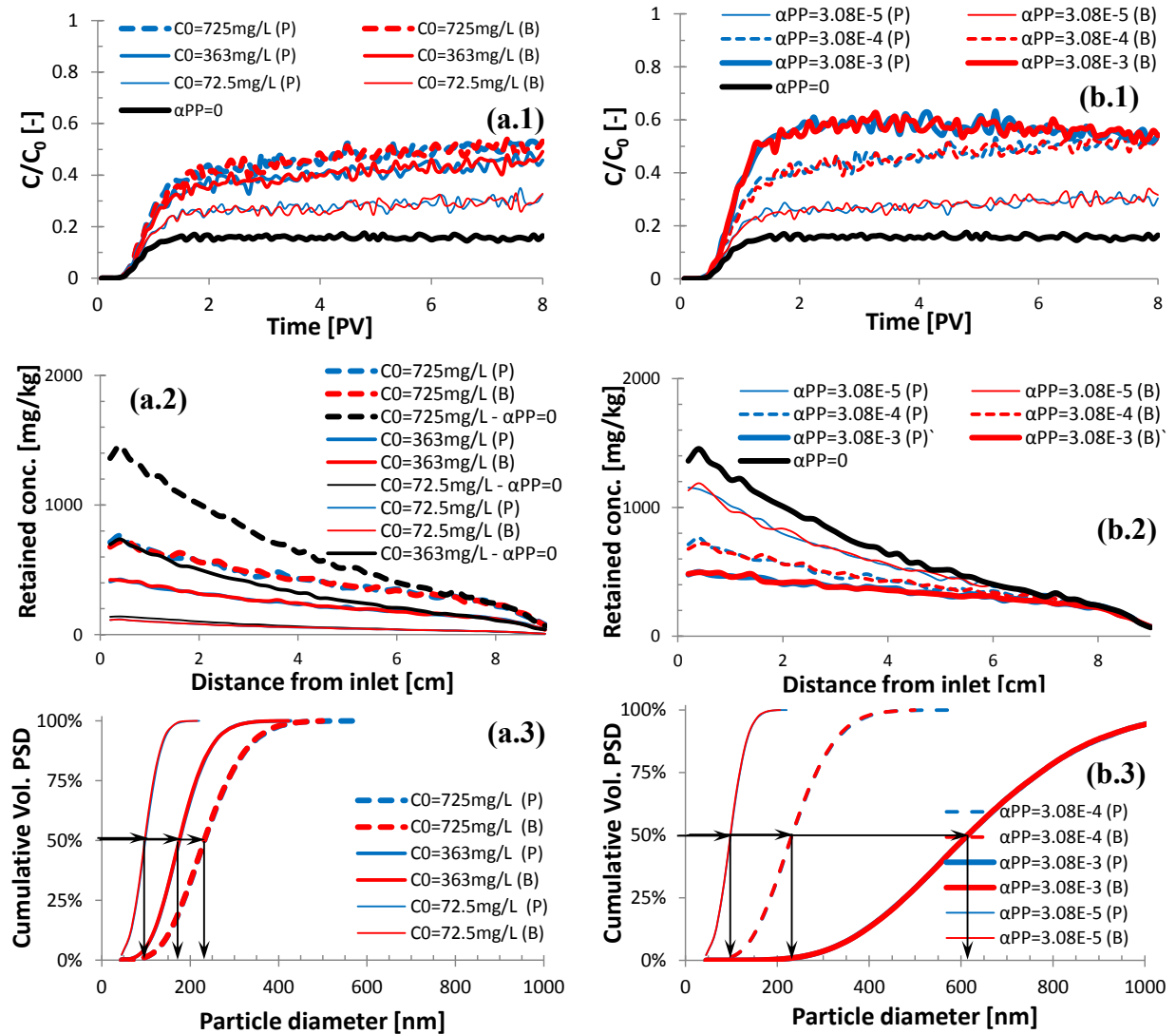


Figure 4-6. Influence of (a) influent NP concentration and (b) aggregation efficiency on predicted (1) effluent NP concentrations, (2) spatial distribution of retained NPs, and (3) cumulative volumetric PSD curves of effluent NPs.

4.4.2.4. Sensitivity to Primary Particle Size

Primary particles ($d_{P(i=1)}$) are the constructing units of larger clusters. The size of primary particle can be influenced by a number of factors including the method of production, solution and particle surface chemistry. While some NPs like nanosilver can be as small as ca. 10 nm [114], others such as nZVI fall in the range of hundreds of nanometers [13]. Thus for this sensitivity analysis, the primary particle diameter was varied over a one order-of-magnitude range, from 10 to 100 nm while the influent NP

concentration remained constant. To better demonstrate the potential controlling effects of $d_{P(i=1)}$ on PP and PC interactions, an aggregation efficiency of 3.08×10^{-5} was considered in all simulations, which is one order-of-magnitude lower than that used in the base case.

Decreasing $d_{P(i=1)}$ from 45 to 10 nm increased η_0 from ca. 0.075 to ca. 0.24 (due to the enhancement of Brownian motion), resulting in a significant increase in the retention of non-aggregating particles and decreasing NP elution from 14.3% to 0.6% of the total injected NP mass (Figure 4.7 (a)). The reduction in $d_{P(i=1)}$ accelerated the aggregation process by increasing the number concentration of primary particles (i.e. $n_{(i=1)}$) 90 fold. This increased number concentration resulted in an increase in the mean diameter of effluent particles from ca. 100 nm to ca. 145 nm (Figure 4.7 (b)) thereby enhancing their overall mobility, as η_0 decreased from ca. 0.042 to ca. 0.030 (Figure 4.7 (c)). The predicted NP elution thus increased from 25.0% to 35.1%. A reduction in NP size has a dual effect on the transport of NPs. It increases the frequency of PC collisions by increasing the magnitude of Brownian diffusion thereby decreasing the NP mobility. At the same time, the reduction in primary particle size, also promotes the aggregation process through a third-order increase in the number of particles. An enhancement of aggregation implies an increase in the level of aggregation-induced enhancement of NP mobility in the nanometer range.

On the other hand, increasing $d_{P(i=1)}$ from 45 to 100 nm decreased the collision efficiency from 0.075 to 0.039 which enhanced NP elution from 14.3% to 32.2% for non-aggregating particles. When $d_{P(i=1)}$ was increased to 100 nm, the extent of PP interactions was greatly reduced; more than 30% (by weight) of effluent NPs were primary particles and only a small fraction (i.e. < 3%) had a cluster size greater than 3.

The effect of aggregation on PC interactions, as a result, decreased markedly; the aggregation-induced enhancement of NP elution declined from ca. 75% to 9%.

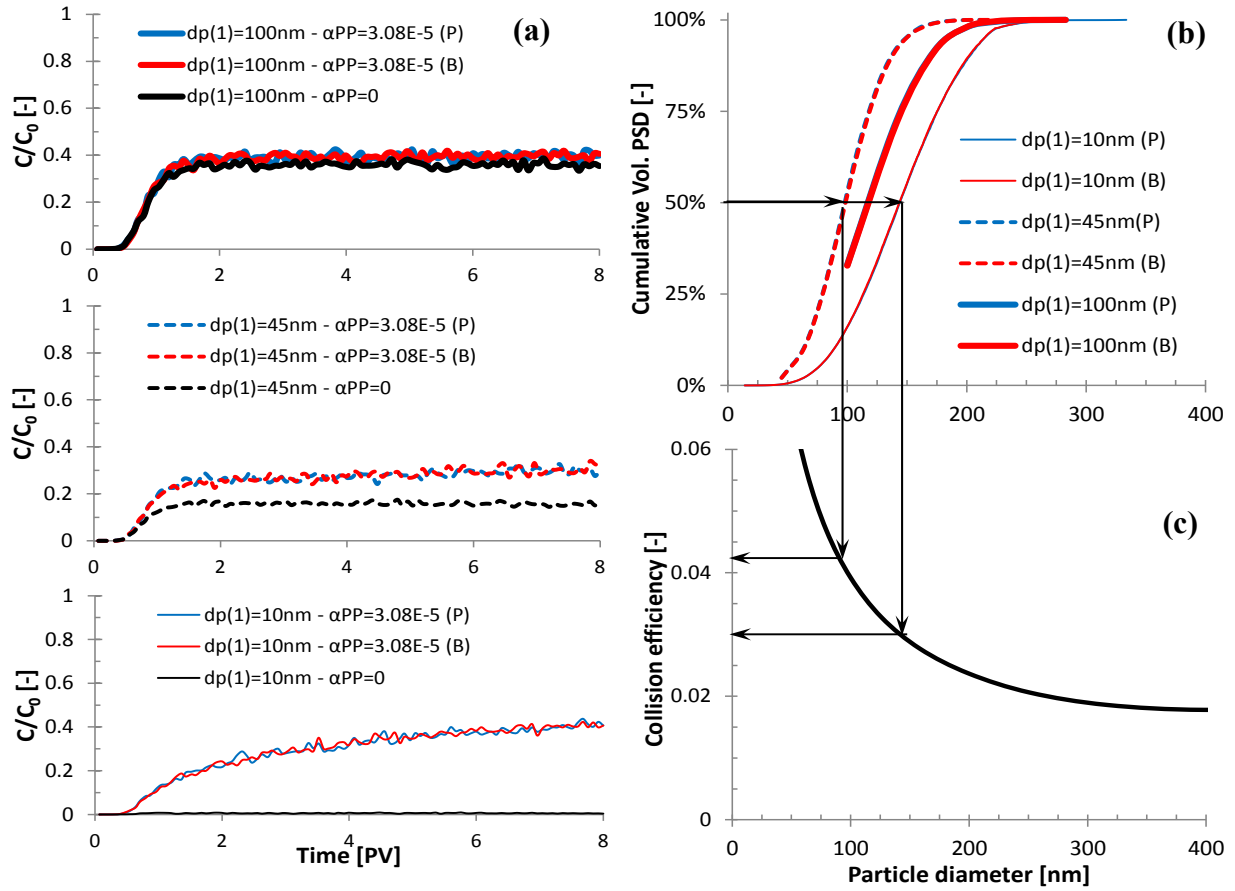


Figure 4-7. Influence of primary particle size on (a) effluent NP concentration for aggregating (in red) and non-aggregating (in black) particles, (b) predicted cumulative volumetric PSD curves for effluent NPs, and (c) collision efficiency – particle diameter relationship.

4.5. Conclusions

In the nanometer scale, Brownian diffusion is typically considered the predominant mechanism for particle-collector collisions. An increase in the hydrodynamic diameter of NPs due to aggregation, however, can potentially suppress this dominance by stimulating drag and gravity forces acting on particle clusters moving toward collector surfaces. Despite their potential influence, aggregation processes have

not generally been included in conventional models for colloidal transport. Provided that the system physicochemical characteristics promote the PP interactions, the insensitivity of conventional models to spatiotemporal changes in particle sizes, will not allow for an appropriate description of the retention and transport behavior of NPs in porous media. According to the existing literature on the colloidal transport in aquatic systems, however, changes in the size of colloidal particles can potentially either enhance or reduce the extent of PC interactions.

In this chapter, a Lagrangian framework was developed and implemented in a RWPT simulator to model nanoparticle aggregation. This model, HELP-1D, offers some advantages as well as a number of limitations over existing models. The main advantages include (1) capability of modeling polyadic collisions as opposed to binary collisions associated with Eulerian models, (2) a rigorous satisfaction of global mass conservation, and (3) calculation, instead of pre-selection, of the maximum cluster size. Well-known disadvantages associated with the Lagrangian approach include: (1) a sensitivity of numerical precision and accuracy to the number of modeled particles, potentially resulting in computationally expensive simulations (2) solutions which exhibit random fluctuations that inhibit applicability to inverse problems.

HELP-1D reproduced the numerical results of an existing Eulerian coupled aggregation-transport model. Neither models, yet, fully described the reported experimental observations of CMC-nZVI retention and transport in water-saturated sand columns [123]. Hypothetically, a combination of either (1) NP aggregation and site-blocking or (2) aggregation and detachment processes can provide a better fit to the experimental data. The verification of these hypotheses, however, is subject to further experimental evidence and numerical analysis.

Result of subsequent sensitivity analyses identified influent NP concentration, primary particle size and pore water velocity as key factors influencing particle-particle interactions, thereby affecting the retention and transport characteristics of NPs (i.e. particle-collector interactions). For similar mass concentration, increasing primary particle size reduces the number concentration of particles, thus, decelerating the aggregation process, while a reduction in flow velocity intensifies the aggregation effects by increasing the residence time of particles in the system.

Chapter 5 MODELING NP-OIL/WATER INTERFACE INTERACTIONS

5.1. Introduction

The significance of the interactions of NPs with an oil/water interface (o/w IF) lies in the application of nanosensors in determining the geolocation and composition of gas and oil reservoirs. Studies of capillary interactions have shown that colloidal particles with a broad range of moderately hydrophobic coatings [50] tend to localize at high energy oil/water interfaces [49]. To date, only a few studies have directly addressed the fate and transport of NPs in porous media containing a secondary non-aqueous phase [13, 50, 51]. To the best of the writer's knowledge, thus far, the only modeling attempt has been by *Bishop et al.* [50]. They used a collision efficiency term based on clean-bed filtration theory to simulate ZVI retention profiles in sand columns containing dichlorobenzene residuals. The shortcoming of this approach is in the presumption of unlimited retention capacity of particles on the o/w IF. Engineered NPs are often designed, however, to form stable aqueous suspensions. Thus, their affinity for the aqueous phase suggests that their unlimited accumulation at the hydrophobic water/NAPL interface is unlikely. This assumption has also been contradicted by numerous observations of limited enhancement of particle retention in NAPL containing systems (see Subsection 1.2.4 for more information).

To facilitate a more realistic mathematical representation of NP-o/w IF interactions, in this study, a surface excess model was developed based on Gibb's equation. The Gibbs model is employed to describe the non-linear isotherm representing the accumulation of interfacial tracers (which do not partition into the non-aqueous phase) at fluid-fluid interfaces [128]. The effect of coexisting surface active agents on NP-o/w IF interactions was included in the mathematical model. Surfactants, if present, may interact with NPs and/or porous media to alter the transport behavior of NPs [126]. Also, their presence can facilitate the dissolution rate of oil residuals [129] thereby reducing the interfacial area to which NPs attach. Surfactants can be co-injected with NPs to enhance or reduce NP mobility, or can be present as unintentional residuals from the particle synthesis/coating process (e.g., free polyacrylamide (PAA) in aqueous suspension of PAA-coated quantum-dot NPs [126]).

Rosen [130] is the main reference used here for deriving the mathematical expressions for NP and surfactant-o/w IF interactions. According to Gibb's equation, in a two component system (i.e. one-solvent (1) one-adsorbate (2)), equilibrium adsorption from dilute solutions (where the activity coefficient approaches unity) can be estimated from interfacial tension measurements via the following expression:

$$\Gamma_2^1 = -\frac{c}{RT} \left(\frac{d\gamma}{dc} \right)_T = -\frac{1}{RT} \left(\frac{d\gamma}{d \ln c} \right)_T \quad (5.1)$$

Here Γ_2^1 [mmol/m²] is the surface excess of component 2 (i.e. the adsorbate) where the mathematical surface is arbitrarily placed to make the surface excess of component 1 (i.e. the solvent – water) $\Gamma_1 = 0$; c [mol/L] denotes the bulk phase concentration of adsorbate; and γ [mN/m] is the surface tension. R [8.31 J mol⁻¹ K⁻¹] and T [K] are the universal gas constant and ambient temperature, respectively. Note that two portions of the aqueous

solution comprise the interfacial region. One is from the surface region and the other from the bulk solution. “The number of moles of solute in the sample from the surface minus the number of moles of solute in the sample from the bulk give the **surface excess** number of moles of solute” [131]. This quantity divided by the area of the surface equals Γ_2^1 . This form of Gibbs equation states that the slope of a plot of γ versus the logarithm of concentration (or activity if the solution is non-ideal) is a measure of the surface excess of the solute [131].

For surface-active solutes, Γ_2^1 can be considered to be equal to the actual surface concentration without significant error [130]. This approximation was accepted in this work, because the calculation of actual surface concentrations requires an estimation of the interfacial layer thickness. Currently, there is no technology to measure the thickness of the interfacial layer. However, the interfacial tension measurements may be readily available.

Figure 5.1, borrowed from Hiemenz and Rajagopalan [131], shows the typical $\gamma - c$ curves for organic (curve 1), ionic inorganic (curve 2), and amphiphilic (curve 3) solutes. All three of these curves correspond to relatively dilute solutions. At higher concentrations effects other than adsorption may lead to departures from these basic forms [131]. The break in curve 3, typical of soluble amphipathic species, is understood to indicate the threshold of micelle formation, known as the critical micelle concentration (CMC). Above the CMC the surface tension of the solution remains constant, since only the monomeric form contributes to the reduction of interfacial tension. For concentrations below but near the CMC the slope of the $\gamma - c$ curve is constant, indicating that the surface concentration has reached a constant maximum value [130]. In this range the interface is considered to be saturated with surfactant and the continued reduction in

interfacial tension is due mainly to the increased activity of the surfactant in the bulk phase region of the interface rather than at the surface region [130].

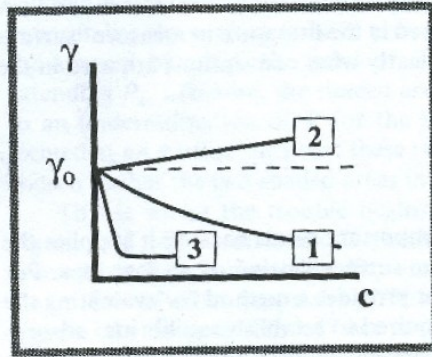


Figure 5-1. Three types of variation of γ with c for aqueous solutions: (1) simple organic solutions, (2) simple electrolytes, and (3) amphiphathic solutes (Fig. 7-14) [131].

5.2. Mathematical Model

The partitioning of NPs from the o/w IF into the oil phase was considered negligible in this study consistent with reports outlined in Subsection 1.2.4. Two liquid phases are considered: (1) a mobile aqueous phase, and (2) an immobile residual organic liquid phase. Two types of capture sites exist that allow for the attachment/adsorption of NPs/surfactant molecules; surface sites on (1) the solid sand grains and (2) the o/w IF. Two possibilities are considered for simultaneous NP/surfactant interactions with the o/w IF: (1) independent (non-competitive) interactions where each component interacts with interfacial sites that are specific to that component, and (2) competition-based interactions where NPs and the surfactant interact with the same capture sites on the o/w IF. The residual oil can dissolve in the aqueous phase at limited-rate which can be influenced by surfactants. Figure 5.2 illustrates a schematic of the described conceptual model.

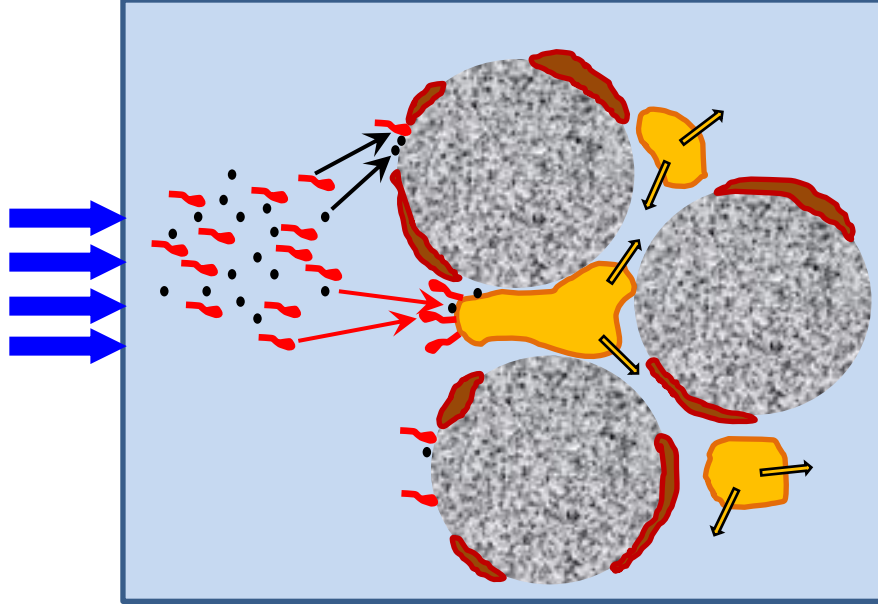


Figure 5-2. A schematic of the NP and surfactant transport and interactions with the solid phase and o/w IF and interphase mass transfer (i.e. solubilization of the organic liquid phase in the aqueous phase).

5.2.1. Phase Mass Balance Equations

A multiphase extension of Darcy's equation was implemented to represent aqueous and oil phase mass balance [90]:

$$\frac{\partial}{\partial t} (\varphi \hat{\rho}_w S_w) = \frac{\partial}{\partial x} \left[\hat{\rho}_w \lambda_w \left(\frac{\partial P_w}{\partial x} - \hat{\rho}_w \bar{g}_x \right) \right] + \varphi E_{wn_o}^* \quad (5.2)$$

where φ [-] is the porosity, $\hat{\rho}_w$ [g/m³] is the density of the aqueous phase, S_w [-] is the saturation of the aqueous phase, \bar{g}_x (m/s²) is the component of gravitational acceleration vector in the x -direction, and λ_w [m³ s/g] is the mobility of the aqueous phase ($\lambda_w = k \frac{k_{rw}}{\mu_w}$), where k [m²] is the intrinsic permeability of the medium, k_{rw} [-] denotes the relative permeability of the aqueous phase, and μ_w [g/m s] is the aqueous phase dynamic viscosity. $E_{wn_o}^*$ [g/m³ s] is the rate of interphase mass transfer (i.e. dissolution) to the aqueous phase, w , from the non-aqueous phase, n , per unit pore volume. The surfactant-

enhanced solubilization model of *Abriola et al.* [132] was implemented for modeling rate-limited dissolution of oil residuals. Mass balance for the immobile oil phase can be written as:

$$\frac{\partial}{\partial t}(\varphi \hat{\rho}_n S_n) = -\varphi E_{wno}^* = -\varphi k_{eff}(C_o^{sol}(C_{surf}^w) - C_o^w) \quad (5.3)$$

where S_n [-] and $\hat{\rho}_n$ [kg/m³] are oil phase saturations and density, respectively. k_{eff} [1/s] is a lumped or “effective” mass transfer coefficient ($k_{eff} = k_f a_0$), where k_f [m/s] is a film mass transfer coefficient across the boundary layer, and a_0 [m²/m³] is the specific surface area of the interface. *Abriola et al.* [132] proposed the following functional form for k_{eff} considering a quasi-steady-state diffusion-limited mass-transfer process:

$$k_{eff} = a_1 \cdot q_w^{a_2} + \hat{k}_0 \quad (5.4)$$

where q_w [m/s] is the Darcy velocity, and a_1 [s^{b-1}/m^b] and a_2 [-] are empirical constants and \hat{k}_0 [1/s] is the value of k_{eff} under no flow condition. C_o^{sol} [mM] and C_o^w [mM], in Eq. 5.3, are the equilibrium solubility and bulk aqueous concentrations of dissolved oil, respectively. C_o^{sol} can be expressed as a function of the aqueous phase concentration of the surfactant species, C_{surf}^w [132]:

$$C_o^{sol} = C_o^{sol}(C_{surf}^w = 0) + a_3 \cdot C_{surf}^w \quad (5.5)$$

where $C_o^{sol}(C_{surf}^w = 0)$ [mM] and a_3 [-] are system specific empirical parameters that must be experimentally determined for different oil and surfactant systems.

5.2.2. Component Mass Balance Equations

The multiphase extension of the transport equation used by *Abriola et al.* [90] was modified to include a mass accumulation term for sites on the o/w IF:

$$\frac{\partial}{\partial t} (\varphi S_w C_c^w + \rho_b \omega_c^s + \varphi S_n \omega_c^{if}) + \frac{\partial}{\partial x} \left[\varphi S_w \left(C_c^w v_w - D_{w_c}^h \frac{\partial C_c^w}{\partial x} \right) \right] = \varphi E_{wn_c} \quad (5.6)$$

here, c represents the nanoparticles (NP) and dissolved constituents (i.e. dissolved oil and the surfactant), C_c^w [mmol/L water], ω_c^s [mmol/kg dry soil], and ω_c^{if} [mmol/L oil] denote the aqueous phase, solid phase, and interfacial concentrations of component c . ρ_b [kg/m³] is the bulk density of sand, v_w [m/s] is the pore water velocity, and $D_{w_c}^h$ [m²/s] is the hydrodynamic dispersion coefficient of component c in the aqueous phase. For $c = o$, E_{wn_o} [mmol/L s] is the mass transfer rate between aqueous and oil phases per unit pore volume. Based on their hypophilic-lypophilic balance (HLB), some surfactants act as interfacial tracers (considered in this study) that only accumulate at the o/w IF but do not partition into the organic phase [128] (i.e. $E_{wn_{surf}} = 0$). Colloidal particles with a broad range of moderately hydrophobic coatings are expected to adhere spontaneously to the interface [50], therefore NP partitioning into the organic liquid phase was considered negligible (i.e. $E_{wn_{NP}} = 0$).

5.2.2.1. Capture by Solid Phase Sites

A multi-constituent site blocking (MCB) model proposed by *Becker et al.* [126] was implemented for modeling NPs and surfactant capture by the solid phase. The MCB model is a modified version of modified filtration theory (MFT) that incorporates a competitive one-site scheme for attachment/adsorption of NPs/surfactants. According to the MCB model rate-limited capture by solid phase is expressed as:

$$\frac{\partial}{\partial t} (\rho_b \omega_c^s) = \varphi S_w k_c^s \psi^s C_c^w \quad (5.7)$$

$$\psi^s = 1 - \sum_c \frac{\omega_c^s}{\omega_c^{s,max}} \quad (5.8)$$

in which Ψ^s [-] is the site-blocking function, and $\omega_c^{s,max}$ [mmol/kg soil] is the maximum retention capacity for component c by solid surfaces in the absence of all other components. k_{surf}^s [1/s] and k_{NP}^s [1/s] are first-order rate constants for surfactant adsorption and NP attachment, respectively. k_{NP}^s can be estimated from *Yao et al.* [25] formulation:

$$k_{NP}^s = \frac{3}{2d_c}(1 - \varphi)V_w \alpha_s \eta_s \quad (5.9)$$

where d_c [m] is the collector diameter, η_s [-], the collision contact efficiency of particles with collector surfaces, that is calculated from *Tufenkji and Elimelech's* correlation (Eq. 3.5) [24]. α_s [-], the attachment efficiency, is a function of chemical properties of the system.

5.2.2.2. Capture by Interfacial Sites

The MCB model [126] was modified and implemented to model NP and surfactant o/w IF interactions. Note that the developed mathematical model is only applicable to systems where surfactants compete with NPs for the interfacial sites. The component mass transfer to the o/w IF is expressed as:

$$\frac{\partial}{\partial t}(\phi S_n \omega_c^{if}) = \phi S_w k_c^{if} \Psi^{if} C_c^w \quad (5.10)$$

$$\Psi^{if} = 1 - SSA_n^{-1} \cdot \sum_c \frac{\omega_c^{if}}{\Gamma_c^{eq}(C_c^w)} \quad (5.11)$$

where k_{surf}^{if} [1/s] and k_{NP}^{if} [1/s] are rate constants for surfactant adsorption and NP attachment to the o/w IF. Γ_c^{eq} [mmol/m² of IF] is the Gibbs surface excess of component c on the o/w IF. Γ_c^{eq} , as explained in Subsection 5.1, is the equilibrium-state capacity of the interface for the association of component c , and thus, considered analogous to $\omega_c^{s,max}$ in Eq. 5.8. There is a difference, however, between Γ_c^{eq} and $\omega_c^{s,max}$. Unlike the

constant solid phase retention capacity, the Gibbs surface excess varies with bulk aqueous concentration surface active species as described by Eq. 5.1.

SSA_n [m² of IF/m³ oil], in Eq. 5.11, is the effective specific surface area of oil phase residuals expressed as a function of oil phase saturation:

$$SSA_n = \frac{6 \cdot f}{d_b^{init} S_n^{init}} \left(\frac{S_n}{S_n^{init}} \right)^{-1/3} \quad (5.12)$$

where d_b^{init} [m] and S_n^{init} [-] are the initial representative diameter of spherical oil blobs and initial organic liquid phase saturation, respectively, and f [-] denotes a fraction of o/w IF that is in contact with mobile aqueous phase [132]. The adsorption rate constant of surfactant molecules, k_{surf}^{if} in Eq. 5.10, was assumed directly proportional to the surface area of the o/w IF [133], which in turn is a function of oil phase saturation, and was expressed as:

$$k_{surf}^{if} = k_{surf\,init}^{if} \left(\frac{S_n}{S_n^{init}} \right)^{2/3} \quad (5.13)$$

in which $k_{surf\,init}^{if}$ [1/s] is the adsorption rate constant when the oil phase is at its maximum saturation, S_n^{init} [-] at time $t = 0$.

In order to represent the attachment of NPs to the o/w IF, the following expression was derived from Eq. 5.9 that describes attachment to the solid phase:

$$k_{NP}^{if} = \frac{3}{2d_b^{init} \left(\frac{S_n}{S_n^{init}} \right)^{1/3}} (\varphi S_n) V_w \alpha_{if} \eta_{if} \quad (5.14 \text{ (a)})$$

Here $(1 - \varphi)$, the volume of solid phase per unit volume of porous medium, in Eq. 5.9 was replaced with the volumetric content of the oil phase, $\theta_n = \varphi S_n$, and d_c , the constant representative diameter of sand grains, in Eq. 5.9 was replaced with the variable

oil blob diameter, $d_b = d_b^{init} \left(\frac{S_n}{S_n^{init}} \right)^{1/3}$. α_{if} [-] and η_{if} [-] are interfacial attachment and collision contact efficiencies. The latter efficiency can be estimated from the correlation of *Tufenkji and Elimelech* (i.e. Eq. 3.5) [24] assuming that o/w IF behaves similar to a solid surface in terms of collisions with approaching NPs, consistent with the approach taken by *Bishop et al.* [50]. Simplifying the terms of Eq. 5.14 (a) yields:

$$k_{att,if}^{nP} = \frac{3}{2} \frac{\varphi}{d_b^{init}} S_n^{init^{1/3}} S_n^{2/3} V_w \alpha_{if} \eta_{if} \quad (5.14 \text{ (b)})$$

Note that in the proposed approach, the mass accumulation on the o/w IF is assumed to be an irreversible process. If later experimental evidence suggests otherwise, Eq. 5.10 must be modified to include surfactant desorption and NP detachment. This can be done by either (1) implementing a linear driving force approach or (2) adding desorption/detachment terms that are first-order with respect to ω_c^{if} concentrations.

5.3. Numerical Implementation

Two hybrid numerical modules were added to HELP-1D for modeling NP (Lagrangian) and surfactant (Eulerian) interactions with the solid phase (module 1) and the o/w IF (module 2). The component transport equation (i.e. Eq. 5.6) is solved using (a) the Crank-Nicolson discretization method for dissolved oil and the surfactant, and (b) the Lagrangian RWPT method for NPs. The expressions for the adsorption of solute components to the solid phase (Eq. 5.7) and to the interfacial sites (Eq. 5.10) are solved using an explicit discretization approach with a time lag for calculating the adsorbed phase concentrations. That is, in each round of computations, the ω_c^s -values from time level k , are used to calculate C_c^w at time level $k + 1$ (solving Eq. 5.6), from which ω_c^s - values are subsequently calculated with a time lag for time level $k + 1$ (Eq. 5.7). The

same discretization method is employed for adsorption of solute components to the o/w IF (i.e. Eq. 5.10).

Numerical implementation of Eqs. 5.7 and 5.10 in the Lagrangian module of HELP-1D was accomplished by (i) calculating probability values during time interval Δt for the two cases of NP attachment to (1) the solid phase and to (2) the o/w IF, (ii) selecting a random chance for each modeled particle and for each case from a uniform distribution between 0 to 1, and (iii) labeling particles whose attachment probability exceeds the random chance as “attached” to either the (1) solid phase or (2) o/w IF, following the procedure described in Subsection 3.3.3. Probability functions for NP attachment to capture sites on solid, $P_{att_p}^s$ [-] and interfacial, $P_{att_p}^{if}$ [-], surfaces were derived by rearranging the terms of Eqs. 5.7 and 5.10, respectively:

$$P_{att_p}^s = -\frac{dC_{NP}^s}{C_{NP}^s} = k_{NP}^s \Psi^s \Delta t = \frac{3}{2d_c} (1 - \varphi S_w) V_w \alpha_s \eta_s \Psi^s (\omega_c^s) \Delta t \quad (5.15)$$

$$P_{att_p}^{if} = -\frac{dC_{NP}^{if}}{C_{NP}^{if}} = k_{NP}^{if} \Psi^{if} \Delta t = \frac{3}{2} \frac{\varphi}{d_b^{init}} S_n^{init^{1/3}} S_n^{2/3} V_w \alpha_{if} \eta_{if} \Psi^{if} (\omega_c^{if}) \Delta t \quad (5.16)$$

where dC_{NP}^s [mM] and dC_{NP}^{if} [mM] refer to changes in the aqueous concentration of NPs due to NP mass exchange with the solid phase and the o/w IF, respectively, during time increment Δt .

5.3.1. Model Verification

The accuracy of the numerical solution of module 1 (i.e. interactions with the solid phase) was verified by comparing HELP-1D results of with those from the MCB model [126] for a generic case scenario, where two concurrent 3 pore volume pulses of quantum-dot NPs and PAA surfactant were injected into a 10.8 cm long water-saturated

sand column under conditions similar to the quantum-dot transport column experiments presented in *Becker et al.* [126]. HELP-1D successfully reproduced both the effluent (Figure 5.3 (a)) and retained (Figure 5.3 (b)) concentrations of NPs and the surfactant obtained from the MCB model. The second numerical module (i.e. interactions o/w IF) could not be independently verified because no appropriate analytical solutions or numerical simulators exist.

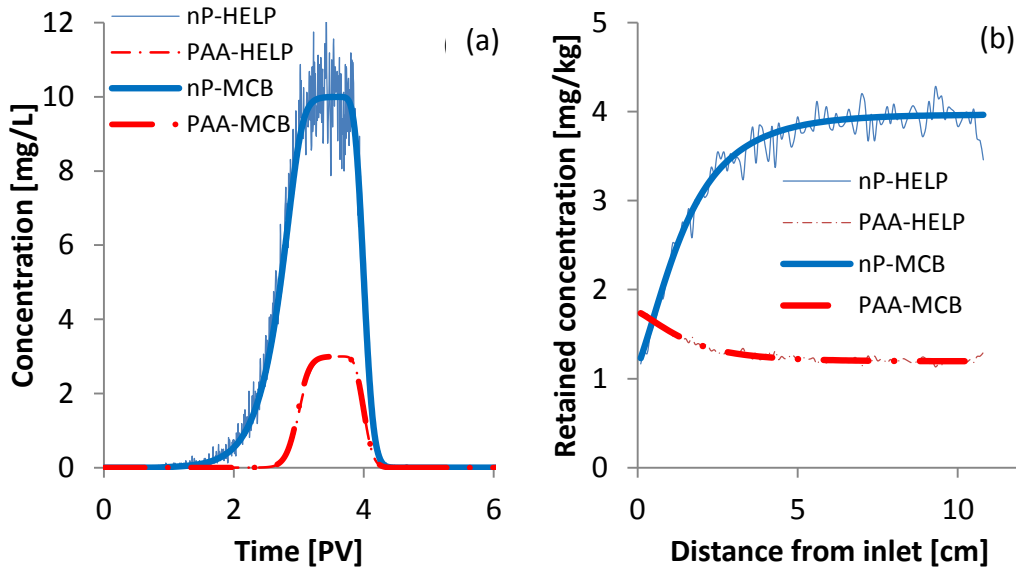


Figure 5-3. Comparative NP and surfactant (a) BTCs and (b) solid phase retention profiles simulated by HELP-1D and MCB models [126] for simultaneous injection of a 3 pore volume pulse of 10 mg/L of quantum-dot particles and 3 mg/L of PAA.

5.4. Results and Discussion

5.4.1. The Hypothetical Scenario

The validation of the proposed model is not currently possible due to a lack of pertinent experimental data. However, the capability of HELP-1D, as a mathematical tool, for simulating the interactions of NPs and surfactants with the o/w IF is demonstrated in this section. For the **simplicity of the interpretation** of the simulation results presented in this subsection, NP and surfactant **interactions with the solid phase**

are neglected. A hypothetical scenario for simultaneous transport of NPs and surfactant in a porous medium containing a residual oil-phase was created, and model input parameters were selected in accordance with the documented values in the colloidal transport in porous media literature (Table 5.1).

Table 5-1. List of model input parameters used in the simulation of the generic case scenario.

Property	Symbol	Unit	Value	Reference
Column length	L_c	cm	10.8	[126]
Porosity	ϕ	-	0.367	[126]
Pore velocity	v_w	m/day	7.6	[126]
Sand median diameter	d_c	μm	354	[91]
Initial mean blob diameter	d_b^{init}	μm	440	[132]
Initial NAPL saturation	S_n^{init}	-	0.2	[132]
o/w IF surface area factor	f	-	0.8	[132]
Particle diameter	d_p	nm	10.3	[134]
NP - IF attachment efficiency	α_{if}	-	0.13	Hypothetical [50]
Hamaker constant of oil	A_{33}	10^{-20} J	84	[135]
Hamaker constant of Fe_2O_3 in water	A_{121}	10^{-20} J	5.4	[18]
Initial Calfax IF ads. const.	$k_{surf}^{if init}$	1/s	1×10^{-3}	Hypothetical IFT-data
Oil (dodecane) solubility	$C_o^{sol}(C_{surf}^w = 0)$	mg/L	3.7×10^{-3}	[132]
Lumped mass transfer coefficient	k_{eff}	1/s	1.42×10^{-3}	Calculated [132]
Oil dissolution parameter (Eq. 5.5)	a_3	-	8.11×10^{-2}	[132]

The Gibbs surface excess values were calculated from two separate sets of interfacial tension measurements for magnetite NPs (nMag) (0-500 mg/L) and Calfax 16L-35 surfactant (0-1000 mg/L) in contact with IsoparI oil/water interface (Figure 5.4). The experimental data used here were provided by Prof. Pennell's research group (Dr. Wang Y.). A second-order polynomial function was fitted to nMag $\gamma - c$ data (Figure 5.4 (b)). Calfax data were fit with a sigmoidal function of the following form:

$$\gamma(\ln C) = a_1 - \frac{a_2}{1 + \exp[-a_3(\ln C - a_4)]} \quad (5.17)$$

where a_i ($i = 1, \dots, 4$) coefficients are fitting parameters. a_1 and a_2 are related to surface tensions measured at the lowest (γ_0) and highest (γ_f) bulk concentrations of Calfax surfactant, a_3 is a measure of the steepness of $\gamma - \ln c$ curve, and a_4 is related to the concentration (C_M) at which Γ reaches its maximum. Table 5.2 discusses the physical meaning of a_i coefficients in more detail.

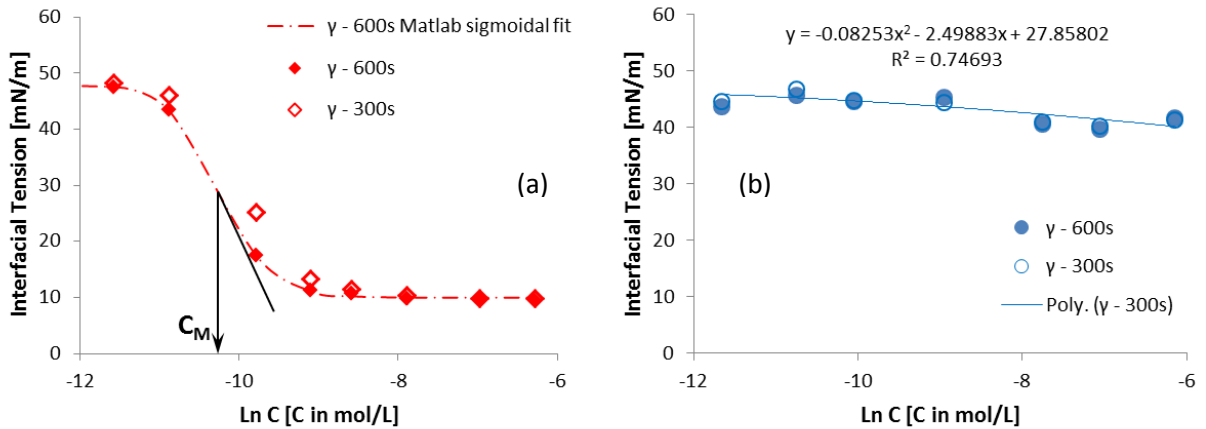


Figure 5-4. Experimental $\gamma - \ln c$ data measured at IsoparI oil/water interface for (a) Calfax 16L-32 surfactant (with a sigmoidal fit) and (b) magnetite NPs (with a 2nd-order polynomial fit).

Table 5-2. Interpretation of the physical meaning of the sigmoidal model parameters.

Fitting parameter	Fitted value	Physical meaning	Symbol	Value
a_1	48.19	IFT measured for lowest experimental concentration	γ_0	48.30
a_2	38.22	The difference between IFT measured for lowest and highest experimental concentrations.	$\gamma_0 - \gamma_f$	38.54
a_3	3.045	This parameter controls the slope of the steep part of $\gamma - c$ curve	λ	N/A
a_4	-10.25	The bulk concentration at which $\gamma - c$ curve has the highest slope corresponding to Γ_{max}	$\ln C_M$	N/A

The first derivative of the fitted functions was analytically evaluated, and used to estimate the component-specific Gibbs surface excess as a function of bulk aqueous

concentrations for Calfax surfactant and nMag (Eq. 5.1). Figure 5.5 (b) shows Γ values in a concentration range (0-40 mg/L), that is relevant to the hypothetical scenario and the subsequent sensitivity analysis. Note that, for the surfactant, Γ remains constant once Γ_{max} is reached at $C = C_M$.

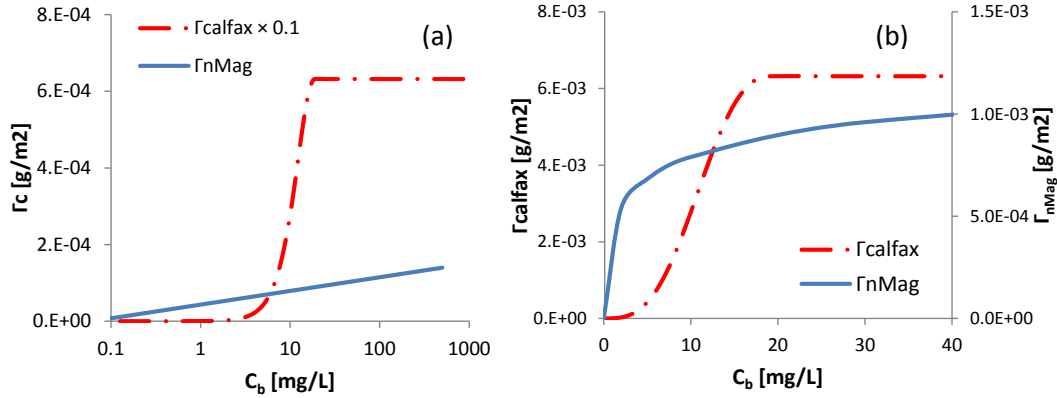


Figure 5-5. Surface excess – bulk phase concentration ($\Gamma - c$) curves in (a) logarithmic and (b) linear concentration scales derived from IFT data measured at Isoparl oil/water interface for Calfax 16L-35 surfactant and nMag.

To the best of the author's knowledge, no previous work supports the estimation of the kinetic interaction parameters with the o/w IF (i.e. $k_{surf_{init}}^{if}$ (Eq. 5.13) and α_{if} (Eq. 5.14 (b))). Therefore, hypothetical values were assigned to these parameters. The hypothetical value that was selected for $k_{surf_{init}}^{if} = 1 \times 10^{-3} s^{-1}$ (Table 5.1) is in the range of first-order rate constants ($2.3 \times 10^{-4} - 1.8 \times 10^{-3} 1/s$) that fit the temporal reduction in the interfacial tension (IFT) data measured at different bulk aqueous Calfax surfactant concentrations (10 – 200 mg/L) (Figure 5.6). The reduction in the IFT is recognized to be directly related to the number of moles of adsorbate on the IF. Therefore, the time rate of reduction of IFT can be related to the rate at which interfacial adsorption occurs.

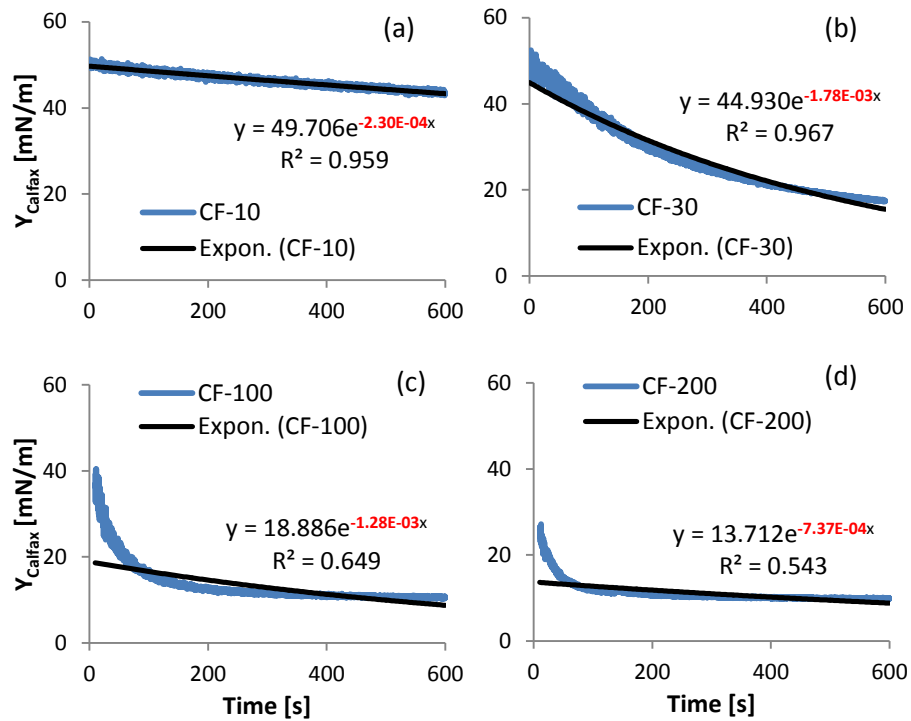


Figure 5-6. Interfacial tension measured over a 600 s time interval at IsoparI/water interface for Calfax 16L-35 surfactant at variable bulk aqueous concentrations of (a) 10, (b) 30, (c) 100, and (d) 200 mg/L.

5.4.1.1. nMag Transport in the Column in the Absence of Surfactants

The transport and capture of nMag by interfacial sites was explored over a 1-10 mg/L range of influent particle concentrations (C_0). A 3 aqueous (or 2.4 total) pore volume pulse of nMag was introduced to the column containing an initial residual oil saturation of 0.20 under conditions specified in Table 5.1. The column was then flushed with nMag-free background solution for up to 5 aqueous (or 4 total) pore volumes at a constant pore velocity of ca. 7.6 m/day.

At both of the simulated input nMag concentrations (i.e. 1 and 10 mg/L), HELP-1D predicted that o/w IF had little effect on nMag mobility. nMag BTCs resembled those of a non-reactive tracer (Figure 5.7 (a)) within the simulated range of influent concentrations. Only 3.4% of particles were retained at $C_0 = 1 \text{ mg/L}$, a value which

reduced to less than 0.9% when C_0 was increased to 10 mg/L. This minor level of NPs retention is consistent with minute reduction of IFT by nMag particles (Figure 5.4 (b)). Inspection of nMag retention profiles (Figure 5.8) revealed that regardless of the influent concentration, the interfacial sites reach their maximum capacity during the 2.4 PV pulse with an o/w IF attachment efficiency (α_{if}) of 0.13. At 10 mg/L, the saturation of interfacial sites occurred very fast as the pulse of particles migrates down gradient from the injection point (Figure 5.8 (b)). However, a kinetic effect can be seen at 1 mg/L both in the retention profiles up to 1.0 aqueous (or 0.8 total) pore volume (Figure 5.8 (a)) and nMag breakthrough from the column (Figure 5.7 (b)). The increase in the surface capacity of o/w IF with influent concentration of nMag is consistent Gibbs surface excess estimates (Figure 5.5).

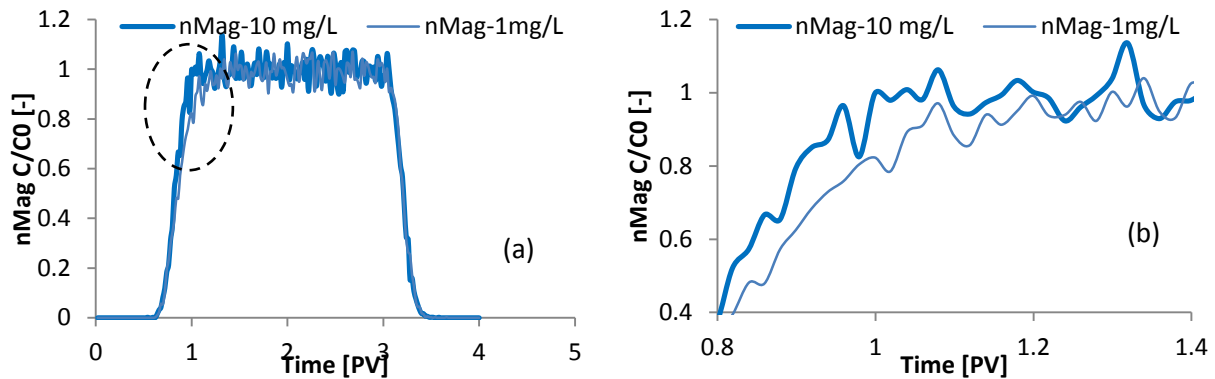


Figure 5-7. (a) Simulated effluent concentrations of nMag particles, and (b) effluent concentrations of nMag magnified for better visual illustration of the difference between NP breakthrough predicted for C_0 of 1 and 10 mg/L. Here, nMag interactions with solid phase are neglected.

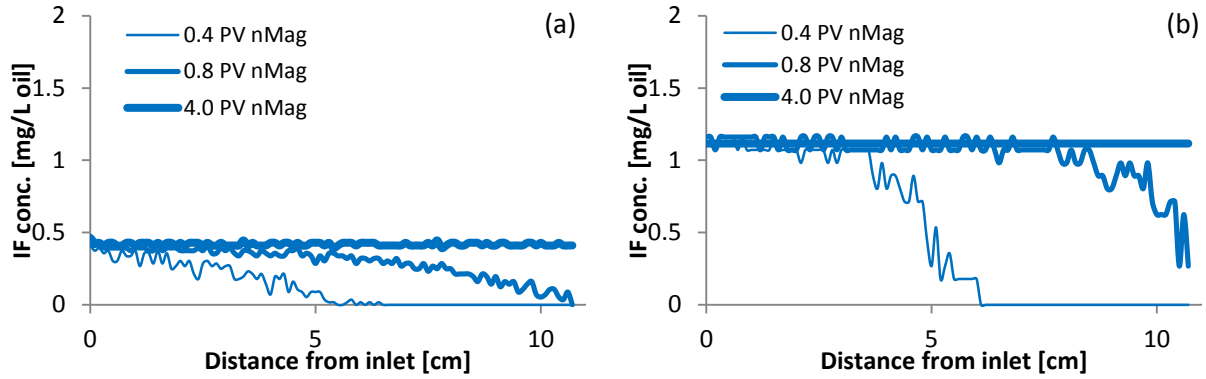


Figure 5-8. Simulated retention profiles of nMag particles captured by o/w IF at different simulation times corresponding to 0.5, 1.0 and 5.0 aqueous PVs for C_0 values of (a) 1 mg/L and (b) 10 mg/L. Here, nMag interactions with solid phase are neglected.

5.4.1.2. Surfactant Transport in the Column in the Absence of Particles

Transport and adsorption of Calfax 16L-35 surfactant in the absence of nMag particles was simulated at two different influent surfactant concentrations of 10 and 100 mg/L. Similar to the injection scenario described in Subsection 5.4.1.1, a 3 aqueous (2.4 total) pore volume pulse was introduced into the column, and then the column was flushed with 2 aqueous (1.6 total) pore volumes of surfactant-free water. The surface capacity of the o/w IF for Calfax was estimated from experimental $\gamma - c$ measurements (Figure 5.5). Table 5.1 shows the values assigned to other model input parameters.

Simulation results are shown in Figures 5.9 and 5.10. Increasing the input surfactant concentration (C_0) resulted in faster blocking of interfacial sites. For an input concentration of 100 mg/L, the normalized effluent concentration ($\frac{c}{C_0}$) approached unity, indicating full blockage of interfacial sites, after ca. 2 (total) pore volumes (Figure 5.9 (a)). For an adsorption rate constant of 1×10^{-3} 1/s, HELP-1D predicted significant adsorption of Calfax to o/w IF compared to nMag particles. 25% of the injected mass of surfactant was removed from the aqueous phase for $C_0 = 10$ mg/L, and when this number was increased to 100 mg/L, ca. 7% of surfactant mass was retained by the o/w IF.

Inspection of the spatial profiles of adsorbed surfactant in the column (Figure 5.10) shows that the maximum interfacial concentration of Calfax increases with C_0 . The adsorbed surfactant concentration is controlled by the surface capacity (i.e. surface excess) of o/w IF which in turn is directly but non-linearly related to C_0 (Figure 5.5). Increasing the surfactant concentration, as expected, enhanced the oil phase solubilization kinetics in the column thereby increasing the effluent dissolved oil concentrations (Figure 5.9 (b)). However, the eluted dissolved oil in both simulations accounted for less than 0.01% of the initial mass of oil in the system.

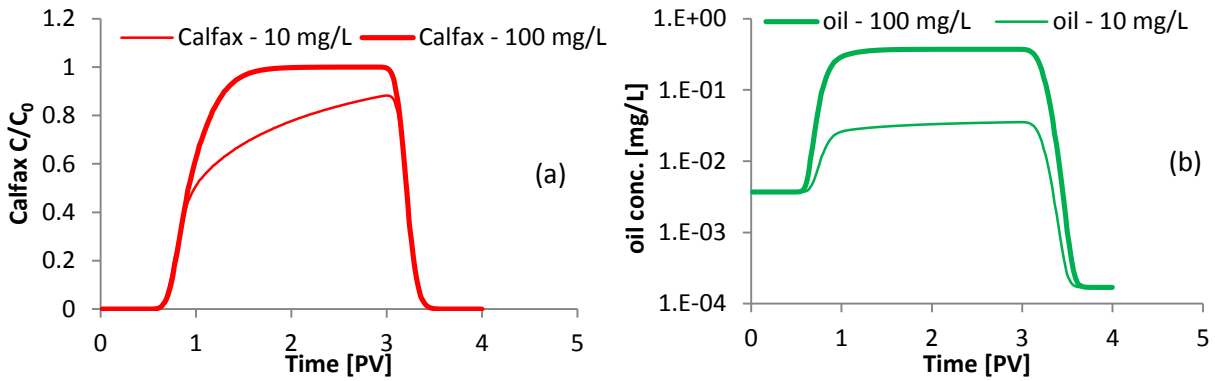


Figure 5-9. Simulated effluent concentrations of (a) Calfax 16L-35 and (b) dissolved IsoparL. Here, surfactant and dissolved oil adsorption to the solid phase is neglected.

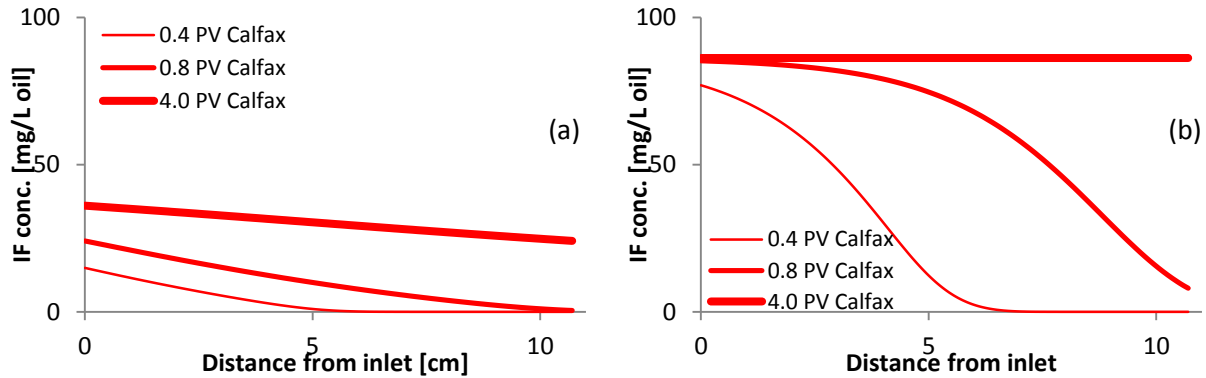


Figure 5-10. Simulated retention profiles of Calfax 16L-35 adsorbed to the o/w IF at different simulation times corresponding to 0.5, 1.0 and 5.0 aqueous PVs for C_0 values (a) 10 mg/L and (b) 100 mg/L. Here, surfactant adsorption to the solid phase is neglected.

5.4.1.3. Simultaneous Transport of nMag and Calfax 16L-35 surfactant

The mobility of nMag particles, under conditions specified in Table 5.1, in the presence of Calfax surfactant was numerically explored. A 3 aqueous (2.4 total) pore volume pulse of 1 mg/L nMag and 10 mg/L Calfax surfactant was introduced to the porous medium. The column was subsequently flushed with background solution for up to 4 (total) pore volumes. The simultaneous NP attachment and surfactant adsorption to the o/w IF were simulated based on two distinct site-blocking scenarios: (1) a one-site competitive and (2) an independent non-competitive scenario. Simulation results are shown in Figure 5.11.

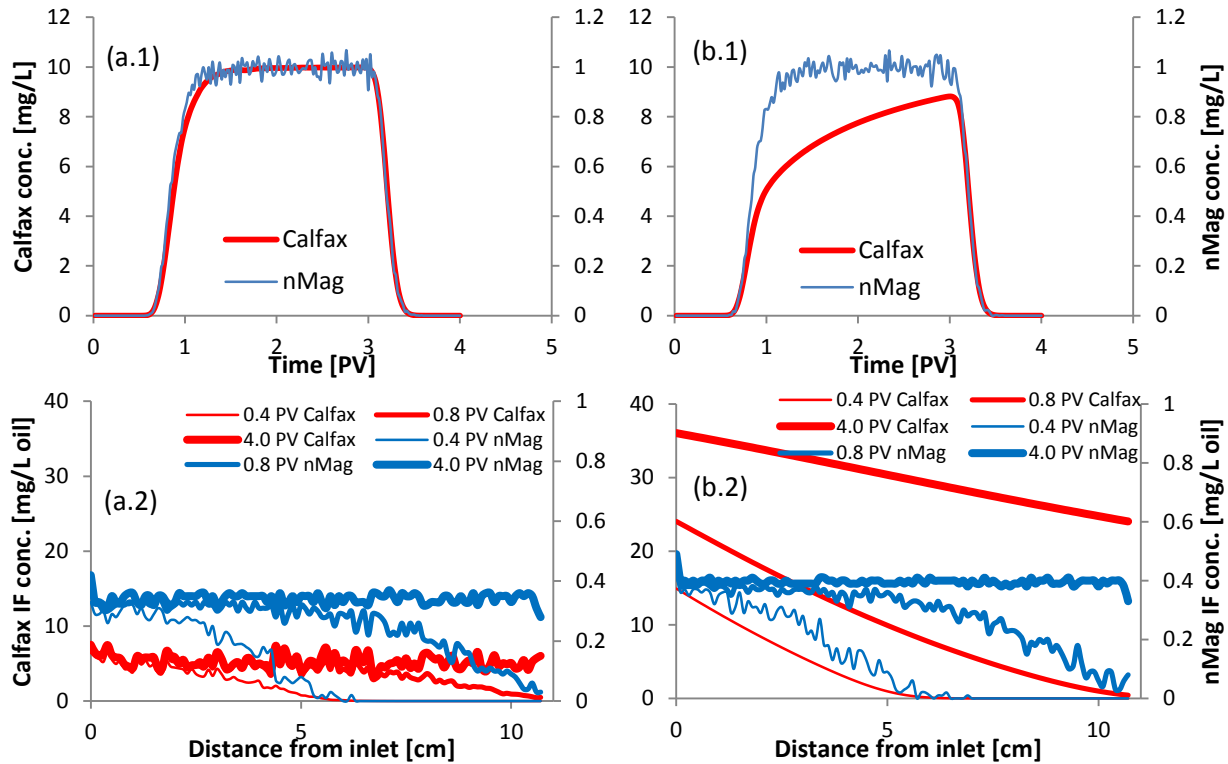


Figure 5-11. Simulated (1) effluent concentrations and (2) retention profiles of nMag ($C_0 = 1$ mg/L) and Calfax 16L-35 ($C_0 = 10$ mg/L), based on (a) competitive one-site and (b) non-competitive site-blocking models.

Simulations, under non-competitive conditions, yielded a predicted retention of ca. 3.5% of particles and a ca. 25% removal of the injected surfactant mass by the o/w IF

(Figure 5.11 (b.1)). When competitive site-blocking was assumed, the percent retention of nMag and percent removal of Calfax from the aqueous solution (caused by the o/w IF) decreased to ca. 2.8% and 4.4%, respectively (Figure 5.11 (a.1)). Comparison of simulated retention profiles suggest that the enhancement of the transport through the sand column was more pronounced for the surfactant than the NPs. No overall conclusion can be drawn from these predictions, however, because they are based on hypothetical values for $k_{surf\ init}^{if}$ and α_{if} . A subsequent sensitivity study (Subsection 5.4.2) revealed that simulations are strongly sensitive to changes in these kinetic parameters.

Assessment of the effect of kinetic processes on the transport and retention of nMag particles using the experimental surface excess data was difficult, because of the estimated low surface capacity of the IF for nMag. Depending upon the solution, o/w IF and particle surface chemistry, particle surface coating composition, and physical factors such as temperature and pore pressure, NPs may exhibit various levels of affinity for the o/w IF. To demonstrate the potential influence of rate-limitations associated with adsorption and attachment processes on the mobility of NPs, the experimental nMag surface excess (Γ_{exp}) curve was magnified one order-of-magnitude. This suppressed the controlling effect of the o/w IF surface capacity in all of the remaining simulations presented in this chapter.

The transport of nMag was simulated at the increased surface excess both with and without the presence of Calfax surfactant. In the absence of the surfactant, this magnification increased NP retention in the column from 3.5% to ca. 23% using a $\alpha_{if} = 0.13$ (Figure 5.12 (b)), and produced enough surface capacity for the interfacial sites so that nMag mobility was not merely controlled by the availability of interfacial sites (Figure 5.12 (a)).

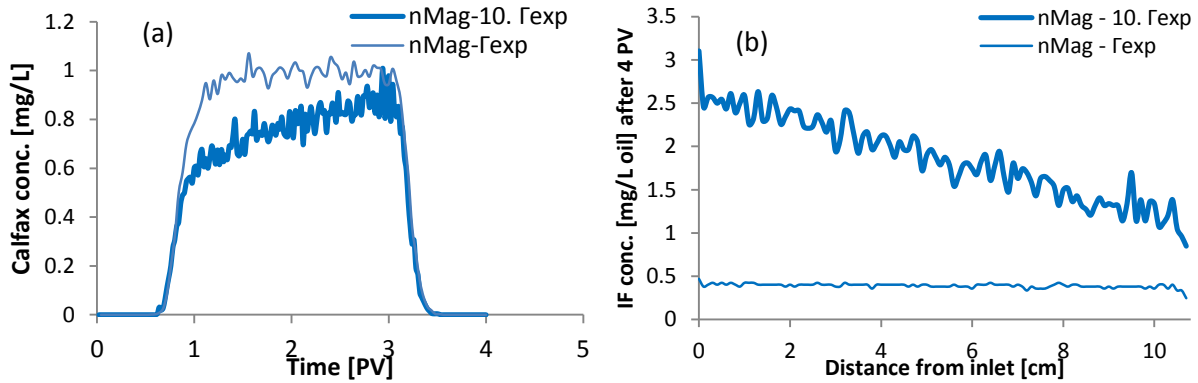


Figure 5-12. Simulated (a) effluent concentrations and (b) retention profiles of nMag inside the column (in the absence of surfactant) using the experimental Gibbs surface excess (Γ_{exp}) and a hypothetical surface excess curve one order-of-magnitude greater than Γ_{exp} . Here, nMag interactions with solid phase are disregarded.

The results of the simulation of nMag interactions with the o/w IF in the presence of competing surfactant molecules are shown in Figure 5.13. As expected, the competition increased nMag mobility. nMag retention in the column decreased from ca. 23% (the surfactant-free system) to 9.4% when the surfactant was co-injected with particles (Figure 5.13 (a)). The simulated effluent concentrations of both components approached the influent concentration after approximately 3 pore volumes (Figure 5.12 (a)) suggesting that o/w IF was fully saturated. Inspection of Figure 5.13 (b) reveals that the interfacial concentration of each component is lower than that for nMag-only (Subsection 5.4.1.1) and Calfax-only (Subsection 5.4.1.2) scenarios. Figure 5.13 (c) shows the predicted aqueous concentration profiles of dissolved oil as the surfactant concentration front advances in the porous medium. It can be seen that at each point in space, the rate at which dissolved oil concentration increases (the slope of the dissolved oil curve) is proportional to the local surfactant concentration. This trend is consistent with the surfactant-enhanced dissolution model incorporated (Eq. 5.3). Less than 0.01% of the initial mass of oil dissolved during simulated time suggesting that the loss of

interfacial sites due to dissolution did not significantly influence nMag interactions with the o/w IF.

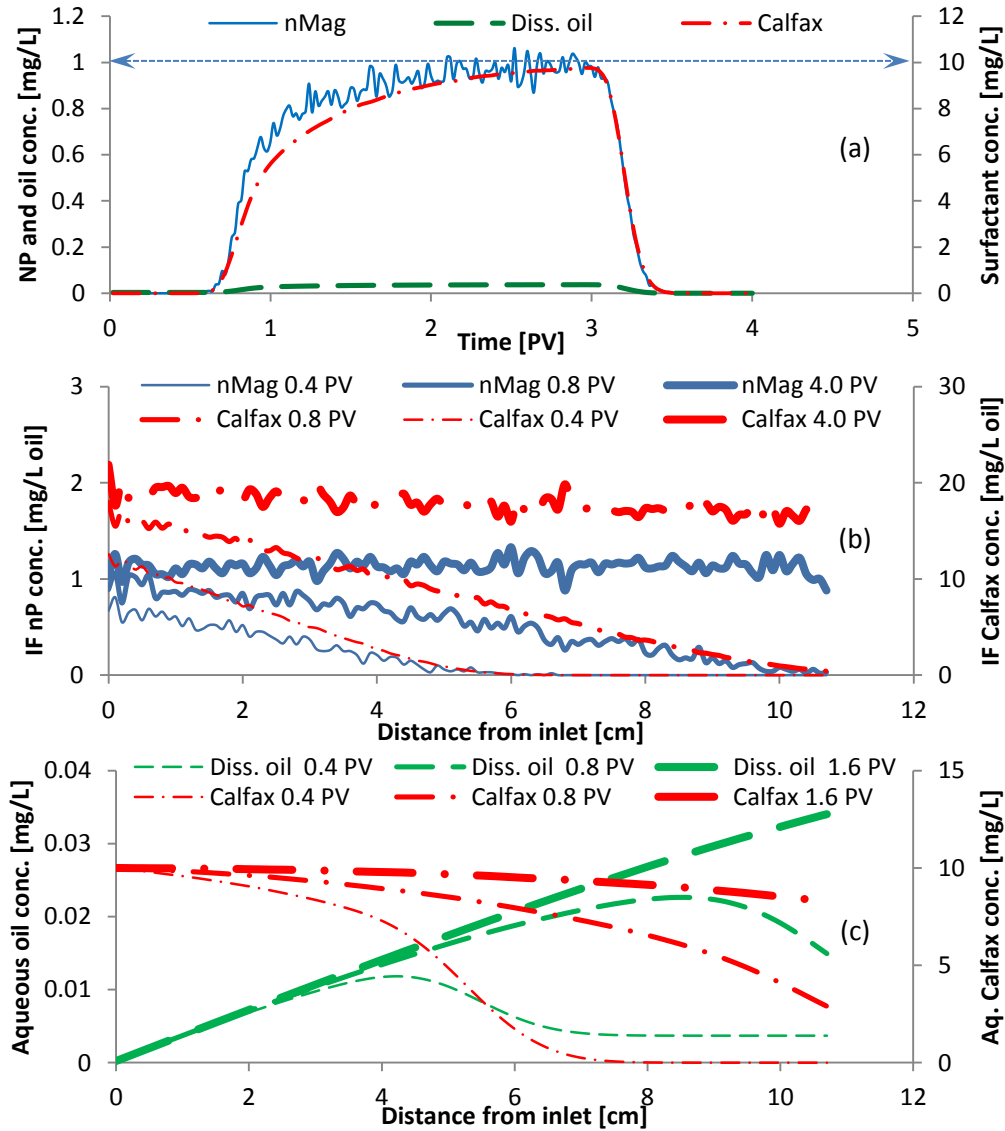


Figure 5-13. Simulated nMag and Calfax 16L-35 surfactant (a) effluent and (b) retained concentrations, and (c) aqueous phase concentration profiles of Calfax16L-35 surfactant and dissolved oil. Here, the interactions of nMag and Calfax 16L-35 with the solid phase are disregarded.

The scenario described above (with the increased nMag surface excess) is used as the **base case** in the sensitivity study that is presented in the following subsection.

5.4.2. Sensitivity Analysis

5.4.2.1. Sensitivity to Physicochemical Parameters

The sensitivity of the mobility of nMag particles to variations of several model input parameters including (a) the Gibbs surface excess, (b) surfactant adsorption and (c) NPs attachment rate constant, and (d) the influent concentration of the surfactant, was evaluated. Recall that the adsorption rate coefficient (k_{surf}^{if}) of 1×10^{-3} 1/s and NP attachment efficiency to the o/w IF (α_{if}) of 0.13 (used in the base case scenario) were selected hypothetically. The selection of these hypothetical values combined with the implemented surface excess values (increased one order-of-magnitude from experimental estimates for nMag), however, created a higher level of surfactant adsorption (adsorption of ca. 14.9% of the input mass of Calfax) compared to NP attachment (retention of ca. 9.4% of the input mass of nMag).

Note that the performed analysis is in a preliminary stage. A comprehensive sensitivity study will be subject to the availability of pertinent experimental data on the NP transport in the oil-containing porous media. The main purpose of this analysis, in the absence of experimental information necessary for meaningful conclusive statements, was to demonstrate HELP-1D performance and capabilities.

(a) Sensitivity to the surface excess of NPs: A one order-of-magnitude decrease/increase of the nMag surface excess decreased/increased nMag retention in the column from ca. 9.4% (base case) to ca. 2.3%/13.2%, respectively. A similar effect was predicted for the transport of the surfactant. A one order-of-magnitude decrease/increase of the nMag surface excess increased/decreased Calfax elution from ca. 85.1% (base case) to ca. 96%/79.2%, respectively. As the surface capacity of o/w IF for nMag decreases the amount of particle mass required to saturate the interfacial sites decreases

leading to an increase in the effluent NP concentrations (Figure 5.14 (a)). In a competitive site-blocking scheme the transport of Calfax was also facilitated by a reduction in the surface capacity for particles, because of the increased sensitivity of the interfacial site blocking function (Eq. 5.11) to changes of surface concentration which would affect both competing components.

(b) Sensitivity to surfactant adsorption rate coefficient: Due to the lack of relevant experimental data, “How close of a reflection of reality do the presented hypothetical predictions provide?” is a question impossible to answer. Nevertheless, “How the mobility of NPs can be influenced due to changes in the surfactant adsorption coefficient?” is a question that the author has attempted to find an answer to on a **relative basis**. Decreasing k_{surf}^{if} by one order of magnitude enhanced nMag retention from 9.4% to 18.0%, while increasing k_{surf}^{if} by the same order, strongly promoted NP mobility (< 2% retention) (Figure 5.14 (b)). The predicted strong sensitivity further confirms the importance of accurate characterization of the kinetic aspect of the surfactant adsorption to the o/w IF for a meaningful assessment of NPs interaction with interfacial sites.

(c) Sensitivity to NP attachment efficiency to o/w IF: NP attachment efficiency to the o/w IF (α_{if}), the fraction of particle collisions with the interface that results in sticking, is a factor determined by the chemical characteristics of the solution, interface, and particles, and thus, is a system-specific parameter. As expected, variations in α_{if} directly influenced the mobility of nMag particles. A one order-of-magnitude reduction of α_{if} from 0.13 (base case) to 0.013 decreased nMag retention from ca. 9.4% to 1.5%, a value which then increased to ca. 20.0% when α_{if} was increased to its maximum possible theoretical value (i.e. $\alpha_{if} = 1$) under diffusion-limited conditions for particle attachment.

A decrease/increase of α_{if} inversely influenced the mobility of the surfactant (Figure 5.14 (c)), via accelerating/decelerating the blocking of interfacial sites by nMag particles.

(d) Sensitivity to Influent Surfactant Concentration: The plausible surfactant concentrations associated with NP transport problems can range widely in practice. Surfactants can be present in minuscule amounts as residuals from the NP synthesis or particle coating process, or can be intentionally injected in significant quantities to alter the transport properties of NPs in the subsurface. The influent concentration of Calfax was varied between 5-20 mg/L. Increasing the C_0 of the surfactant from 10 (base case) to 20 mg/L, slightly increased the nMag retention from 9.4% to 10.4% while decreasing the surfactant C_0 to 5 mg/L remarkably enhanced NP mobility (< 4% nMag retention) (Figure 5.14 (d)). One might expect by intuition that in a competitive adsorption/attachment scheme, decreasing the concentration of one of the competing components (i.e. the surfactant) would facilitate the attachment of the other component (i.e. nMag in this case) thereby reducing the overall particle mobility. Here, however, the simulations suggest: Not necessarily!

The explanation lies in the non-linear nature of the relationship between the surface excess and bulk phase concentration of Calfax surfactant (Figure 5.4 (a)). According to experimental measurements, a 2-fold reduction of the surfactant C_0 from 10 to 5 mg/L results in a ca. 6.5-fold reduction of the Gibbs surface excess from ca. 2.8 to 0.43 mg/m². That is, the reduction in the surface capacity of o/w IF (due to the decrease in surfactant concentration) was a limiting factor that controlled the NP/surfactant interactions with the o/w IF.

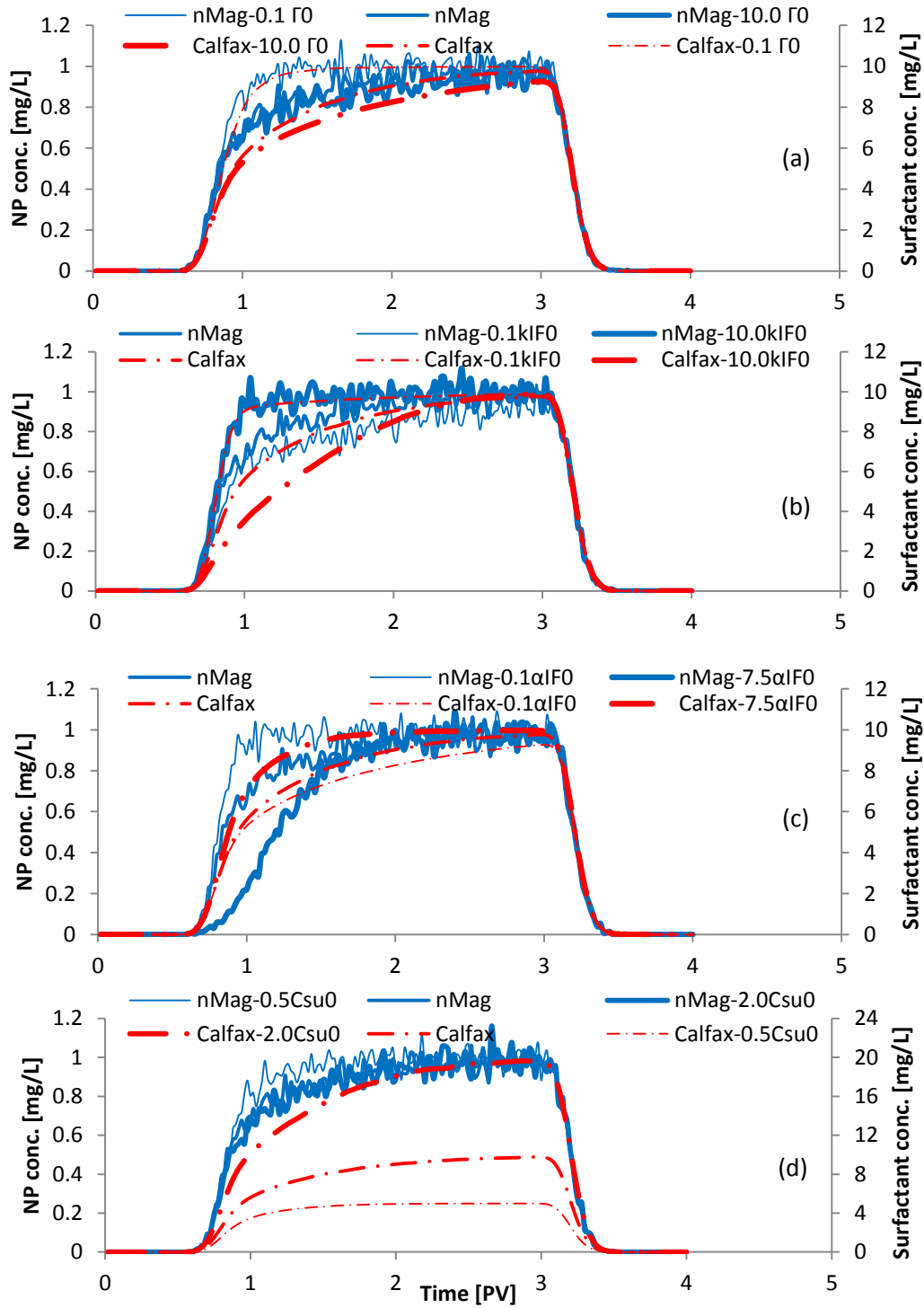


Figure 5-14. Influence of (a) the nMag surface excess, (b) the rate coefficient of surfactant adsorption to the o/w IF ($1 \times 10^{-4} - 0.01$ 1/s), (c) the attachment efficiency of nMag to the o/w IF (0.013-1.0), and (d) influent Calfax 16L-35 concentration on the simultaneous transport of Calfax 16L-35 and nMag particles in a sand column containing 20% saturation of oil at constant pore velocity of ca. 7.6 m/day.

5.4.2.2. Sensitivity to Numerical Model Parameters

As described in Subsection 5.3, an explicit time lag-based numerical approach was implemented for simulating the competitive site-blocking. To evaluate and avoid the potential approximation in the numerical solutions due to the choice of discretization parameters (i.e. the time increment, Δt , and grid-block spacing, Δx), a model sensitivity analysis was undertaken. Δt and Δx were varied in a range of 0.5-10 s and 0.5-2 mm, respectively, yielding Courant numbers ($Cr = v_w \cdot \frac{\Delta t}{\Delta x}$) as high as 1. The sensitivity of model predictions was evaluated over a ca. 2 order-of-magnitude range of α_{if} (0.013-1.0) while the surfactant adsorption constant was kept constant in all simulations.

The strongest sensitivity was observed for an $\alpha_{if} = 1$ (providing the fastest theoretical attachment rate possible). Decreasing Δx from 1 to 0.5 mm ($\Delta t = 1$ s) introduced a 5.1% discrepancy in the predicted NP retention (3.32% vs. 3.16% of NP retention at 4 PV). A 2-fold increase of Δx (from 1 to 2 mm) was associated with a ca. 3% increase in the predicted NP retention (from 3.32% to 3.42%). Variations in the time step sizes had a minimal influence ($< 0.5\%$) on the predicted NP retention.

The highest sensitivity to Δt was recorded when Δt was increased from 1 to 10 s ($\Delta x = 1$ mm) for the lowest considered α_{if} of 0.013 where a ca. 2.3% discrepancy was introduced in the model estimate for NP retention (1.19% vs. 1.22% of NP retention at 4 PV). The maximum change in the predicted NP retention was lower than 1.1% and 0.5%, respectively, for α_{if} -values of 0.13 and 1.0.

The results of this sensitivity analysis are provided in Appendix III.1.1 of this dissertation.

5.5. Conclusions

In this chapter, a mathematical model was developed and incorporated into HELP-1D for representing the simultaneous interactions of NPs and surfactants with the o/w IF, which implements (1) a multi-constituent competitive (based on the method proposed by *Becker et al.* [126]) and (2) a non-competitive site blocking approach. The presented model, unlike previous models (e.g., *Bishop et al.* [50]), considers a finite maximum capacity for the retention/adsorption of NPs/surfactant by the o/w IF, a capacity which is approximated by the Gibbs surface excess.

Due to the potential for enhanced oil phase solubilization in water in the presence of surfactants, HELP-1D was made capable of accounting for spatiotemporal changes in oil phase saturation and surface area. However, simulation results suggest that for the typical experimental conditions and time scales of transport column studies, oil phase dissolution effects seem unlikely to have an influence on the NP – o/w IF interactions. A model sensitivity analysis was conducted which suggested nMag mobility was directly related to Calfax 16L-35 surfactant adsorption rate coefficient and inversely to the NP attachment efficiency to the o/w IF.

Our proposed approach could not be validated at this time due to a lack of sufficient experimental data on the retention and transport of NPs in the oil-containing porous media. It should be noted however, that neither of the two site-blocking scenarios, is likely to be representative of reality. A one-site fully-competitive model seems unlikely because of the slight surface coverage of the IF (ca. 0.4%) by nMag particles even at the highest estimated surface excess (ca. 0.14 mg/m² of IF (Figure 5.5)). On the other hand, preliminary experimental data (Prof. Pennell's research group (Dr. Wang, Y.)) demonstrate a higher level of NPs mobility for the column experiment pre-flooded with

Calfax prior to the introduction of nMag compared to when a premix of Calfax and nMag was injected. This suggests that the surfactant has an inhibitory effect on NPs attachment to the capture sites, ruling out the possibility of a non-competitive site-blocking process. Hence, the considered site-blocking scenarios should be viewed as representative of the two extreme ends of a range of scenarios that may contain an intermediate representative site-blocking scenario. Moreover, the presented approach, considers the mass accumulation on the o/w IF to be an irreversible process, should the experimental evidence indicate otherwise, the governing equations for the mass exchange with the interfacial sites must be modified to account for surfactant desorption and NPs detachment. Addressing the partial competition, which requires a two-site competitive/non-competitive site-blocking model, and/or reversible mass exchange with the o/w IF, however, will be subject to further pertinent experimental data.

Lastly, it must be emphasized that the sole reason for neglecting the NP/surfactant interactions with the solid phase was the simplicity of the interpretation of simulations results and demonstration of model capabilities. By no means, the author of this dissertation intends to minimize the relative importance of interactions with the solid phase (compared to the o/w IF) on the retention and transport of NPs in porous media. On the contrary, the preliminary experimental observations (Prof. Pennell's research group (Dr. Wang, Y.)) suggest that sites on the solid surfaces may act as primary capture sites for nMag particles in the presence of Isoparl oil residuals. *Bishop et al.* [50] attributed ca.50-100% of the retention of ZVI particles (coated with different anionic homopolymers) to the solid phase in the presence of dichlorobenzene residuals, which further emphasizes the significance of interactions with the solid phase in the real systems.

Chapter 6 CONCLUSIONS AND RECOMMENDATIONS

6.1. Conclusions

This work has sought to model the reactive transport of nanoparticles (NPs) in porous media taking into account an aspect which has almost always been neglected in previous modeling investigations: **Non-uniformity** in physical characteristics of NPs. Size, age, and specific surface area are some examples of NP characteristics subject to non-uniformity. Spatiotemporal variation of these physical factors not only influences the physical behavior of NPs (e.g., transport and particle-solid phase collisions), but may also affect their chemical reactivity.

In this work, a hybrid approach was devised by combining an Eulerian (i.e. finite differencing) and a Lagrangian (i.e. random-walk particle-tracking) method to simulate the reactive transport of NPs and co-existing dissolved constituents, simultaneously. Based on this approach, a one-dimensional numerical simulator was developed that was named HELP-1D, an acronym for Hybrid Eulerian Lagrangian Particle transport. Interactions of NPs with the porous medium, residuals of a secondary non-aqueous liquid phase, and other NPs were incorporated into HELP-1D. The presented numerical technique splits the mass of NPs among a large number of parcels, here called model particles, each of which represents a subpopulation of actual particles. The physicochemical characteristics assigned to each model particle are specific to that particle, and thus, can vary from particle to particle. Moreover, in this treatment, both the evolution of model particles based on their particle-specific migratory paths in a porous

medium, and the processes that control this evolution (such as particle surface aging and NP aggregation) can be addressed.

Aside from its capability to account for non-uniformity effects, the developed approach offers other advantages, as well as a number of limitations, over existing models. The deficiencies of the Lagrangian approach include: (a) the strong dependence of numerical precision and solution accuracy on the number of modeled particles, potentially resulting in time and memory intensive simulations, and (b) inapplicability of the approach to inverse problems (parameter estimation) due to random perturbations associated with the Lagrangian solutions.

After verification of the accuracy of its numerical solutions, HELP-1D was applied to investigate the fate and transport of NPs in a number of practical problems. These problems included (1) the reductive dechlorination of chloroethenes by zero-valent-iron NPs (nZVI) in a PCE-DNAPL source zone, (2) the transport and retention of dissolving silver NPs (nAg) in porous media, accounting for the effects of particle surface passivation and dissolved oxygen, (3) particle-particle (PP) interactions (i.e. aggregation) and their influence on physical behavior of NPs in porous media, and (4) NPs interaction with the oil/water interface (o/w IF) in the presence of an immobile oil phase and its influence on NPs mobility. The numerical investigation of the first two problems was coupled with experimental studies conducted by Prof. Pennell's research group. In both cases, HELP-1D accurately captured experimental findings from column studies on nZVI and nAg.

In the case of nZVI-mediated dechlorination, model sensitivity analyses revealed that PCE transformation efficiency was strongly dependent upon the mass and spatial distribution of nZVI, as well as the initial PCE mass and the mean residence time of

dissolved contaminant in the reactive zone. HELP-1D predicted higher conversion of PCE to ethane with a reduction in flow velocity at the expense of increased treatment time. The concentration and duration of effluent PCE was directly related to the extent of the DNAPL source zone. In addition, the spatial distribution of nZVI particles was found to significantly influence PCE transformation. Simulation results predicted that the placement of nZVI zone down-gradient from the DNAPL source improves the treatment effectiveness by both enhancing the transformation efficiency of PCE and reducing the effluent PCE concentrations. This prediction was confirmed by a later experimental study of *Fagerlund et al.* [136]. They asserted that the nZVI, needed to degrade a DNAPL source, must be placed down-gradient of the source eliminating any influence of dechlorination reactions on the rate of dissolution. Mathematical and experimental results demonstrated that a meaningful treatment of DNAPL source zones with nZVI requires careful attention to remedial design parameters including the amount and spatial distribution of nZVI delivered.

The numerical study presented in Chapter 3 involved the transport and dissolution of nAg in porous media. Dissolution is a process that can create non-uniformity in the transport properties (by reducing the size) and reactivity (by increasing the specific surface area of nAg). At the same time, this process can be influenced by particle non-uniformity effects (e.g., particle age-specific dissolution kinetics). To the best of the author's knowledge, however, no previous investigations on the environmental fate of nAg had addressed the coupled (a) transport and retention and (b) oxidative dissolution of nAg. Findings of this study reveal the importance of accounting for both the particulate and dissolved forms of silver. HELP-1D accurately described experimental data on the transport and dissolution of nAg in short-term (hours) and long-term (days) studies. HELP-1D simulations suggest that seepage velocity will have a

distinct effect on the transport and dissolution of nAg under typical groundwater flow conditions. The role of dissolution and transport in the dissolved form is predicted to be more pronounced at lower velocities due to increased residence time for dissolution and enhanced particle-soil collector contact efficiency. Additionally, it was found that dissolution would be the governing mechanism for Ag transport for very small particles, as the mobility of smaller nAg (< 10 nm) is remarkably suppressed due to the strong influence of Brownian diffusion on particle attachment.

Particle aggregation, another process that can result in particle non-uniformity, was the subject of the third problem explored in this research. The mobility of colloidal particles in porous media has a highly non-linear dependence on their size. An increase in the effective hydrodynamic diameter due to aggregation can significantly alter the transport characteristics of NPs. In spite of its potential influence on NP mobility, aggregation has generally been ignored by conventional colloidal transport models. To account for aggregation, a Lagrangian solution to the aggregation equation was derived and was coupled with the RWPT module of HELP-1D. The developed approach is mass conservative and facilitates calculation of the maximum cluster size unlike other existing models that treat this parameter as an input parameter. The main advantage of the RWPT modeling approach, however, lies in its ability to model polyadic collisions as opposed to binary collisions associated with Eulerian models.

The last problem that was explored in this study was the effect of NP interactions with the o/w IF in the presence of surfactants on their transport in porous media containing a residual non-aqueous liquid phase. An extension of modified filtration theory that accounted for competitive adsorption/attachment of

surfactants/NPs to soil grain surfaces was adapted and refined to include an o/w IF. There are two distinctions between solid phase and interfacial sites: (1) the surface capacity of the solid phase is constant, unlike that of the interfacial sites which is represented by the experimentally determined Gibbs surface excess and is a component-specific property that can vary in time and space as a non-linear function of bulk aqueous concentrations of the surfactant and/or NPs, and (2) in contrast to the non-deformable solid surfaces, the surface area of the interfacial sites is subject to change due to oil-phase solubilization, a process that can be significantly enhanced by the presence of surfactants. Simulations based on the measured interfacial tension of Isopar¹/water interface in the presence of nMag particles and Calfax 16L-35 surfactant, suggest only a small reduction in nMag mobility in the porous media (ca. 2.8% retention) due to interactions with the o/w IF. Modeling results suggested that the retention of nMag in the column was controlled by the (experimentally determined) limited surface capacity of interfacial sites and not the (hypothetically selected) kinetic attachment parameters. In addition, the reduction of the interfacial area due to oil dissolution was found to have a negligible influence on the NP-o/w IF interactions within the typical time-scale of column experiments. HELP-1D predicted less than 0.01% decrease in the mass of residual oil during a 3 (aqueous) pore volume pulse of 100 mg/L of surfactant through a column containing an initial oil phase saturation of 20%. Note, however, that solubility limit of the organic phase, the extent of enhancement of the solubilization due to presence of surfactants, and solubilization rates can vary substantially for different organic phase-surfactant

species combinations. Beyond that, the hydrodynamic characteristics of flow and porous medium, the initial saturation and configuration of the organic phase, and the time scale of a problem of interest are other important factors that can remarkably signify the effect of changes in the organic liquid phase saturation on the flow field and the capture sites on the o/w IF as well.

6.2. Recommendations and Future Directions

- I. The presented hybrid Eulerian-Lagrangian approach may prove useful in tracking the behavior of other metallic nanoparticles prone to chemical reactions and/or dissolution in aqueous environments, such as ZnO and CdSe quantum dots. HELP-1D provides a numerical framework that can be used to simulate the reactive transport of other NPs that exhibit non-uniform physicochemical characteristics and/or NPs that experience a transformation of properties based on particle-specific and/or path-specific migration in porous media.
- II. As far as particle-particle (PP) interactions are concerned, the developed Lagrangian scheme for the coupled NPs transport and aggregation, accounts for perikinetic (Brownian diffusion-based) aggregation that allows for modeling the interactions between particles moving with the aqueous phase at similar average velocities. To simulate the interactions between suspended particles and stationary particles retained by the porous medium, orthokinetic aggregation, which accounts for fluid shear effects, must be incorporated in HELP-1D. This type of PP interaction may prove important for the transport scenarios where a significant proportion of the collector surfaces is covered by the retained particles and/or where other forces in addition to hydrostatic repulsion and van Der Waals attraction control PP interactions (e.g., magnetic forces acting on nZVI particles).

- III. A systematic validation of the developed mathematical for representing NPs interaction with o/w IF will depend upon the availability of pertinent experimental data on the transport and retention of NPs in oil-containing porous media. The proposed mathematical formulation only addresses one type of NP-surfactant interactions with the o/w IF that are of a competitive or neutral nature. Alternative constitutive expressions will be required should the existence of a constituent have a synergistic effect on the NP retention by the o/w IF.
- IV. Extending HELP-1D to multiple dimensions, necessary for applicability to field-scale problems, would be a future expansion of this work, which can be achieved easily as for the associated mathematical complexities. Coupling the Lagrangian module of HELP simulator with any multi-dimensional flow model is a straightforward task, and with a known velocity field, the explicit Lagrangian solutions will not be disturbed by numerical issues (e.g., convergence and conservation of mass) that potentially affect the existing Eulerian models. Also, numerous multi-dimensional multi-component transport models exist (e.g., MT3DMS) that can serve as the Eulerian module of the extended hybrid simulator. The inter-module communication, in the proposed approach, is accomplished by means of local sink/source terms. This communication scheme can readily be adopted by many existing transport simulators and will not require extensive effort. Given the computational burden of RWPT simulations, even for the one-dimensional problems, the implementation of a parallel programming scheme for any multi-dimensional extension to HELP is strongly recommended. This parallelization can be process-based (i.e. a separate treatment of independent processes (e.g., NP attachment and NP detachment)), population-based (i.e. dividing the model particles into smaller subgroups and appropriating these subgroups to multiple computing nodes), or a combination of both.

APPENDICES

Appendix I

I.1. Some Notes on the Solution Algorithm of HELP-1D Simulator

Simulations start with solution of the aqueous phase flow equation (i.e. Equation 5.1), and then proceed with solution of the particle mass balance equation (i.e. Equation 5.5). A Lagrangian random-walk particle-tracking (RWPT) method is implemented for solving the advective-dispersive terms of the mass balance equation for nanoparticles. Applying the superposition principle, particle-particle (i.e. aggregation), particle-solid phase (i.e. deposition and detachment), and particle-dissolved phase (i.e. chemical reactions) interactions are simulated separately. The former two types of interactions are solved stochastically, whereas the latter type (i.e. the chemical reactions) has a deterministic solution. Passing the reaction information, the reactive transport equations for dissolved constituents are solved sequentially. The phase and dissolved constituent mass balance equations are discretized using a generally weighted finite-differencing scheme. Phase saturations are then computed by solving the NAPL phase mass balance equation (i.e. Equation 5.2). A schematic of the solution algorithm is illustrated in Figure 0.1.

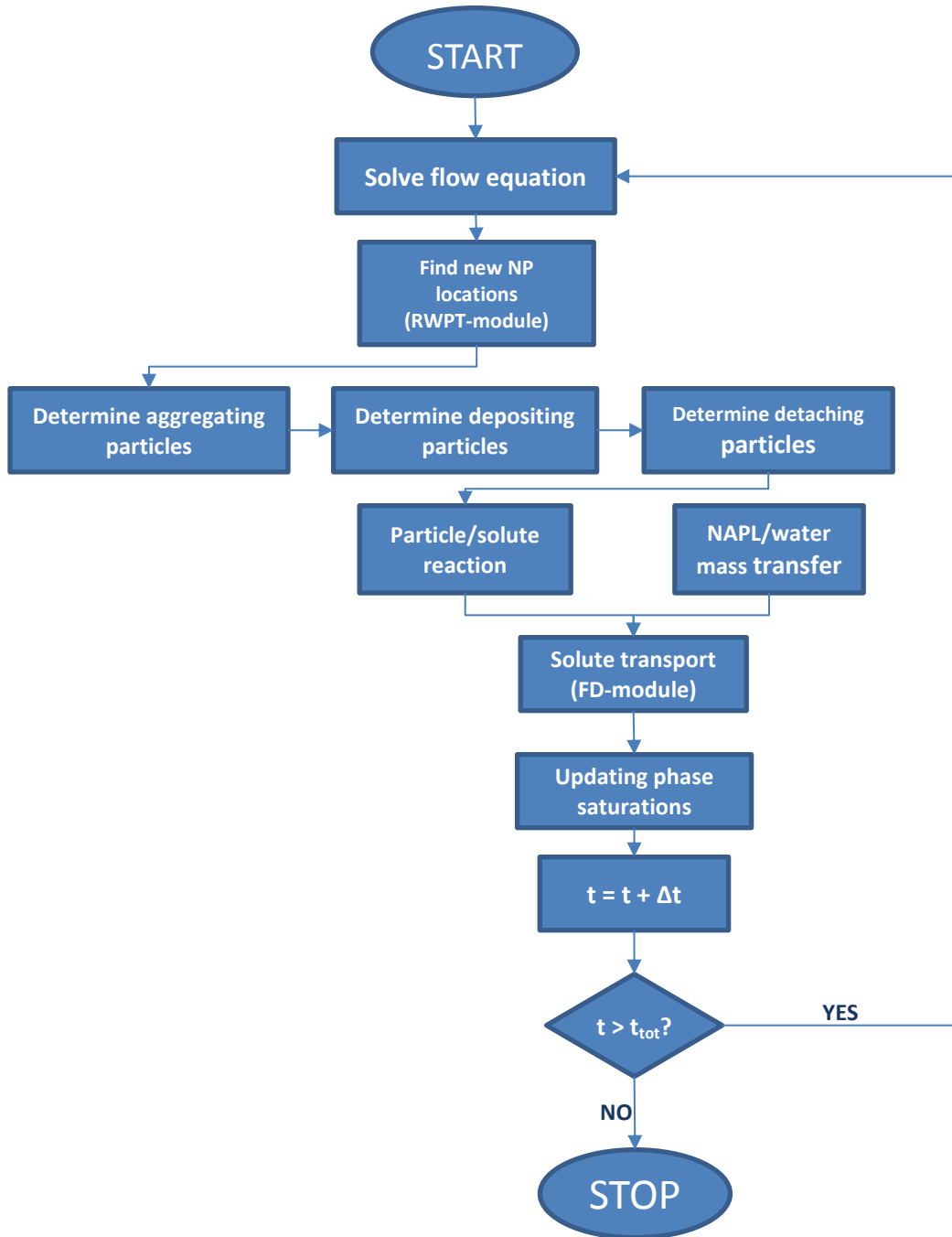


Figure 0-1 Solution algorithm flowchart of the hybrid simulator

Appendix II

II.1.Verification of Transport Modules of HELP-1D

The hybrid simulator has two coupled modules: (1) A *Lagrangian reactive* particle transport module (RWPT), and (2) an *Eulerian* reactive solute transport module (FD). The RWPT module was verified through comparisons with analytical solutions (*van Genuchten*, 1986) and with the results from an existing previously verified particle transport code (*Li et al.*, 2008). Analytical solutions were used for transport of a pulse of non-attaching particles and a pulse of particles that attach according to the Classical Filtration Theory (CFT). Results from the *Li et al.* (2008) model were used for transport of particles that attach according to the Modified version of the classical Filtration Theory (MFT). The FD module was verified through comparisons with analytical solutions (*van Genuchten*, 1986) for transport of a nonreactive pulse of a tracer solute and a pulse of a reactive solute (i.e. dissolved trichloroethene reducing to ethene).

II.1.1.Verification of the RWPT (i.e. particle transport) module

Breakthrough results of the RWPT module and those obtained analytically for (1) a 2 pore volume input pulse of non-attaching (tracer) particles and (2) a 3 pore volume continuous injection of attaching particles according to CFT are shown in Figure 0.2. Illustrated in Figure 0.3 are (1) the breakthrough and (2) the retained concentrations for a 3 pore volume pulse of attaching particles according to MFT for non-detaching particles. Comparison curves for the (1) breakthrough and (2) retention (after 20 pore volumes flushed) of a 3 pore volume pulse of reversibly attaching particles (i.e. simultaneous attachment and detachment) according to MFT are presented in Figure 0.4. Perfect mass

balance is achieved automatically in all RWPT simulations, consistent with the nature of the Random-Walks method.

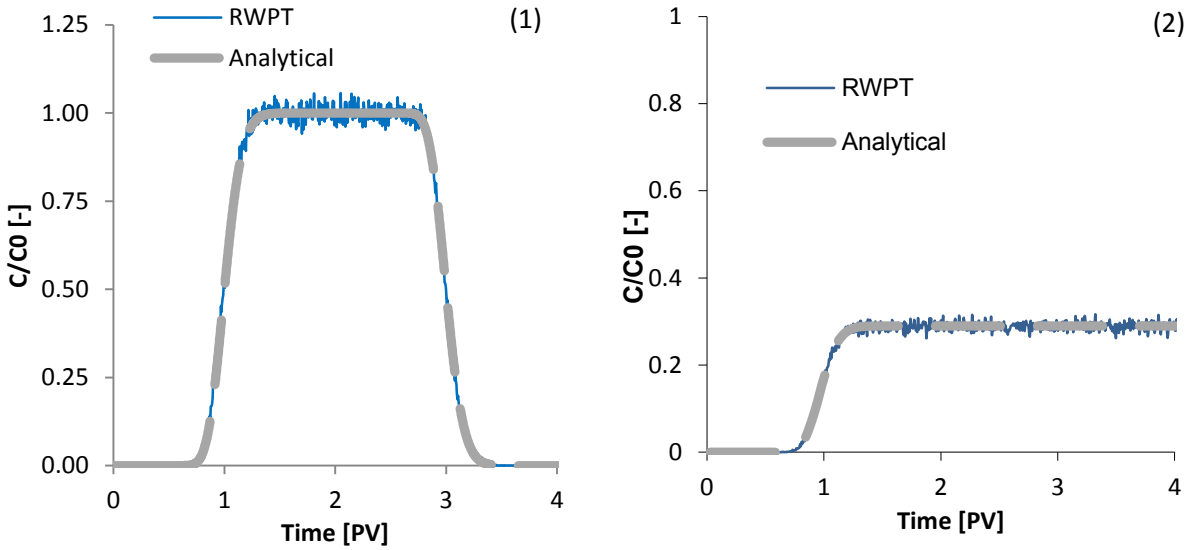


Figure 0-2. A 2PV pulse of non-attaching particles (1), and a 3PV continuous injection of attaching CFT particles (2).

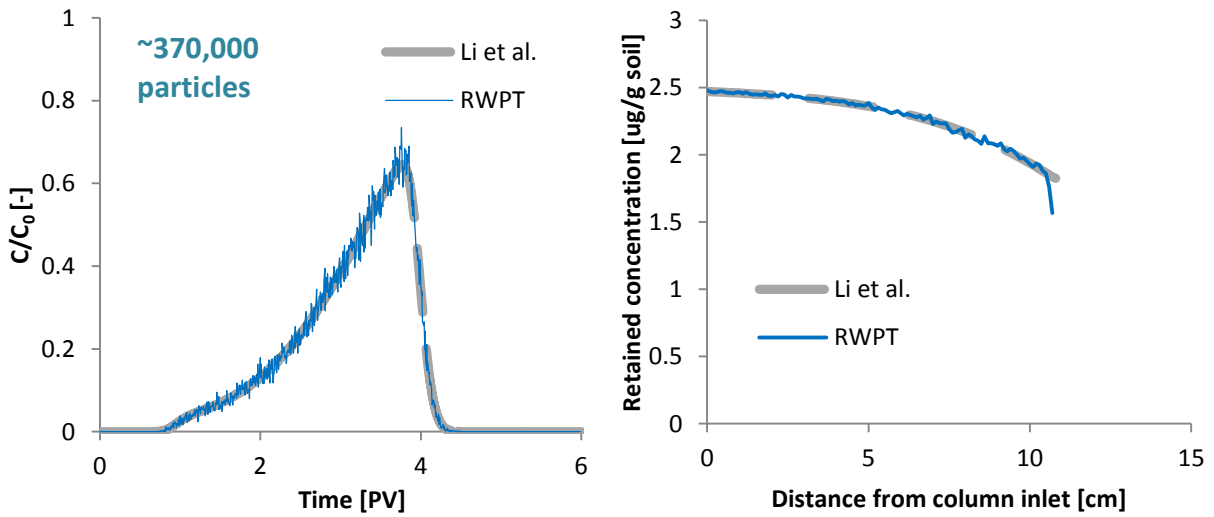


Figure 0-3. Breakthrough (1) and retained (at 6 PV) (2) concentrations of irreversibly attaching particles according to MFT.

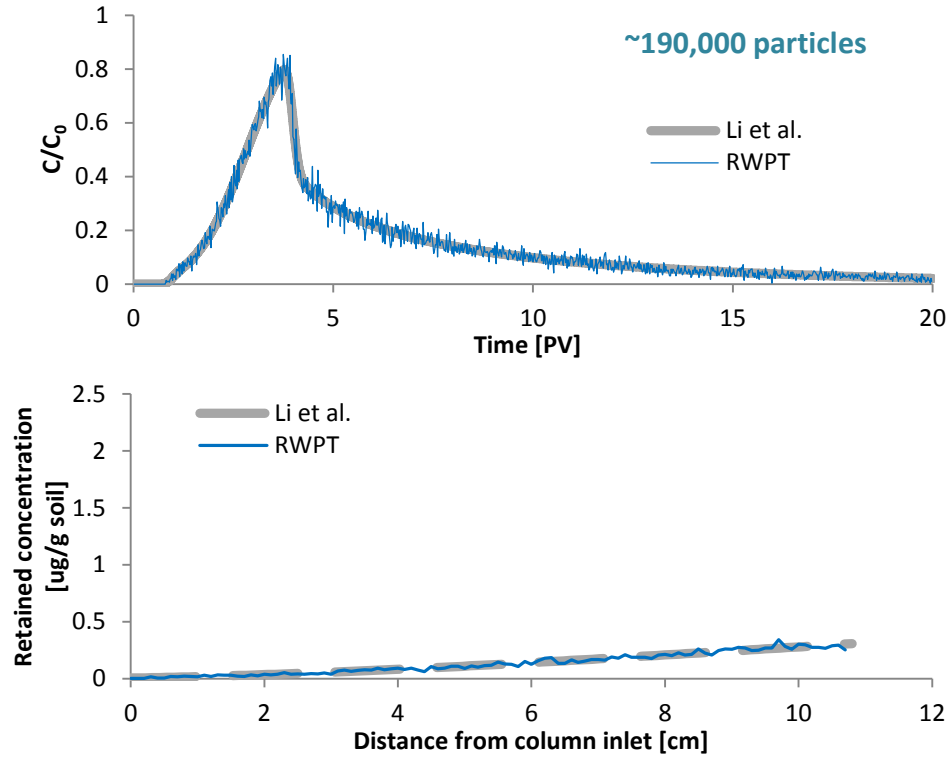


Figure 0-4. Breakthrough (1) and retained (at 20 PV) (2) concentrations of reversibly attaching particles according to MFT.

II.1.2. Verification of the FD (i.e. solute transport) module

Breakthrough predictions of the FD module and those obtained analytically for a 2 pore volume input pulse of (1) a tracer solute and (2) dissolved TCE reducing to dissolved ethene are presented in Figure 0.5. Model mass balance errors, computed on a mole basis for total C_2 (i.e. the sum of the number of moles of PCE and that of ethene) in the system, were of the order of hundredths of a percent for all simulations.

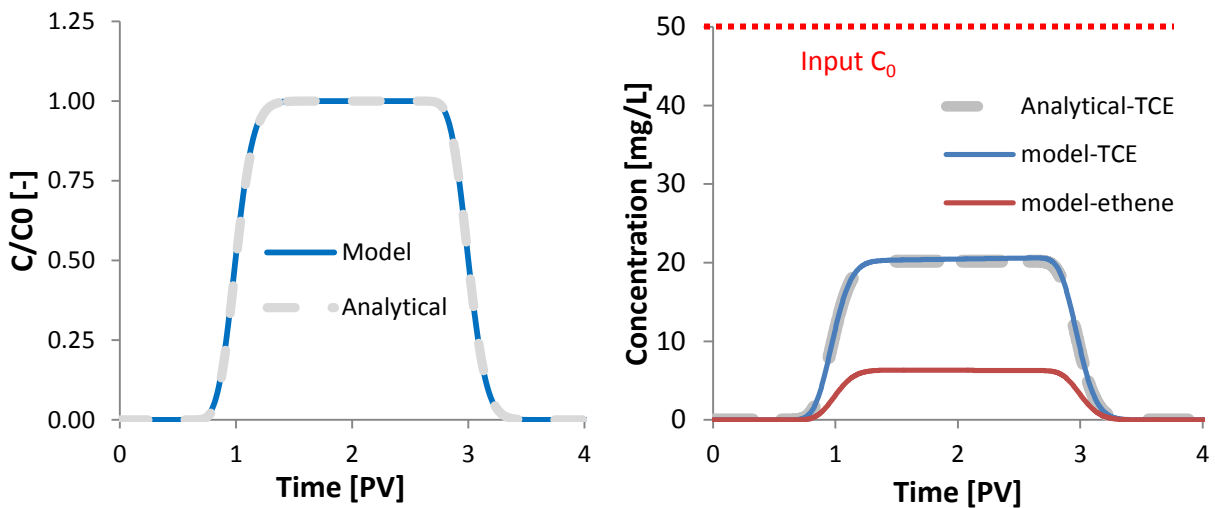


Figure 0-5. Breakthrough concentrations of a 2PV pulse of a tracer solute (1) and of reacting dissolved TCE (2).

Appendix III

III.1. Sensitivity of Modeling Results to Numerical Parameters

Competitive NP/surfactant interactions with the o/w IF: The base values selected for the time-step size, Δt , and grid-block spacing, Δx , were 1 s and 1 mm, respectively. Δt was then varied between 0.5 to 10 s and Δx was decreased/increased by a factor of 2 (i.e. 0.5-2 mm). NP-surfactant interactions with the o/w IF were simulated for three different interfacial attachment efficiency (α_{if})-values of (a) 0.013, (b) 0.13, and (c) 1.0, while a constant surfactant adsorption rate constant (k_{ads}^{if}) of $1 \times 10^{-3} \text{ s}^{-1}$ was used in all simulations. NP-surfactant interactions with the solid phase were not included in the simulations. Other model input parameters are presented in Table 5.1. Simulation results are shown in Figures 0.6 to 0.8.

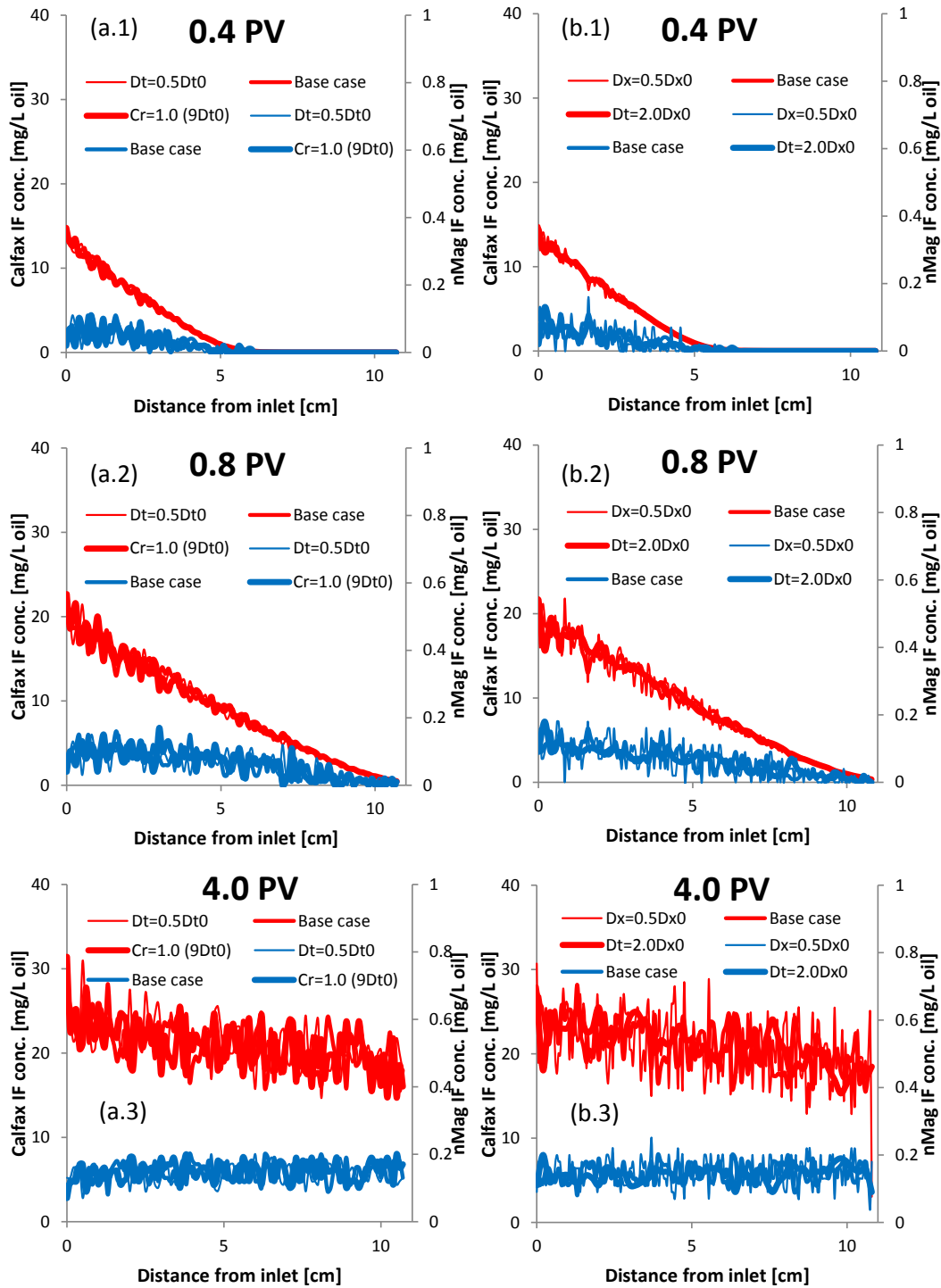


Figure 0-6. Influence of changes in (a) time-step size, Δt , and (b) grid-block spacing, Δx , on simulated NP and surfactant retention profiles after (1) 0.4, (2) 0.8 and (3) 4.0 pore volumes for $\alpha_{if} = 0.013$.

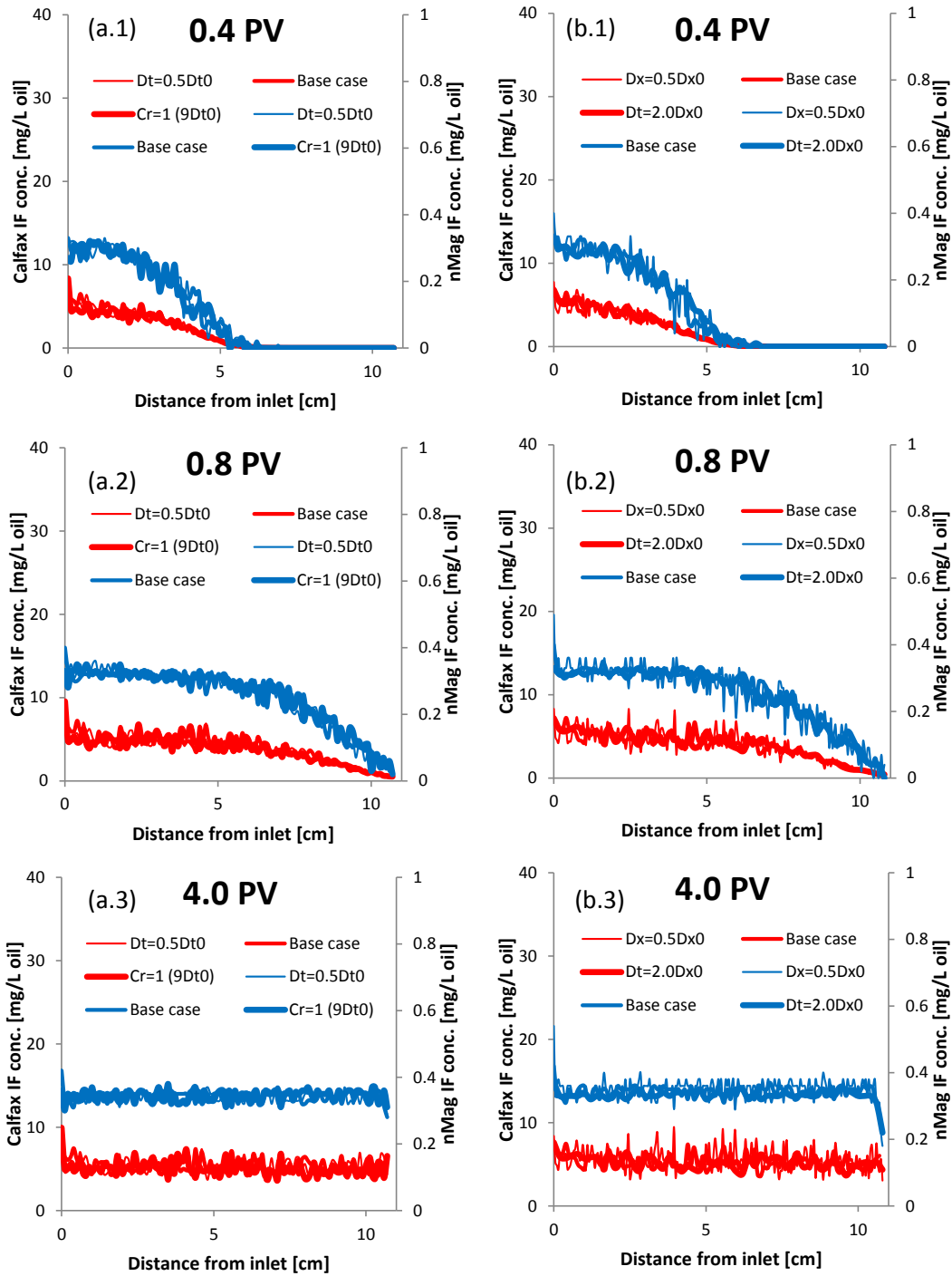


Figure 0-7. Influence of changes in (a) time-step size, Δt , and (b) grid-block spacing, Δx , on simulated NP and surfactant retention profiles after (1) 0.4, (2) 0.8 and (3) 4.0 pore volumes for $\alpha_{if} = 0.13$.

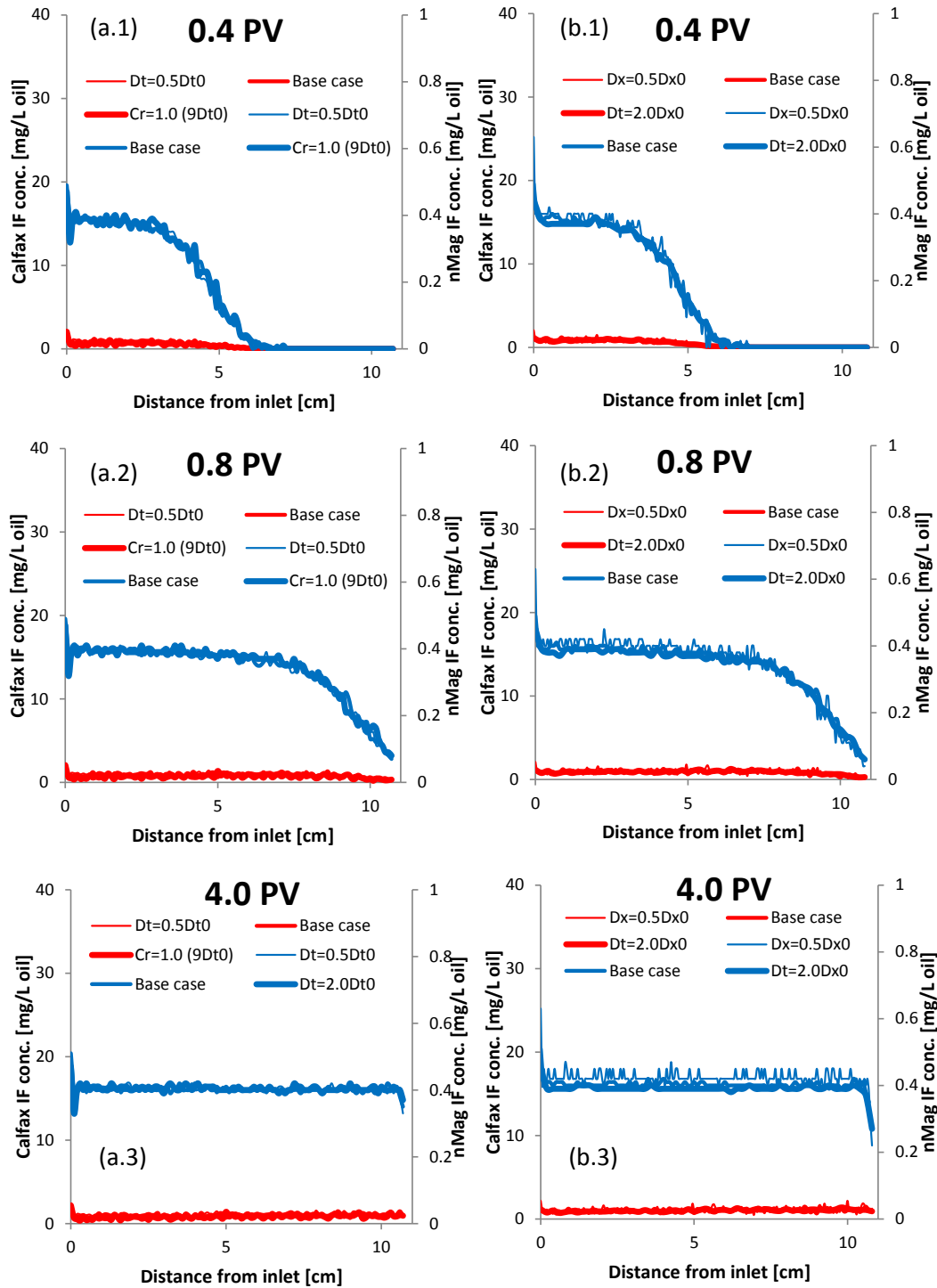


Figure 0-8. Influence of changes in (a) time-step size, Δt , and (b) grid-block spacing, Δx , on simulated NP and surfactant retention profiles after (1) 0.4, (2) 0.8 and (3) 4.0 pore volumes for $\alpha_{if} = 1.0$.

Appendix IV

IV.1. Nomenclature

Symbol	Description	Unit
English Symbols		
A	Hamaker constant	J
A_c	cross-sectional area of the column	m ²
A_s	Happel correction factor	-
a_0	specific surface area of the NAPL blobs per unit volume of porous medium	m ² /m ³
a_{c_1/c_2}	stoichiometric ratio of component c_1 to component c_2	mol/mol
a_h	hydrodynamic radius of aggregates	m
C_w^c	aqueous concentration of component c	mM
C_{PCE}^{sol}	molar aqueous solubility limit of pure phase PCE	mol/m ³
Da_I	type (I) Damköhler number	-
\widehat{Da}_I	modified Damköhler number	-
D_f	fractal dimension	-
D_{wc}^h	aqueous-phase hydrodynamic dispersion coefficient of component c	m ² /s
D_∞	diffusion coefficient of a particle in an infinite medium	m ² /s
d_{50}	median grain size	m
d_b^{init}	representative diameter of spherical oil blobs	m
d_c	representative collector (sand grain) diameter	m
d_M	diameter of a “medium” sand grain	0.5 mm
d_{P_i}	diameter of particle i	m
$d_{P(i=1)}$	diameter of a primary particle	m
d_p^x	NP diameter at weight percentage equal to $x\%$	m
$E_{wn_o}^*$	rate of interphase mass transfer	g m ⁻³ s ⁻¹
f	fraction of o/w IF in contact with mobile aqueous phase	-
f_a	fraction of nAg particles available for dissolution	-
$f_{Fe^0}^{init}$	initial Fe^0 -content of nZVI particles	-
\bar{g}	gravitational acceleration vector	m/s ²
J_{in}^{mP}	model particle flux	1/PV
k	intrinsic permeability of the medium	m ²
\hat{k}	lumped mass-transfer coefficient/ effective reaction rate coefficient	1/s
k_{att}	NP attachment rate coefficients	1/s
k_B	<i>Boltzman</i> constant	J/°K
k_{det}	NP detachment rate coefficients	1/s
k_{diss}	nAg dissolution rate coefficient	1/s

k_{eff}	effective mass transfer coefficient	1/s
k_f	mass transfer rate coefficient	
k_{if}^c	adsorption rate constant of component c to the oil/water interface	1/s
k_r	first-order PCE reduction rate constant	$m^3/s \text{ mol}$
k_{rw}	relative permeability of the aqueous phase	-
k_s^c	adsorption rate constant of component c to the solid phase	1/s
k_{str}	straining coefficient	1/s
L_{obs}	distance between the upstream end of the reactive zone and the location of the observation point	m
l_R	average contact length of the contaminant in the reactive zone	m
$m_{p(i)}$	mass of an i -size cluster	g
N_0	initial particle number concentration	m^{-3}
N_A	attraction number	-
N_G	gravity number	-
N_{Pe}	Peclet number	-
N_R	aspect ratio	-
N_{vdW}	van der Waals number	-
n_i	number concentration of i -size clusters	$1/m^3$
$P_{p(i) \leftarrow p(j)}^{agg}$	aggregation probability for association of a j -size cluster with an i -size cluster	-
$P_p^{att,s}$	probability of the attachment of particle p to solid phase	-
$P_p^{att,if}$	probability of the attachment of particle p to the oil/water interface	-
P_p^{det}	probability of the detachment of particle p from solid phase	-
q_w	Darcy velocity	m/s
R	universal gas constant	$J \text{ mol}^{-1} \text{ K}^{-1}$
r^c	net molar rate of production of component c in the aqueous phase per unit bulk volume	$\text{mol}/m^3 \text{ s}$
Sh'	Sherwood number	-
SSA_n	effective specific surface area of oil phase residuals	$m^2 \text{ of IF}/m^3 \text{ oil}$
SSA_p	specific surface area of particle p	m^2/g
S_n^{init}	initial non-aqueous phase saturation	-
S_α	volumetric saturation of α -phase	-
T	temperature	$^\circ\text{K}$
t	time	s
t_{p_i}	age of particle i	s
U_{i_g}	uniformity index of soil	-
U_w	approach (superficial) velocity of water	m/s
u	corrected flow velocity	m/s
V_{max}	height of the double-layer energy barrier	J
v_w	Pore water velocity	m/s
x	position measured from inlet boundary	m
Z	normally-distributed random variable	-
z	distance from the column inlet	m

Greek Symbols		
α_d	attachment efficiency	-
α_{if}	interfacial attachment efficiency	-
α_L	longitudinal dispersivity	m
α_{PC}	attachment efficiency	-
α_{PP}	attachment efficiency for aggregation	-
β	straining function parameter	-
Γ_c^{eq}	surface excess of component c	mmol/m ²
γ	Interfacial or surface tension	mN/m
Δt	time step	s
Δx	Grid-block spacing	m
δ_g	normalized median sand grain diameter	-
η_0	overall single collector contact efficiency (a.k.a. collisions efficiency)	-
η_D	collision efficiency for transport by diffusion	-
η_G	collision efficiency for transport by gravity	-
η_I	collision efficiency for transport by interception	-
η_{if}	interfacial collision contact efficiency	-
θ_α	volumetric content of α -phase	-
κ	inverse Debye length	1/m
λ	filter coefficient	1/m
λ_d	rate constant of decay	1/s
λ_w	mobility of the aqueous phase	m ³ s/g
μ_w	dynamic viscosity of water	g m ⁻¹ s ⁻¹
ρ_b	bulk density of soil	kg/m ³
ρ_p	particle density	kg/m ³
ρ_α	mass density of α -phase	kg/m ³
φ	soil porosity	-
ϕ	effective porosity of soil	-
ψ_{att}	site blocking function	-
ψ_{str}	particle straining function	-
ω_{if}^c	interfacial concentrations of component c	mmol/L oil
ω_s^c	solid phase concentration of component c	mol/kg dry soil
$\omega_s^{c,max}$	maximum retention capacity of component c by solid phase	mol/kg soil

BIBLIOGRAPHY

1. Lin, D., et al., *Fate and Transport of Engineered Nanomaterials in the Environment*. Journal of Environment Quality, 2010. **39**: p. 1896.
2. Navarro, E., et al., *Toxicity of Silver Nanoparticles to Chlamydomonas reinhardtii*. Environmental Science & Technology, 2008. **42**(23): p. 8959-8964.
3. Wiesner, M.R., et al., *Assessing the Risks of Manufactured Nanomaterials*. Environmental Science & Technology, 2006. **40**(14): p. 4336-4345.
4. Gao, B., et al., *Capillary retention of colloids in unsaturated porous media*. Water Resources Research, 2008. **44**: p. 1-7.
5. Nowack, B. and T.D. Bucheli, *Occurrence, behavior and effects of nanoparticles in the environment*. Environmental pollution (Barking, Essex : 1987), 2007. **150**: p. 5-22.
6. Torkzaban, S., et al., *Hysteresis of colloid retention and release in saturated porous media during transients in solution chemistry*. Environmental science & technology, 2010. **44**: p. 1662-9.
7. Brar, S.K., et al., *Engineered nanoparticles in wastewater and wastewater sludge – Evidence and impacts*. Waste Management, 2010. **30**(3): p. 504-520.
8. Ryan, J.N. and M. Elimelech, *Colloid mobilization and transport in groundwater*. Colloids and Surfaces a-Physicochemical and Engineering Aspects, 1996. **107**: p. 1-56.
9. Klaire, S.J., et al., *Nanomaterials in the environment: Behavior, fate, bioavailability, and effects*. Environmental Toxicology and Chemistry, 2008. **27**(9): p. 1825-1851.
10. Torkzaban, S., et al., *Transport and deposition of functionalized CdTe nanoparticles in saturated porous media*. Journal of contaminant hydrology, 2010. **118**: p. 208-17.
11. Berge, N.D. and C.A. Ramsburg, *Oil-in-water emulsions for encapsulated delivery of reactive iron particles*. Environmental science & technology, 2009. **43**: p. 5060-6.
12. Peralta-Videa, J.R., et al., *Nanomaterials and the environment: a review for the biennium 2008-2010*. Journal of hazardous materials, 2011. **186**: p. 1-15.
13. Saleh, N., et al., *Surface Modifications Enhance Nanoiron Transport and NAPL Targeting in Saturated Porous Media*. Environmental Engineering Science, 2007. **24**: p. 45-57.
14. Jaisi, D.P., et al., *Transport of single-walled carbon nanotubes in porous media: filtration mechanisms and reversibility*. Environmental science & technology, 2008. **42**: p. 8317-23.
15. Li, Y., et al., *Investigation of the transport and deposition of fullerene (C60) nanoparticles in quartz sands under varying flow conditions*. Environmental science & technology, 2008. **42**: p. 7174-80.
16. Pelley, A.J. and N. Tufenkji, *Effect of particle size and natural organic matter on the migration of nano- and microscale latex particles in saturated porous media*. Journal of colloid and interface science, 2008. **321**: p. 74-83.

17. Wang, Y., et al., *Transport and retention of nanoscale C60 aggregates in water-saturated porous media*. Environmental science & technology, 2008. **42**: p. 3588-94.
18. Petosa, A.R., et al., *Aggregation and deposition of engineered nanomaterials in aquatic environments: role of physicochemical interactions*. Environmental science & technology, 2010. **44**: p. 6532-49.
19. Bradford, S.a., *Physical factors affecting the transport and fate of colloids in saturated porous media*. Water Resources Research, 2002. **38**: p. 1-12.
20. Elimelech, M. and C.R. O'Meila, *Kinetics of Deposition of Colloidal Particles in Porous Media*. Environmental Engineering Science, 1990. **24**: p. 1528-1536.
21. Chatterjee, J. and S.K. Gupta, *An agglomeration-based model for colloid filtration*. Environmental science & technology, 2009. **43**: p. 3694-9.
22. Fang, J., et al., *Stability of titania nanoparticles in soil suspensions and transport in saturated homogeneous soil columns*. Environmental pollution (Barking, Essex : 1987), 2009. **157**: p. 1101-9.
23. Cullen, E., et al., *Simulation of the subsurface mobility of carbon nanoparticles at the field scale*. Advances in Water Resources, 2010. **33**: p. 361-371.
24. Tufenkji, N. and M. Elimelech, *Correlation equation for predicting single-collector efficiency in physicochemical filtration in saturated porous media*. Environmental science & technology, 2004. **38**: p. 529-36.
25. Yao, K.-m., H. M.T., and C.R. O'Meila, *Water and waste water filtration: concepts and applications*. . Environmental Engineering Science, 1971. **5**: p. 1105-1112.
26. Kretzschmar, R., et al., *Experimental determination of colloid deposition rates and collision efficiencies in natural porous media*. Water Resources Research, 1997. **33**(5): p. 1129-1137.
27. Johnson, P.R. and M. Elimelech, *Dynamics of Colloid Deposition in Porous Media : Blocking Based on Random Sequential Adsorption*. Langmuir, 1996. **11**: p. 801-812.
28. Bolster, C.H., et al., *Spatial distribution of deposited bacteria following miscible displacement experiments in intact cores*. Water Resources Research, 1999. **35**(6): p. 1797-1807.
29. Guzman, K.A.D., M.P. Finnegan, and J.F. Banfield, *Influence of surface potential on aggregation and transport of titania nanoparticles*. Environmental Science & Technology, 2006. **40**(24): p. 7688-7693.
30. Tufenkji, N., et al., *Transport of Cryptosporidium oocysts in porous media: role of straining and physicochemical filtration*. Environmental science & technology, 2004. **38**: p. 5932-8.
31. Xu, S., B. Gao, and J.E. Saiers, *Straining of colloidal particles in saturated porous media*. 2006. **42**: p. 1-10.
32. Bradford, S.a., et al., *Modeling colloid attachment, straining, and exclusion in saturated porous media*. Environmental science & technology, 2003. **37**: p. 2242-50.
33. Bradford, S.A. and M. Bettahar, *Straining, attachment, and detachment of Cryptosporidium oocysts in saturated porous media*. Journal of Environmental Quality, 2005. **34**(2): p. 469-478.
34. Wiesner, M.R. and J.-Y. Bottero, *Environmental Nanotechnology*. The McGraw-Hill Companies: New York, 2007: p. 540.
35. Elzey, S. and V.H. Grassian, *Agglomeration, isolation and dissolution of commercially manufactured silver nanoparticles in aqueous environments*. Journal of Nanoparticle Research, 2009. **12**: p. 1945-1958.

36. Li, X., J.J. Lenhart, and H.W. Walker, *Dissolution-Accompanied Aggregation Kinetics of Silver Nanoparticles*. Langmuir, 2010. **26**(22): p. 16690-16698.
37. Bian, S.-W., et al., *Aggregation and dissolution of 4 nm ZnO nanoparticles in aqueous environments: influence of pH, ionic strength, size, and adsorption of humic acid*. Langmuir : the ACS journal of surfaces and colloids, 2011. **27**: p. 6059-68.
38. Elimelech, M., et al., *Particle deposition and aggregation - measurement, modelling and simulation*. 1995, Amsterdam: Elsevier.
39. Chen, K.L. and M. Elimelech, *Aggregation and deposition kinetics of fullerene (C60) nanoparticles*. Langmuir : the ACS journal of surfaces and colloids, 2006. **22**: p. 10994-1001.
40. Smoluchowski, M.v., *Versuch einer mathematischen Theorie der Koagulationskinetik kolloider Lösungen*. Z. phys. Chem, 1917. **92**(129-168): p. 9.
41. Lin, M.Y., et al., *Universality in colloid aggregation*. Nature, 1989. **339**(6223): p. 360-362.
42. Cundy, A.B., L. Hopkinson, and R.L. Whitby, *Use of iron-based technologies in contaminated land and groundwater remediation: A review*. Science of the Total Environment, 2008. **400**(1): p. 42-51.
43. Doong, R.-A. and Y.-J. Lai, *Dechlorination of tetrachloroethylene by palladized iron in the presence of humic acid*. Water research, 2005. **39**(11): p. 2309-2318.
44. Dries, J., et al., *Competition for sorption and degradation of chlorinated ethenes in batch zero-valent iron systems*. Environmental Science & Technology, 2004. **38**(10): p. 2879-2884.
45. Liu, Y. and G.V. Lowry, *Effect of particle age (Fe0 content) and solution pH on NZVI reactivity: H2 evolution and TCE dechlorination*. Environmental Science & Technology, 2006. **40**(19): p. 6085-6090.
46. Liu, Y., et al., *Trichloroethene hydrodechlorination in water by highly disordered monometallic nanoiron*. Chemistry of materials, 2005. **17**(21): p. 5315-5322.
47. Liu, J. and R.H. Hurt, *Ion release kinetics and particle persistence in aqueous nano-silver colloids*. Environmental science & technology, 2010. **44**: p. 2169-75.
48. Zhang, W., et al., *Modeling the primary size effects of citrate-coated silver nanoparticles on their ion release kinetics*. Environmental science & technology, 2011. **45**: p. 4422-8.
49. Kralchevsky, P.a. and K. Nagayama, *Capillary interactions between particles bound to interfaces, liquid films and biomembranes*. Advances in colloid and interface science, 2000. **85**: p. 145-92.
50. Bishop, E.J., et al., *Anionic homopolymers efficiently target zerovalent iron particles to hydrophobic contaminants in sand columns*. Environmental science & technology, 2010. **44**: p. 9069-74.
51. Saleh, N., et al., *Adsorbed triblock copolymers deliver reactive iron nanoparticles to the oil/water interface*. Nano letters, 2005. **5**: p. 2489-94.
52. Rogers, B.B. and B.E. Logan, *BACTERIAL TRANSPORT IN NAPL-CONTAMINATED POROUS MEDIA*. 2000: p. 657-666.
53. Link, A., et al., *Effects of growth conditions and NAPL presence on transport of Pseudomonas saccharophilia P15 through porous media*. Water research, 2010. **44**: p. 2793-802.
54. Zheng, C. and G.D. Bennett, *Applied contaminant transport modeling: Theory and practice*. Vol. 1. 1995: Van Nostrand Reinhold New York.
55. Kinzelbach, W., *Groundwater modeling: An introduction with sample programs in Basic*. 1986, Amsterdam: Elsevier.

56. Ahlstrom, S., et al., *Multicomponent mass transport model: Theory and numerical implementation (discrete-parcel-random-walk version)*, 1977, Battelle Pacific Northwest Labs., Richland, Wash.(USA).
57. Prickett, T.A., T.G. Naymik, and C.G. Lonnquist, *A 'Random Walk' Solute Transport Model for Selected Groundwater Quality Evaluations*. Bulletin 65 1981. 103, 1981: p. 68.
58. Salamon, P., D. Fernández-Garcia, and J.J. Gómez-Hernández, *Modeling mass transfer processes using random walk particle tracking*. Water Resources Research, 2006. **42**: p. 1-14.
59. Scheibe, T.D. and B.D. Wood, *A particle-based model of size or anion exclusion with application to microbial transport in porous media*. Water Resources Research, 2003. **39**(4).
60. Schwartz, F.W., L. Smith, and A.S. Crowe, *A stochastic analysis of macroscopic dispersion in fractured media*. Water Resources Research, 1983. **19**(5): p. 1253-1265.
61. Garven, G. and R.A. Freeze, *Theoretical analysis of the role of groundwater flow in the genesis of stratabound ore deposits; 1, Mathematical and numerical model*. American Journal of Science, 1984. **284**(10): p. 1085-1124.
62. Itô, K., *On stochastic differential equations*. Mem. Amer. Math. Soc, 1951. **4**: p. 1-51.
63. Salamon, P., D. Fernández-Garcia, and J.J. Gómez-Hernández, *A review and numerical assessment of the random walk particle tracking method*. Journal of contaminant hydrology, 2006. **87**: p. 277-305.
64. Keane, E., *Fate, Transport and Toxicity of Nanoscale Zero-Valent Iron (nZVI) Used During Superfund Remediation*, 2010, Duke University.
65. Kim, H., et al., *Degradation of trichloroethylene by zero-valent iron immobilized in cationic exchange membrane*. Desalination, 2008. **223**(1): p. 212-220.
66. Pooley, K.E., et al., *Aerobic biodegradation of chlorinated ethenes in a fractured bedrock aquifer: quantitative assessment by compound-specific isotope analysis (CSIA) and reactive transport modeling*. Environmental Science & Technology, 2009. **43**(19): p. 7458-7464.
67. Arnold, W.A. and A.L. Roberts, *Pathways and kinetics of chlorinated ethylene and chlorinated acetylene reaction with Fe (0) particles*. Environmental Science & Technology, 2000. **34**(9): p. 1794-1805.
68. Freedman, D.L. and J.M. Gossett, *Biological reductive dechlorination of tetrachloroethylene and trichloroethylene to ethylene under methanogenic conditions*. applied and Environmental Microbiology, 1989. **55**(9): p. 2144-2151.
69. Quinn, J., et al., *Field demonstration of DNAPL dehalogenation using emulsified zero-valent iron*. Environmental Science & Technology, 2005. **39**(5): p. 1309-1318.
70. Schrick, B., et al., *Hydrodechlorination of Trichloroethylene to Hydrocarbons Using Bimetallic Nickel-Iron Nanoparticles*. 2002: p. 5140-5147.
71. Hydutsky, B.W., et al., *Optimization of nano- and microiron transport through sand columns using polyelectrolyte mixtures*. Environmental science & technology, 2007. **41**: p. 6418-24.
72. Phenrat, T., et al., *Particle Size Distribution, Concentration, and Magnetic Attraction Affect Transport of Polymer-Modified Fe⁰ Nanoparticles in Sand Columns*. Environmental Science & Technology, 2009. **43**(13): p. 5079-5085.
73. Zhan, J., et al., *Multifunctional colloidal particles for in situ remediation of chlorinated hydrocarbons*. Environmental science & technology, 2009. **43**: p. 8616-21.

74. Elliott, D.W. and W.-X. Zhang, *Field assessment of nanoscale bimetallic particles for groundwater treatment*. Environmental Science & Technology, 2001. **35**(24): p. 4922-4926.
75. Henn, K.W. and D.W. Waddill, *Utilization of nanoscale zero-valent iron for source remediation—A case study*. Remediation Journal, 2006. **16**: p. 57-77.
76. Bayer, P. and M. Finkel, *Life cycle assessment of active and passive groundwater remediation technologies*. Journal of contaminant hydrology, 2006. **83**: p. 171-99.
77. Moon, J.-W., et al., *Remediation of TCE-contaminated groundwater using zero valent iron and direct current: experimental results and electron competition model*. Environmental Geology, 2005. **48**(6): p. 805-817.
78. Schrick, B., et al., *Hydrodechlorination of trichloroethylene to hydrocarbons using bimetallic nickel-iron nanoparticles*. Chemistry of materials, 2002. **14**(12): p. 5140-5147.
79. Shin, M.-C., et al., *Effect of surfactant on reductive dechlorination of trichloroethylene by zero-valent iron*. Desalination, 2008. **223**(1): p. 299-307.
80. Wang, W., et al., *Reactivity characteristics of poly (methyl methacrylate) coated nanoscale iron particles for trichloroethylene remediation*. Journal of hazardous materials, 2010. **173**(1): p. 724-730.
81. Laine, D.F. and I.F. Cheng, *The destruction of organic pollutants under mild reaction conditions: A review*. Microchemical journal, 2007. **85**(2): p. 183-193.
82. Li, Z., et al., *Enhanced Reduction of Chromate and PCE by Pelletized Surfactant-Modified Zeolite/Zeravalent Iron*. Environmental Science & Technology, 1999. **33**: p. 4326-4330.
83. Viollier, E., et al., *The ferrozine method revisited: Fe (II)/Fe (III) determination in natural waters*. Applied Geochemistry, 2000. **15**(6): p. 785-790.
84. Powers, S.E., et al., *Hydrology Phenomenological models for transient NAPL-water mass-transfer processes*. Journal of contaminant hydrology, 1994. **16**: p. 1-33.
85. Wilkins, M.D., L.M. Abriola, and K.D. Pennell, *An experimental investigation of rate-limited nonaqueous phase liquid volatilization in unsaturated porous media: Steady state mass transfer*. Water Resources Research, 1995. **31**(9): p. 2159-2172.
86. Brusseau, M.L., et al., *Dissolution of nonuniformly distributed immiscible liquid: Intermediate-scale experiments and mathematical modeling*. Environmental Science & Technology, 2002. **36**(5): p. 1033-1041.
87. Fure, A.D., J.W. Jawitz, and M.D. Annable, *DNAPL source depletion: Linking architecture and flux response*. Journal of contaminant hydrology, 2006. **85**(3): p. 118-140.
88. Bradford, S.A., R.A. Vendlinski, and L.M. Abriola, *The entrapment and long-term dissolution of tetrachloroethylene in fractional wettability porous media*. Water Resources Research, 1999. **35**(10): p. 2955-2964.
89. Christ, J.A., et al., *Predicting DNAPL mass discharge from pool-dominated source zones*. Journal of contaminant hydrology, 2010. **114**(1): p. 18-34.
90. Abriola, L.M., J.R. Lang, and K. Rathfelder, *Michigan soil vapor extraction remediation (MISER) model: a computer program to model soil vapor extraction and bioventing of organic chemicals in unsaturated geological material* 1997: US Environmental Protection Agency, Research and Development, National Risk Management Research Laboratory.

91. Taghavy, A., et al., *Effectiveness of nanoscale zero-valent iron for treatment of a PCE–DNAPL source zone*. Journal of contaminant hydrology, 2010. **118**(3–4): p. 128-142.
92. Doong, R.-a. and Y.-l. Lai, *Effect of metal ions and humic acid on the dechlorination of tetrachloroethylene by zerovalent iron*. Chemosphere, 2006. **64**(3): p. 371-378.
93. Cho, J. and M.D. Annable, *Characterization of pore scale NAPL morphology in homogeneous sands as a function of grain size and NAPL dissolution*. Chemosphere, 2005. **61**(7): p. 899-908.
94. Kaye, G.W.C. and T.H. Laby, *Tables of physical and chemical constants: and some mathematical functions* 1921: Longmans, Green and co.
95. Qin, X., et al., *Simulation-based process optimization for surfactant-enhanced aquifer remediation at heterogeneous DNAPL-contaminated sites*. Science of the Total Environment, 2007. **381**(1): p. 17-37.
96. Chiao, F., R. Currie, and T. McKone, *Intermedia transfer factors for contaminants found at hazardous waste sites: Tetrachloroethylene (PCE)*, 1994, California Department of Toxic Substances Control, available at: <http://www.dtsc.ca.gov/AssessingRisk/Upload/pce.pdf>.
97. Pennell, K.D., et al., *Surfactant enhanced remediation of soil columns contaminated by residual tetrachloroethylene*. Journal of contaminant hydrology, 1994. **16**(1): p. 35-53.
98. Zhang, W.-x., *Nanoscale iron particles for environmental remediation : An overview*. 2003: p. 323-332.
99. Kunkel, R. and F. Wendland, *WEKU – a GIS-Supported stochastic model of groundwater residence times in upper aquifers for the supraregional groundwater management*. Environmental Geology, 1997. **30**(1-2): p. 1-9.
100. Amos, R.T. and K. Ulrich Mayer, *Investigating the role of gas bubble formation and entrapment in contaminated aquifers: Reactive transport modelling*. Journal of contaminant hydrology, 2006. **87**(1): p. 123-154.
101. Fogler, H.S., *Elements of chemical reaction engineering*. Vol. 817. 1999: Prentice-Hall International London.
102. Klump, S., et al., *Experimental and numerical studies on excess-air formation in quasi-saturated porous media*. Water Resources Research, 2008. **44**(5): p. W05402.
103. George, S., et al., *Use of a high-throughput screening approach coupled with in vivo zebrafish embryo screening to develop hazard ranking for engineered nanomaterials*. ACS nano, 2011. **5**: p. 1805-17.
104. Kent, R.D. and P.J. Vikesland, *Controlled Evaluation of Silver Nanoparticle Dissolution Using Atomic Force Microscopy*. Environmental Science & Technology, 2011. **46**(13): p. 6977-6984.
105. Sotiriou, G.A. and S.E. Pratsinis, *Antibacterial Activity of Nanosilver Ions and Particles*. Environmental Science & Technology, 2010. **44**(14): p. 5649-5654.
106. Sotiriou, G.A., et al., *Quantifying the Origin of Released Ag⁺ Ions from Nanosilver*. Langmuir, 2012. **28**(45): p. 15929-15936.
107. Sagee, O., I. Dror, and B. Berkowitz, *Transport of silver nanoparticles (AgNPs) in soil*. Chemosphere, 2012. **88**: p. 670-675.
108. Tian, Y., et al., *Transport of engineered nanoparticles in saturated porous media*. Journal of Nanoparticle Research, 2010. **12**: p. 2371-2380.
109. Hubaux, A. and G. Vos, *Decision and detection limits for calibration curves*. Analytical Chemistry, 1970. **42**(8): p. 849-855.

110. Bergstrom, L., *Hamaker constants of inorganic materials*. Advances in colloid and interface science, 1997. **70**: p. 125-169.
111. Israelechvili, J., *Intermolecular and surface forces*. 2 ed1992, London: Academic Press.
112. Scheckel, K.G., et al., *Synchrotron speciation of silver and zinc oxide nanoparticles aged in a kaolin suspension*. Environmental science & technology, 2010. **44**: p. 1307-12.
113. Coutris, C., E.J. Joner, and D.H. Oughton, *Aging and soil organic matter content affect the fate of silver nanoparticles in soil*. The Science of the total environment, 2012. **420**: p. 327-33.
114. Taghavy, A., et al., *Mathematical modeling of the transport and dissolution of silver nanoparticles in porous media*. Environmental Science & Technology, 2013: p. Submitted.
115. Mittelman, A., et al., *Influence of Dissolved Oxygen on Silver Nanoparticle Mobility and Dissolution in Water-Saturated Quartz Sand*. Submitted to J. Nanoparticle Res., 2013.
116. Kittler, S., et al., *Toxicity of silver nanoparticles increases during storage because of slow dissolution under release of silver ions*. Chemistry of materials, 2010. **22**(16): p. 4548-4554.
117. Sarathy, V., et al., *Aging of iron nanoparticles in aqueous solution: effects on structure and reactivity*. The Journal of Physical Chemistry C, 2008. **112**(7): p. 2286-2293.
118. Sohn, K., et al., *Fe (0) nanoparticles for nitrate reduction: stability, reactivity, and transformation*. Environmental Science & Technology, 2006. **40**(17): p. 5514-5519.
119. Damm, C. and H. Münstedt, *Kinetic aspects of the silver ion release from antimicrobial polyamide/silver nanocomposites*. Applied Physics A, 2008. **91**: p. 479-486.
120. Benn, T.M. and P. Westerhoff, *Nanoparticle silver released into water from commercially available sock fabrics*. Environmental science & technology, 2008. **42**: p. 4133-9.
121. Geranio, L., M. Heuberger, and B. Nowack, *The behavior of silver nanotextiles during washing*. Environmental science & technology, 2009. **43**: p. 8113-8.
122. Solovitch, N., et al., *Concurrent Aggregation and Deposition of TiO₂ Nanoparticles in a Sandy Porous Media*. Environmental Science & Technology, 2010. **44**(13): p. 4897-4902.
123. Raychoudhury, T., N. Tufenkji, and S. Ghoshal, *Aggregation and deposition kinetics of carboxymethyl cellulose-modified zero-valent iron nanoparticles in porous media*. Water research, 2012. **46**: p. 1735-44.
124. Phenrat, T., et al., *Particle size distribution, concentration, and magnetic attraction affect transport of polymer-modified Fe(0) nanoparticles in sand columns*. Environmental science & technology, 2009. **43**: p. 5079-85.
125. M., S., *Versuch einer mathematischen Theorie der Koagulationskinetic kolloider Losungen*. Z. Phys. Chem., 1917. **92**: p. 129-168.
126. Becker, M.D., et al., *A Multi-Constituent Site Blocking Model for Nanoparticle and Stabilizing Agent Transport in Porous Media*. . In preparation, 2013.
127. Liang, Y., et al., *Sensitivity of the transport and retention of stabilized silver nanoparticles to physicochemical factors*. Water research, 2013. **47**(7): p. 2572-2582.
128. Rao, P.S.C., M.D. Annable, and H. Kim, *NAPL source zone characterization and remediation technology performance assessment: recent developments and*

- applications of tracer techniques*. Journal of contaminant hydrology, 2000. **45**(1): p. 63-78.
129. Pennell, K.D., L.M. Abriola, and W.J. Weber, *Surfactant-Enhanced Solubilization of Residual Dodecane in Soil Columns . 1 . Experimental Investigation*. Environmental science & technology, 1993. **27**: p. 2332-2340.
 130. Rosen, M.J., *Surfactants and interfacial phenomena*. 2 ed. 1988: John Wiley and Sons, New York. 431.
 131. Hiemenz, P.C. and R. Rajagopalan, *Principles of Colloid and Surface Chemistry, revised and expanded*. 3 ed. Vol. 14. 1997: CRC.
 132. Abriola, L.M., T.J. Dekker, and K.D. Pennell, *Surfactant-enhanced solubilization of residual dodecane in soil columns. 2. Mathematical modeling*. Environmental Science & Technology, 1993. **27**(12): p. 2341-2351.
 133. Saripalli, K.P., P. Rao, and M. Annable, *Determination of specific NAPL-water interfacial areas of residual NAPLs in porous media using the interfacial tracers technique*. Journal of contaminant hydrology, 1998. **30**(3-4): p. 375-391.
 134. Kim, D., et al., *Surface-modified magnetite nanoparticles for hyperthermia: Preparation, characterization, and cytotoxicity studies*. Current Applied Physics, 2006. **6**: p. e242-e246.
 135. Bedwell, B. and E. Gulari, *Electrolyte-moderated interactions in water/oil microemulsions*. Journal of colloid and interface science, 1984. **102**(1): p. 88-100.
 136. Fagerlund, F., et al., *PCE dissolution and simultaneous dechlorination by nanoscale zero-valent iron particles in a DNAPL source zone*. Journal of contaminant hydrology, 2012. **131**(1-4): p. 9-28.